Characterizing Mosquito Flight Using Measurement and Simulation

A Dissertation

Presented to the Faculty of the Graduate School

of Cornell University

in Partial Fulfillment of the Requirements for the Degree of

Doctor of Philosophy

by

Sarah Miriam Iams

January 2014

Characterizing Mosquito Flight Using Measurement and Simulation

Sarah Miriam Iams, Ph.D.

Cornell University 2014

The mosquito *Aedes aegypti* is a dengue fever vector. Via its flight, it spreads potentially fatal disease to millions of people each year. In this dissertation I describe my work recording *Aedes* males using high speed imaging, quantifying and analyzing their motion, and simulating their flight. I describe image processing techniques that have allowed us to characterize their body position and orientation as well as their wing motion. We find that mosquitoes fly with a sideways component to their flight more often than other recorded Dipterans, and rely on sideslipping turns to change their flight direction. We show quantitatively that they use their stroke plane roll angle to generate sideways accelerations. We also show that, unlike many Dipterans, they do not use their pitch angle to control forward acceleration. Their body roll angle is thus central to the control of their motion. Using computer simulation to probe the stability characteristics of their flight we find that, like other Dipterans, the motion of these mosquitoes lies near the boundary between asymptotic stability and instability. However, the linearized map describing the motion of the body from one wingbeat to the next is not self-adjoint, resulting in potentially large growth of perturbations on the shorter timescales relevant to mosquito motion. These perturbations are rotated as they grow, potentially leading to a reduction in the dimension of the controller.

Biographical Sketch

Sarah hails from the Maryland suburbs of Washington, DC, where her father, Howard, is an analyst for the Social Security Administration and her mother, Ella, runs a small business. Raised in Maryland, Sarah grew up detesting seafood but loving the Potomac River and the Chesapeake Bay. She spent her youth playing soccer, riding her bike, reading books, and doing math problems. A two week trip down the Nanticoke River and Chesapeake Bay with the Chesapeake Bay Foundation during middle school cemented her deep concern for the natural world.

She attended the Math, Science, and Computer Science Magnet program at Montgomery Blair High School, where she was on the computer, debate, mock trial, Envirothon, track, cross country, and math teams. Her senior year she was captain of Montgomery County A, the countywide math team, and her Envirothon team was the state runner-up. Throughout high school she also played soccer, did Tae Kwon Do, and enjoyed meandering through local stream valley parks.

For college, Sarah retreated to the gentle hills of the Purple Valley in Williamstown, Massachusetts, where she majored in Physics at Williams College and was a Goldwater Scholar. At Williams she ran cross country and took up backpacking. She was also a writing tutor, spent her first two years continuing her interest in debate, and was involved in student government and community building efforts. She spent the long winters as a pole vaulter for the track and field team, earning All New England honors her junior year, and spent a summer walking El Camino de Santiago in northern Spain as a Lawrence Travel Fellow. Her

senior year, Sarah traveled to the Grand Canyon with the Williams Outing Club and learned that there are parts of the United States that rival Maryland for their natural beauty.

After Williams, Sarah was a camp counselor in Maine, leading hikes in the White Mountains of New Hampshire. She then went to Cambridge University in the United Kingdom, spending two years as a Herchel Smith Fellow. Her first year was spent hillwalking in Wales and the Lake District and studying fluid dynamics, perturbation methods, numerical analysis, and bifurcation theory in the Department of Applied Math and Theoretical Physics in the course of study known at the time as "Part III Maths". Despite having had no previous exposure to the topics, she was able to to receive her Certificate of Advanced Study in Mathematics with Distinction, the highest honor, thanks to supportive instructors and the quiet of the Emmanuel College library. In 2011, she was informed that her certificate had been retroactively transformed into a Masters degree, so she unexpectedly earned an M.Math. In her second year at Cambridge, Sarah was at the BP Institude where she studied the Kelvin-Helmholtz instability under the direction of Colm Caulfield, earning an M.Phil. in fluid flow in industry and the environment. She enjoyed being exposed to an industrial perspective, and having to take a business course during that time.

After a formative summer at Sandia National Laboratories in Livermore, California, working with Habib Najm on the reduction of systems of equations describing combustion, Sarah decided to continue in applied mathematics. She joined the Center for Applied Mathematics at Cornell University, where she participated in an NSF-IGERT program. Attending a climate change workshop at MSRI in 2008 inspired her to do a project in the economics of groundwater resources with Mukul Majumder, and her strong interest in data led to her studies of mosquito motion under the supervision of John Guckenheimer.

While at Cornell, Sarah lived in Gamma Alpha, a cooperative house of science graduate students, where she paid somebody else to do her grocery shopping, and was involved in EARS as a counselor and trainer. Her time as an EARS trainer transformed how she thought about teaching and learning, and she was excited to return to Maine during the 2012-2013

academic year as a visiting instructor at Bowdoin College, in Brunswick, Maine. There, she gained practical experience as a teacher of mathematics. Sarah will continue to develop her teaching skills, while expanding her research horizons, as the Golovin Assistant Professor of Applied Mathematics at Northwestern University for the 2013-2014 academic year.

Acknowledgements

I would like to acknowledge John Guckenheimer, Itai Cohen, Laura Harrington, Ron Hoy, Tsevi Beatus, Lauren Cator, and Ben Arnold for their insightful assistance with this work. In addition, Itai Cohen provided camera time for motion capture of mosquitoes, and the Harrington lab provided the *Aedes aegypti* mosquitoes used in the work. The Cornell Institute for Computational Sustainability is acknowledged for providing funding, as is the NSF-IGERT program.

The communities of students in the Center for Applied Mathematics, in the Gamma Alpha Graduate Scientific Society, and in EARS are gratefully acknowledged for making my time at Cornell truly lovely. I would also like to acknowledge Mary Lou Zeeman, Matt Boone, Briana Halpin, Jon Reichel, and Jenny Roizen for their invaluable support.

Contents

List of Figures

Chapter 1

Introduction

In much of the world, mosquitoes act as a human disease vector ([35]), and their presence threatens human health. Even in locations where mosquito borne disease is not endemic, mosquitoes are a human irritant and are often a target of control efforts ([45]). Many mosquito studies have focused on the interaction between mosquitoes and humans, because it is this interaction which makes mosquitoes both a nuisance and a danger. Research has focused on many aspects of mosquitoes, including identifying compounds associated with human skin or breath that mosquitoes find attractive ([69]), and characterizing where and how mosquitoes bite humans ([15], [46]). Many studies have focused on mosquito dispersal and control, as well as on the preferred environmental conditions for flight (light of moon, Gambia CO2 distance,).

Mosquitoes were the subjects of substantial early work in understanding insect flight by Kennedy ([43]). However, our understanding of wing motion, maneuverability, and control in Dipterans is based on studies of fruitflies ([76], [5],[58], [38], [29], [14]), hoverflies ([12],[32]), houseflies ([77]), droneflies ([49], [79], [78], [24]), and blowflies ([2], [54]). For mosquitoes, there has been recent work describing flight paths in CO_2 plumes ([3]) and studying interactions with raindrops ([16]). Very little research has focused on the details of mosquito flight ([11]). Mosquito geometry is different from that of the Brachyceran flies listed above, with

mosquitoes having a long narrow body and thin wings, so they have the potential to employ different mechanisms of control in their flight. Since mosquito flight is central to their role as disease vectors, it is an important area for further study. Female mosquitoes find human hosts while in flight ([15]), and in *Aedes aegypti*, the insect studied here, mating often occurs when a female enters a swarm of males ([22]). Understanding male flight characteristics, including the orientation of the male sensory system during flight, as well as eventual studies of the search process in male mosquitoes, has the potential to illuminate this process and could lead to novel techniques for mating interruption.

We observe and measure the motion of male *Aedes aegypti* mosquitoes, which is the Dengue fever vector, in free flight under laboratory conditions. We measure their position and orientation and during flight as well as their wing motion. We present data on mosquito orientation and turning during flight. We assess the applicability to mosquitoes of models of thrust generation that are based on tilting the lift vector, we describe their wing kinematics, and we use numerical simulation to study their flight stability. To observe mosquito motion, we use high speed motion capture, recording three simultaneous views of the insect. The motion capture setup is described by Ristroph et al in ([59]). We trigger recording by hand when an insect enters the frame of the cameras, and we capture hundreds of flights of male *Aedes aegypti* mosquitoes. During these flights, the insects were confined within a cubic flight chamber with 15 cm sides. The insects are induced to fly by various stimuli, including the flight of female mosquitoes, looming stimuli, a 400 Hertz tone, and slight vibrations of their chamber. For the flights examined here, the insects were passing through the center of the chamber and were flying alone, unconnected to another insect.

Mosquitoes have a substantially different body geometry than Brachyceran flies. They have long legs that sometimes occlude the wings in the recorded images, a slender body with an abdomen that is positioned at an angle of approximately 30 degrees below the thorax, and a remarkably short wingstroke, subtending an angle of as little as 34 degrees during a single stroke. This is in contrast to angles of 140 degrees that are typical of fruitflies

([38]). These differences mean that the presence of legs needs to be treated carefully by any image processing algorithm, that the thorax and abdomen need to be treated separately for the purpose of measuring body orientation, and that it is important to measure the location of the leading edge of the wing, as opposed to the mean location of the wing, when characterizing wingstroke. Because of the geometric distinctions between mosquitoes and the more commonly studied Brachycerans, we custom design image processing tools for measuring the position and orientation of the mosquito body and wings.

The image processing tools we employ take advantage of the temporal nature of the data stream, using changes in pixel intensity between successive frames to separate pixels that are in the wings from those in the legs or body. The body position and orientation are measured using average pixel locations and principal components computed from pixel locations. Body yaw is measured using pixels from the thorax and head of the insect as seen from the overhead view. The thorax is not an elongated feature in the side views of the insect, so the abdomen, which is long and slender, is used to identify the pitch angle of the body. The insect's roll angle is also measured directly from body information. When the insect rolls, the abdomen appears tilted relative to the thorax in the overhead view, and this tilt angle serves as a proxy for body roll. In addition, the body orientation angles are also measured using the wings to define a reference frame, so that we are able to examine differences between a reference frame fixed to the body and one fixed to the wings.

The orientation of the leading edge of each wing is measured in every frame using pixels identified in both the side and overhead views, with frame to frame differencing helping us to identify pixels that are potentially part of the leading edge. These leading edge pixels are used to compute the orientation of the wing's span vector, which is a vector aligned with the wing vein. The width of the wing, which is measured in the overhead view, is used to find the chord vector of the wing. This vector is perpendicular to the span and lies within the wing. We use the locations of the tips of the span vectors of each wing, over the course of two wingbeats, to define a reference frame associated with the wings. We compute the

stroke angle, deviation angle, and pitch angle of the wings relative to this frame.

In our observations of male *Aedes aegypti* mosquitoes, we find that their flight direction and body yaw angle are less correlated than in Brachyceran flies, so that their flight often has a strong sideways component. These results are discussed in Chapter 2. In the blowfly, a larger Brachyceran, sideways and backwards flight is observed, but is infrequent ([64]). In fruitflies, it is thought that body yaw angle and flight direction align ([70], [52], [75]), although fruitflies are also known to be capable of generating sideways thrust ([59], [68]). In the hoverfly *Syritta pipiens*, which is well known to exhibit non-forward flight, about 45 percent of flight segments measured by Collett and Land fell within 20 degrees of forward ([12]). In mosquitoes, we find that the insects have such a forward orientation in only 32 percent of frames. Mosquito flight exhibits a stronger sideways component than that measured in other Dipterans. Amongst other insects, sideways flight is known in bees ([6]), and in moths, where it occurs during flight in pheromone plumes ([87]). The presence of sideways flight in mosquitoes means that measurements of mosquito flight paths, such as those by Beeuwkes et al ([3]) where the insects fly in an odor plume, or those by Butail et al of male mosquitoes in a swarm ([8]), would be enhanced by measurements of body yaw angle, since yaw measurements give an indication of the orientation of the insect's sensory apparatus during flight.

Mosquitoes usually fly with a nonzero slip angle, the angle between their body yaw direction and their flight direction. In addition, the slip angle often changes during flight. We observed hundreds of changes in flight direction during the mosquito flights we measured. We found that in over half of such changes in direction, the change was actuated using a sideslip based turn, and there was not a rapid change in the body yaw angle of the insect. The slip angle would change during such turns. The slip angle would also change even when yaw and flight direction were changing simultaneously, because changes in yaw angle were usually smaller in magnitude than those in flight direction. The yaw angle also sometimes changed without an accompanying change in flight direction, again leading to a change in

the slip angle. Sideslip based turns, which are observed in hoverflies ([32], [12]) and blowflies ([64]), are thus central to the mosquito's flight repetoire. Yaw turns are much less common.

Sideslip based turns require the generation of substantial sideways acceleration. Mosquitoes also exhibit a sideways component to their acceleration during straight flight segments. Thrust generation in mosquitoes is examined in chapter 3. Sideways motion in moths has been attributed to changes in body roll angle that redirect the lift force of the wings ([87]). Such a mechanism shows qualitative agreement with measurements of flight speed in houseflies ([77]). We are able to assess this relationship quantitatively in mosquito data, and find that when roll angle is measured in the wing-based reference frame, there is quantitative agreement between sideways thrust generated by the rolled lift vector and measured sideways acceleration. For the linear model $a_y = k_1(g + a_z)\tan\psi + k_2 v_y$ where a_y is measured sideways acceleration, g is vertical acceleration due to gravity, a_z is measured vertical acceleration, v_y is measured sideways velocity, ψ is the measured roll angle, and $k_2 v_y$ is a drag term, the R^2 value is greater than 0.5 for 95 percent of movies and is greater than 0.75 for 49 percent of movies. This strong quantitative agreement indicates that, for mosquitoes, roll is the dominant driver of sideways motion.

For a similar model, using forward acceleration and velocity in place of sideways, and pitch in place of roll, we find only weak agreement with flight data in mosquitoes. The R^2 value exceeds 0.5 in only 23 percent of movies. This is in marked contrast to fruitflies, where such a model has very strong agreement with flight data ([50]). Thus, in mosquitoes, we need not look beyond roll to understand sideways thrust. At the same time, pitch is only a small contributor to net forward thrust. For the mosquito, body pitch is not clearly linked to flight dynamics, and neither is body yaw. Instead, it is the body roll angle that appears to be of particular importance to motion actuation.

Roll torque is likely generated by wing based mechanisms, and these probably also play a large role in forward thrust generation, since it is not well accounted for by changes in body pitch angle. Identifying mechanisms of torque generation and of forward thrust generation

requires understanding the aerodynamic forces produced by the wings. In chapter 4 we examine a number of mosquito wing motions. Mosquitoes have a stroke amplitude of 34 to 54 degrees. This compares to stroke amplitudes of more than 120 degrees in fruitflies and amplitudes of 66 to over 90 degrees in hoverflies ([24]). Combined with wingbeat frequencies in free flight that average 800 Hertz (fruitflies flap at approximately 200 Hertz), these *Aedes aegypti* males have substantially different wing motions than other studied insects. Their short wingstroke leads to lower Reynolds numbers, than other flapping insects. We compute a mean Reynolds number of 75, where the relevant velocity is the maximum velocity at midstroke, and the relevant lengthscale is the wing chord, which is less than half a millimeter. Their low stroke amplitude also means that much of the wing stroke is spent in wing rotation, with a short translation phase sometimes present, and sometimes entirely absent. This, combined with frequent sideways components to their motion, puts their force generation at the limits of where wing forces have been measured and quasisteady aerodynamic models have been assessed. Altshuler et al show that force generation is very sensitive to the speed of rotation, but their work on forces during short wingstrokes uses a wingstroke of 90 degrees, with a long translational period ([1]). Wang et al examine lower Reynolds number wing motions with stroke amplitudes only somewhat beyond the mosquito range, but also include a long translational period in the wing motion ([80]). Experiments that reach the flight regime of mosquitoes and include the impact of sideways translation on flight forces would make it possible to assess the relative importance of different asymmetries to force torque generation in mosquitoes.

We identify asymmetries between the two wings because these are important to creating torque ([38], [5]). In addition, asymmetries between the forward and backward portions of the stroke are observed in other insects and drive forward thrust ([58]). In mosquitoes, as in hoverflies ([78]), stroke amplitude asymmetries between the two wings are not large. This is in contrast to fruitflies ([38]) and blowflies ([2]). Pitch asymmetries are linked to turning maneuvers in fruitflies ([5]) and are also present in mosquitoes. In mosquitoes, an offset

between the time of the wing flip and that of the change in stroke direction is also frequently present. The offset can occur asymmetrically in the two wings, and usually results in a shorter time between wing flips on the upstroke and a longer time on the downstroke. Advanced and delayed wing flips are associated with additional production of lift and of drag ([63], [20], [80]), and we find they have a positive association with forward thrust. In mosquitoes, an advanced wing flip usually occurs when the wings are near the head, and a delayed flip when the wings are away from the head. Along with delayed and advanced wing flips, the insects display different amounts of rotation at the end of the wing flip, with the wing sometimes plunging to near horizontal during the flip. More often, the wing falls to an angle of attack below 45 degrees during the flip and then recovers to near that value. A different depth of flip frequently occurs at each end of the half stroke, and this forward/backward asymmetry in wing rotation is also associated with forward thrust. Asymmetries in wing flip timing are associated with asymmetries in pitch angle between the two wings. In addition, a translational phase may be present in one wing without being present in the other.

We use these measured wing motions, along with quasisteady aerodynamics, to study the stability of mosquito motion. Using the numerically robust rigid body simulation software TREP ([41]), which implements the rigid body kinematics formulation presented by Murray et al ([53]), we impose symmetric wing motions in an insect with mosquito geometry. Instead of using time averaged aerodynamics to study stability, we impose aerodynamic forces at each step of numerical integration during the wingbeat. Although Wu and Sun find that eigenvalue results have shown good agreement between flapping and time averaged calculations ([84]), examining their results, there is disagreement in the largest singular values associated with the two methods. These singular values are important.

Much insect flight stability work focuses on asymptotic stability and thus the eigenvalues associated with the insect motion map ([27], [28], [85]. Examining eigenvalues, we find that mosquito motion is weakly stable at higher forward velocities and weakly unstable below 0.26 m/s. This stability result is similar to that found for bees by Xu and Sun ([85]). Mosquitoes

have sensory feedback that likely operates on timescales from just a few milliseconds with the halteres ([62]) to tens of milliseconds with the visual system ([81]). Because of this feedback, we are interested in their control environment over timescales of tens of wingbeats. Examining the short timescale growth of perturbations by computing the largest singular value gives us insight into the stability landscape on timescales of up to 80 wingbeats. For all wing motions that we examine, we find that non-normality of the Jacobian matrix leads to singular values of 1.76. Based on the work of Wu and Sun, droneflies have a largest singular value of 1.61, which is similar. These large singular values are present whether or not the insect's motion is asymptotically stable based on the eigenvalues of the Jacobian. The presence of large singular values means that, on timescales of up to 80 wingbeats, arbitrary perturbations both grow and rotate. The growth rate of perturbations is governed by these singular values, rather than by the eigenvalues of the system. Longitudinal perturbations, which impact forward or upward motion as well as pitch or pitch velocity, are rotated towards alignment with a singular vector that is not far from a pure pitch mode by the action of the map associated with body motion during flight. The presence of large singular values, which rotate perturbations, may simplify the control landscape by limiting the range of impacts caused by arbitrary perturbations to those associated with the largest singular vectors of the longitudinal and lateral cases. Because these singular values are not well captured by time averaged computations, the inclusion of flapping and rigid body interactions are important to understanding the full control landscape of these insects.

In summary, we use motion capture data to generate measurements of position and orientation of mosquito bodies and wings during flight. Using these wing data, along with rigid body simulation software, we examine the stability of mosquito motion. We find large singular values that will drive perturbation growth along particular directions for up to 80 wingbeats of flight, before long term stability considerations become dominant. We also characterize mosquito motion, finding that most turns are driven by sideslip based mechanisms and that changes in yaw are less frequent and smaller in amplitude than changes

in flight direction. The sideways accelerations that drive these changes in direction are well explained by deflection of the lift vector via roll. In contrast, many mechanisms contribute to forward acceleration in mosquitoes, and body pitch based mechanisms do not make a dominant contribution. This work begins the process of characterizing and explaining the motion of mosquitoes and creates a number of open questions for further study.

Chapter 2

Insect heading and yaw turns during flight

2.1 Introduction

In this chapter, we present measurements of the mosquito's body yaw during free flight. This is the orientation of its longitudinal body axis in the horizontal plane relative to a fixed coordinate system. We compare the body yaw to the insect's horizontal flight direction. The body yaw angle determines the orientation of the insect's visual and auditory systems, and is central to understanding the insect's interaction with its visual environment during flight. The flight direction is described using the course angle, which is the angle of the projection of the velocity vector into the horizontal plane in the same fixed coordinate system. We specifically investigate the slip angle, which is the difference angle between the body yaw and the course angle, during free flight.

Amongst Dipterans, in fruitflies, the slip angle is thought to be approximately zero during flight ([71], [19], [75], [52]). In blowflies, the slip angle is often small, but the insects sometimes exhibit sideways or backwards flight, so the slip angle can reach 180 degrees ([6]). For hoverflies and houseflies, the slip angle is frequently nonzero ([12], [32], [77]). Non-Dipterans

such as bees and moths also often fly sideways ([6]). Such motion corresponds to large slip angles. Moths in pheremone plumes maintain an upwind body orientation while engaging in zigzagging flight formed of cross wind legs ([87]), so the slip angle can be near 90 degrees for these flight legs. In mosquitoes, female *Anopheles Gambiae* mosquitoes exhibit cross wind flights when flying in a CO_2 plume, but their slip angle has not been explicitly measured ([3]). In swarming flights of male mosquitoes, the individuals are described as facing upwind ([22]), while in constant to-and-fro motion, and likely have a nonzero slip angle in such flights. For the *Aedes aegypti* males measured here in free flight, we find the slip angle varies from 0 to 180 degrees, and that the insect is oriented more than 20 degrees away from forward in almost 70 percent of flights. This is more frequent oblique flight than in hoverflies, where they fly more than 20 degrees away from forward in about 55 percent of flights, based upon data from [12].

In mosquitoes, the slip angle changes during flight. This is in contrast to fruitflies ([52]), but also occurs to some extent in hoverflies ([12]), and is common in houseflies ([77]). We examine the types of maneuvers that drive these changes in slip angle. Other small flies often exhibit straight segments interspersed with rapid turns. In hoverflies and houseflies, such turns can involve rapid changes in body yaw, frequently termed 'saccades', or may be sideslipping turns, where the body yaw angle changes very little, while sideways accelerations produce rapid turns ([12], [77]). In such turns, the slip angle often changes dramatically. In fruitflies, rapid turns are assumed to involve yaw saccades and are not associated with changes in slip angle ([71]). We find that mosquitoes also fly using relatively straight flight segments that are interpersed with rapid changes in flight direction. In mosquitoes, these rapid changes in direction are nearly always due to sideslipping turns, and are associated with large changes in slip angle.

Mosquitoes also change slip angle via yaw saccades that are not accompanied by commensurate changes in flight direction. Saccadic turns have been well described in blowflies. Blowflies in nearly free flight exhibited frequent saccade-like turns, turning tens of degrees

in $20 - 30$ ms, at a rate of about ten turns per second ([64], [44]). During saccadic turns in blowflies, the head moves at lower rotational velocities, but does exhibit a similar pattern of turns ([36], [65]). Mosquitoes do not exhibit yaw saccades nearly as frequently as blowflies. When they do, they can turn up to 90 degrees in approximately 40 ms. Saccadic yaw turns induced by visual stimulation in tethered flies, as well as in free flight, are frequently studied in fruit flies because of their importance to flight heading in these insects ([38], [39], [52], [29], [4], [21], [19]). In fruit flies, these turns can take longer lasting up to 80 ms ([4]).

In addition to sideslipping turns and rapid yaw saccades, mosquitoes sometimes display small oscillations in their body yaw angle. These oscillations involve the thorax and the head with typical amplitudes of less than 5 degrees and a timescale of approximately 30 ms from peak to peak. These rapid, small, oscillations, lead to comparable changes in slip angle.

2.2 Methods

2.2.1 Generating Motion Capture Sequences

The *Aedes aegypti* mosquitoes used in this observational work were bred by Cornell entomologists in the Harrington lab. One to two days after emergence the mosquitoes moved from a temperature and humidity controlled environment to less environmentally controlled conditions on bench space near the motion capture apparatus. In this space, they were kept on a twelve hour light/dark cycle using a timed incadescent light and a drape to isolate the insects from overhead lighting, with access to a solution of sucrose and water for food. The humidity in their enclosure was raised by leaving dishes of water within the drape near the enclosures. Humidity ranged from 12 to 31 percent r.h. and was typically about 25 percent rh. Temperature remained between 20 C and 27 C at all times. This temperature is within a range for mosquitoes that is optimum for mosquito flight performance ([61]). Rowley and Graham also found that flight activity was not sensitive to humidity at these temperatures.

To record mosquito flight, we used the motion capture system described in [59]. The ob-

servational system consisted of three perpendicularly aligned high speed cameras (Phantom), a transparent flight chamber, LED lights on the far side of the chamber from the cameras along with a power system for the lights, a data acquisition computer, a trigger to indicate when to download images from the cameras to the computer, and an incandescent bulb to maintain the temperature of the chamber. Because the LED lights are across the flight chamber from the cameras, the insects appear as dark silhouettes on a bright background in the motion capture footage. During recording periods, the cameras were recording continuously with a continuous display of one camera view on the computer. When the trigger was depressed, the contents of the camera memory for a period of time before and after the trigger would be downloaded to the computer. This triggering was done by hand when the mosquito was seen in focus on the camera image on the computer screen.

Ninety flights were recorded at 13029 frames per second, which yields about 15 frames per wingbeat, and a camera resolution of 384×384 pixels. At this frame rate, it is possible to analyze the wing motion of the insect, as well as its body motion. Another 173 flights were recorded at 6309 frames per second, with a camera resolution of 592×592 pixels, allowing a larger region to be imaged. we aligned the cameras, starting with the XZ side view, so that the imaging resolution was approximately 16 pixels per mm. To estimate this imaging resolution, we recorded a 1 cm by 1 cm square marked with a millimeter grid. By clamping the square in the center of the flight arena, and adjusting each camera's distance to the center, we set all three cameras to yield an identical resolution. In addition, the cameras needed to be aligned so that they were perpendicular to each other. The overhead camera was hung so that it was automatically perpendicular to the optical table. The side view cameras would tilt slightly relative to the table, and this tilt was corrected by adding weights to the camera mount. Affixing a needle to a translation stage, and translating the needle parallel to the table, we determined whether the side view cameras were aligned parallel to the table, and adjusted their alignment.

In all data acquisitions, mosquitoes were transferred to a 15 cm by 15 cm acrylic chamber

with six transparent sides. This enclosed the mosquitoes and prevented outside air currents from perturbing their flight. The chamber was placed using a magnetic mount so that its position on the optical table was easy to adjust. For most experiments, the chamber was aligned so that the center of the chamber was at the center of the camera field of view. At times, the chamber was shifted so that the side wall was in the field of view. Insects were transferred to the chamber via mouth aspirator in the morning, shortly after the onset of the lighted period in their enclosure. In the 6309 fps recordings they were shaken out of the aspirator. In the chamber, they never had access to food, but they would often have access to a small dish of water placed in a corner of the chamber to raise the humidity. The chamber was typically loaded with about twenty unmated male mosquitoes, and would have a maximum of thirty-five. The mosquitoes were more likely to respond to stimuli early in the day, and most days of observations included just a few hours of flying time. After that point, the insects would become less responsive and instead of crossing the chamber, would land nearby whenever they were induced to take off.

Most flights were recorded with insects between five and ten days old. Outside of this window, the insects were less likely to respond to flight stimuli. This is consistent with the findings of Rowley and Graham in [60], where they found a substantial drop in flight ability after two weeks for *Aedes aegypti* females. However, in their work, the insects flew actively on a flight mill from shortly after emergence. In my observations, the mosquitoes were particularly willing to fly on the seventh or eighth day afer emergence, when they would fly in response to motion outside of the chamber. In addition to being less responsive to flight stimuli, older insects would often lose some of their legs and have tattered wings.

To remove mosquitoes from the flight chamber, we sedated the mosquitoes by placing the chamber in a refrigerator for ten minutes. we then transferred the sluggish mosquitoes from the chamber into a fresh bucket with food. After cleaning the chamber with ethanol and allowing it to dry, we would introduce new mosquitoes into the chamber.

In the flight segments recorded at 13029 fps, insect motion was induced with a 400 Hz

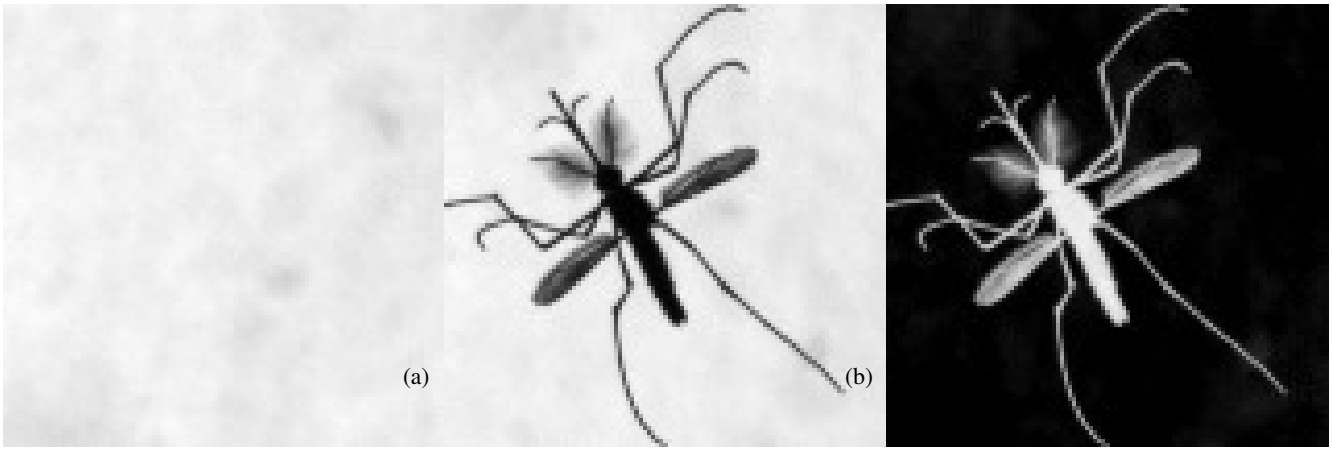

Figure 1: The raw image, shown in b, is subtracted from a background image, show in a, to yield an analysis image, shown in c.

flight tone played on an iPod speaker in the chamber, with exposure to human breath odors, or by tapping on the chamber. In the 6309 fps flights, flight was induced via a looming stimulus by moving my hand towards the chamber, by tapping or rubbing a gloved finger on the outside wall of the chamber near where an insect was standing on the inside, or with a flying female whose flight induced male flight. To generate female flight, we would spur an individual female to fly either by rubbing a gloved finger on the outside of the chamber where she was resting, or by threading a long stick through a 2 mm hole in the side of the chamber and gently touching the back legs of a resting female. The latter stimulus was always sufficient to trigger her to fly. Once a female was in flight, males would then take flight. Sometimes this would cause another female to fly, creating a cycle of motion in the chamber that could take minutes to settle down. During these mixed male and female flights, the chamber would have approximately 30 initially virgin male mosquitoes and two to four initially unmated females. The insects were replaced at the beginning of the day.

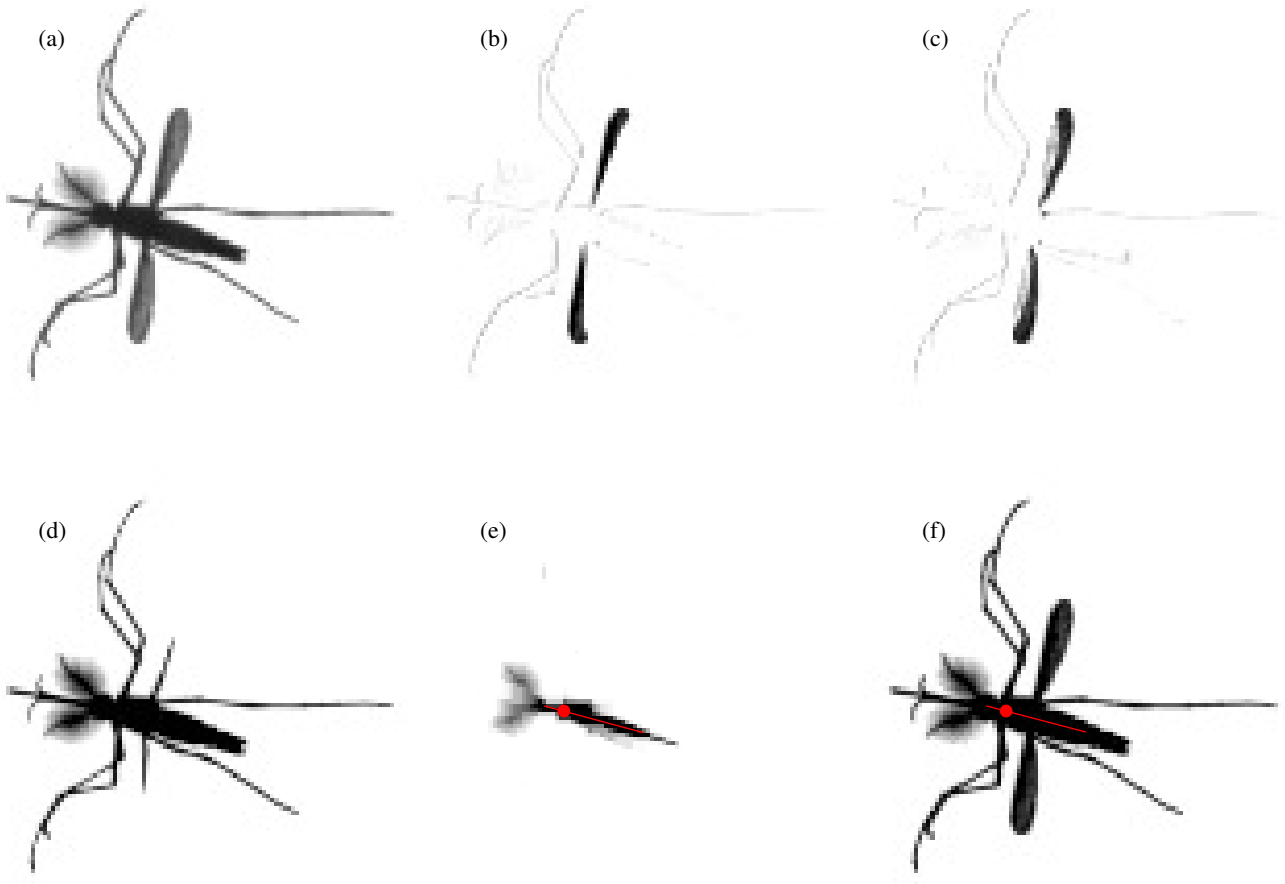

Figure 2: An image of the mosquito after background subtraction, but without further processing, is shown in (a). In (b) we show the result of subtracting a prior frame from the current frame, isolating leading edge pixels of the wings. In (c) we have subtracted a subsequent frame, isolating trailing edge pixels. Subtracting both (b) and (c) from (a) yields (d), an image where most of the wing pixels are eliminated and the wings are retained as thin features. These thin wings and the legs are removed using image erosion, where each pixel intensity is replaced with the lowest intensity from within a $4x4$ box surrounding the pixel. The result of erosion is shown in (e). Calculating the mean pixel location for the remaining pixels, as well as their orientation, yields the point shown by a red dot in (e) and (f) as well as the direction indicated by the thin red line.

2.2.2 Extracting Orientation from Motion Capture Data

Data from the Overhead View

To process the motion capture data for the purpose of observing predominant patterns of insect motion, we extract position information and body orientation information using a series of image processing algorithms. The methods presented are slightly different than those used for similar data from flies ([59]). This is necessary because the geometry of the mosquito body is different from that of a fly. Mosquitoes are more slender, with an abdomen that is connected to the thorax at an angle of approximately 30 degrees. This angle is generally fixed, although we observe changes during male/female tandem flights. We consider the body axis to pass through the thorax and head of the insect, with the abdomen tilted away from the body axis. Using a reference frame connected to the thorax to define the yaw, pitch, and roll of the insect, means that it is necessary to segment the abdomen from the thorax in our image analysis. This segmentation is unnecessary in flies, where the abdomen, thorax, and head form a line. In addition to these differences in body geometry, mosquito wings move through very short wing strokes compared to flies, and are often occluded in images by the mosquito legs. This makes it important to use the wing vein as an indicator of stroke angle, rather than an average angle based upon the whole wing. Here we describe methods for processing the overhead view, measuring the position of the body in the horizontal plane, as well as the body yaw angle. In Chapter 3 we present additional methods that enable us to measure all six degrees of freedom of the body. Methods for determining wing position and orientation are described in Chapter 4.

In the initial processing step of each image, we subtract the raw image from a background image in which no mosquito is present. In figure 1, we show a background image, a raw image, and the analysis image that is the result of subtraction. Images are captured sequentially, so we use frames that are near a particular frame in time or that have a similar wing position to aid in data extraction. To identify body position and orientation using frames of motion

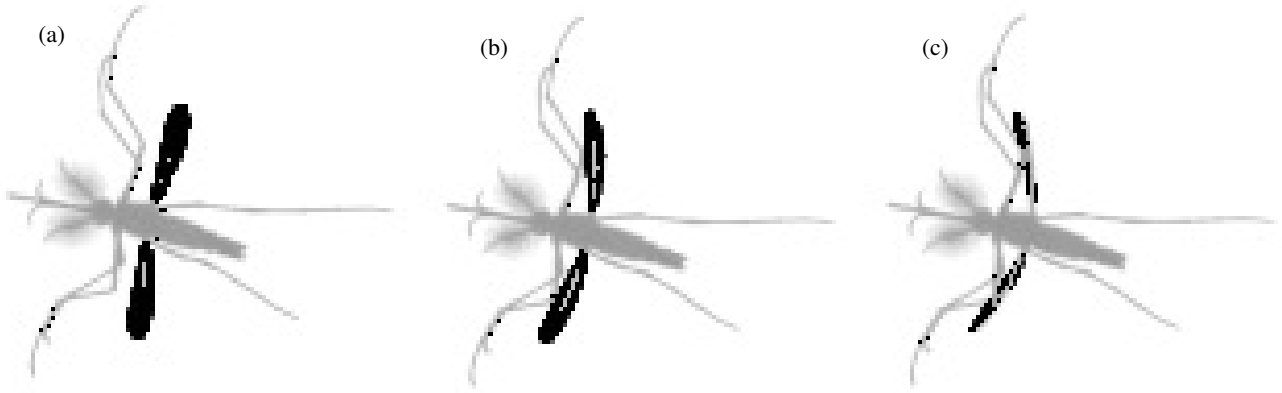

Figure 3: Pixels counted as part of the wing for the wing area estimate are superimposed in black on an insect viewed from overhead at three different phases of a wing stroke.

capture data from the overhead view, we remove pixels associated with the wings and legs, and then use averaging and principal components analysis to assign a position and orientation to body pixels that remain. Wing motion and rotation is much faster than body motion, so subtracting frames that are nearby in time eliminates most body and leg pixels and isolates wing pixels. In figures 2b and 2c we show difference images created by subtracting a frame 1/8 of a wingbeat behind or 1/8 of a wingbeat ahead of the current frame, respectively, where figure 2a shows the analysis image for the current frame. These are plotted as black insects on a white background for ease of display. Mainly leading edge wing pixels are captured in 2b, and mainly trailing edge pixels in 2c.

Summing these two difference images, and counting the number of pixels present, allows us to approximate the wing area visible from overhead in each frame. Pixels identified using this method are shown in black in figure 3. In frames where the wings are nearly horizontal, as in 3a, the measured area is large. When the wings are more vertical, as in 3c, the measured area is smaller. Since the wing is rotating as it flaps, the area signal is periodic. It is low at the ends of the wingbeat, since the wing becomes vertical during the wing flip, and it is relative high during the center portion of the stroke where the wings are often at approximately 45 degrees from horizontal, and sometimes plunge to near 0 degrees

just after the wing flip. In figure 4b the periodic wing area information drawn from 8 ms of a motion capture sequence is shown. To compute wingbeat frequency, we use a fast fourier transform on sequences of 250 to 350 frames of data. Because the area signal is always positive, the measured frequency is twice the wingbeat frequency, and must be adjusted to yield the wingbeat frequency. The results of these frequency measurements are discussed in Chapter 4.

Subtracting the difference images that include mainly wing pixels from the analysis image leaves behind a thin wing remnant, and is a step towards isolating the body pixels. The body image from figure 2a, with the difference images that are shown in 2b and c subtracted, is shown in figure 2d. After subtraction, the body is the only wide object remaining in the image. The legs and wing remnants can be removed using image erosion. In image erosion, the intensity value of each pixel is replaced by the smallest intensity value in an p by p box around the pixel, where the pixel is at the center of the box when p is odd and skewed up and to the left of center when p is even. Erosion eliminates the narrow leg and wing features, leaving behind the centerline of the body and a dim remnant of the antennae. The result of such an erosion, in this case with $p = 4$, is shown in figure 2e.

To identify pixels near the centerline of the insect, we apply an intensity threshold to this eroded image. The mean coordinate of the pixels with intensity above threshold is used as the (x, y) position of the body and is indicated by a red dot in figure 2e. The point is also plotted on the analysis image in figure 2f. We use the direction of the first principal component vector through these pixels as an orientation measurement. It serves as an initial estimate of the insect's yaw angle. Because the abdomen of the insect deflects to the side when the insect is rolled, and many abdomen pixels are part of the identified centerline, this orientation is skewed by the body's roll, and is not a pure yaw measurement We distinguish the orientation of the thorax from that of the abdomen for a better measurement of yaw angle. In Chapter 3 we will use this differentation to estimate the roll angle of the insect. The principal component orientation is shown by a red line in figures 2e and f and is plotted for

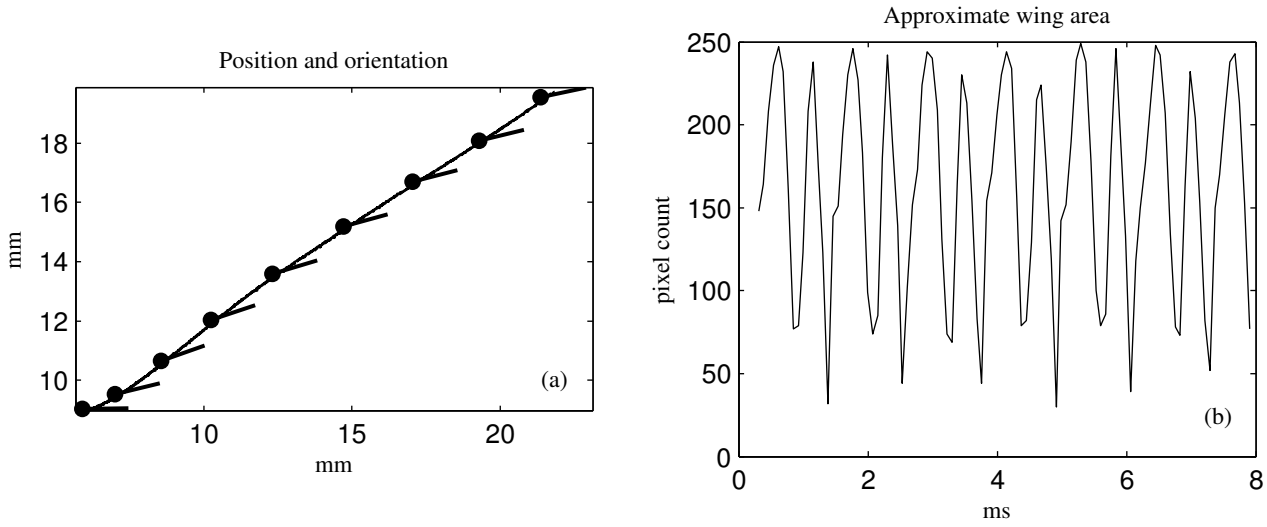

Figure 4: On the left, body position and orientation data are shown over the course of a motion capture sequence. The dot indicates the insect's head, and the line to the right its measured orientation. The thin line in the background is the insect's measured trajectory. On the right, approximate wing area is shown over the course of 6.5 wingbeats. A single wingbeat consists of two cycles, one peak corresponding to a point in the forward portion of the stroke and the other peak corresponding to a point in the backward portion.

a motion capture sequence in figure 4a. In the figure, the position of the body is plotted as a thick line and is marked with filled circles at times where the orientation is being displayed. The orientation of the body is shown via a line segment pointing from the head towards the tip of the abdomen. The circles are located every 16.9 ms, or approximately every 13.5 wingbeats, and are shown for a 143 ms motion capture sequence.

Measuring Orientation

To measure the thoracic yaw, we will use the thorax, head, and proboscis of the insect in the overhead view. Because the thorax is an ellipsoid with a ratio of less than two between the smallest and largest radii, it is not an elongated feature. Using an edge based method where we identify the edges of the thorax and create a centerline based on the edge positions, which is the technique we use to identify the yaw angle of the abdomen in Chapter 3, thoracic yaw measurements had a standard deviation of 4 degrees, a large error. For this reason, we do not use the thorax alone to identify yaw, but instead estimate thoracic yaw by finding the

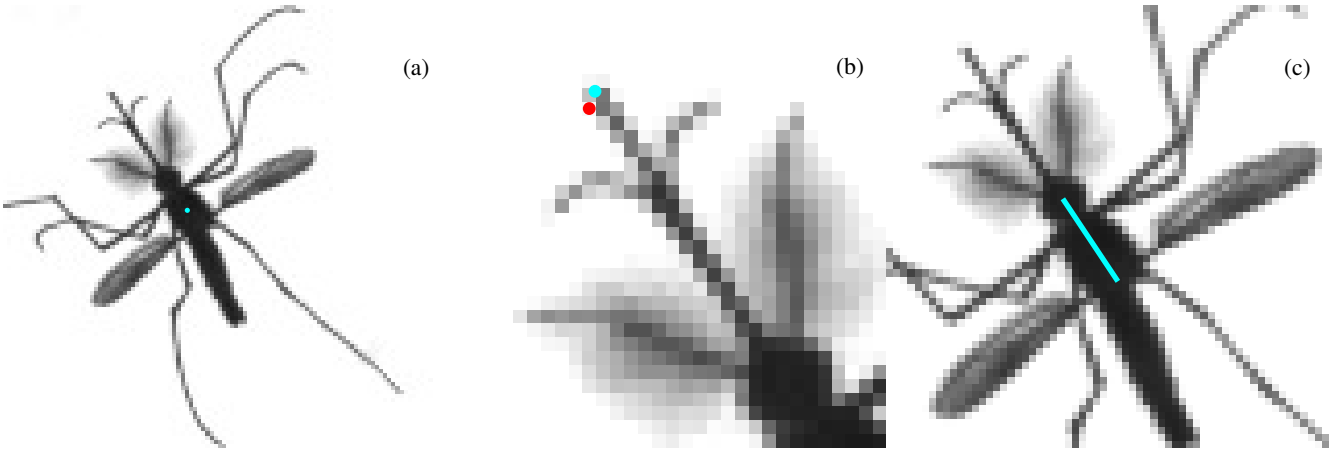

Figure 5: To generate the thoracic yaw measurement, we use a point centered within the thorax and connect it to the tip of the proboscis. This vector acts as a thoracic yaw measurement. In Chapter 4 we measure thoracic position via mean wing location, and the two measurements are in close agreement. To identify a point in the thorax, we fit a quadratic function to the intensity profile of a cross section. We then select the point associated with the maximum. That point is shown as a cyan dot in (a). We also identify the tip of the proboscis by using cross correlation to find the tip to subpixel accuracy given a nearby initial guess. The guess is shown as a red point in (b) and the refined point is in cyan. The direction of the vector between these two points serves as our yaw measurement. The vector, centered on the thorax, is shown in (c) as a cyan line.

orientation of a vector drawn from the tip of the proboscis to the center of the thorax. To find the center of the thorax, we use the thorax position measurement (x, y) described above, and center it along the intensity profile of a cross section of the thorax using a quadratic fit to the intensity. When the initial measurement and the centered measurement are within a 2 pixel neighborhood of each other, we consider the measurement to be good. We use a spline fit to these measurements as the thoracic center point. In figure 5a, the insect is shown with its thoracic location plotted in cyan. To identify the proboscis tip, we begin with an estimate of its location and orientation. Using the orientation, we create a template shaped like the tip of the proboscis. We use cross correlation to identify the point of maximum similarity to the template near the estimated location. The initial estimate either comes from using the initial orientation computed for the xy view along with the point on the body farthest from the abdomen as the location or from the location and orientation in a prior frame. The initial estimate is a red dot and the refinement a cyan dot in figure 5b. In 5c we plot the measured vector as a cyan line. The standard deviation of the thoracic yaw measured with this technique is 0.24 degrees, so this is a low noise measurement. There is the potential that the proboscis moves independently of the head and that the head moves relative to the thorax during flight. We use the average of the two wing stroke angles as an independent source of yaw data, as described in Chapter 4 and find that the two measures agree at almost all times.

Computing Velocity

We use the functional data analysis package for Matlab, described in [57] to calculate the velocity of the insect using the position measurements described above. To compute the velocity, we use cubic b-splines with knots spaced every 2 ms, which is every 1.6 wingbeats for an insect with an 800 Hertz wing beat. We balance the smoothness of the second derivative with the fitting error on the position data, using a balancing factor λ, with $10^4 \leq \lambda \leq 10^7$. The value of the generalized cross validation is minimized when $\lambda \approx 10^{4.5}$

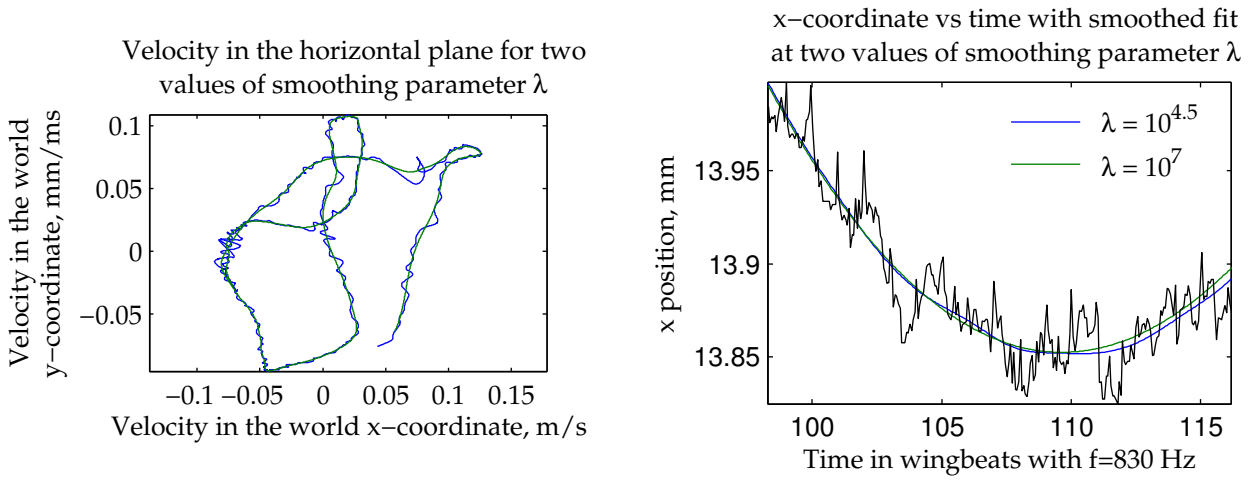

Figure 6: In (a) the blue line shows x-velocity for a single flight at a smoothing level of $\lambda = 10^{4.5}$, a low smoothing. The green line is the velocity information computed as $\lambda = 10^{7}$, a higher level of smoothing. The two different computed velocities produce similar trajectory data, which is shown in (b) for the x-coordinate over the same segment of flight. The position measurements for the x-coordinate, shown in black, are noisy on this short timescale.

2.3 Results

2.3.1 Changes in slip angle

Male mosquitoes exhibit swarming behavior that is central to their mating, but which is poorly understood ([8]). Without information on mosquito slip angles during flight, it is not possible to begin to reconstruct the insect's sensory experience during swarming and chasing flights. This requires measurements of mosquito body yaw angle and course angle during flight. Because the velocity vector is tangent to the flight path, the x and y components of the velocity are used to compute the course angle. This angle is aligned with the horizontal-plane projections of the flight path at all times. This computation requires taking a numerical derivative of the horizontal position data. Even with high fidelity data, there is a noise signal in the body position data. The measurement method is slightly dependent on the phase of the wingbeat, leading to small variations on a one wingbeat timescale. In taking the derivative, we must determine the smoothness of the signal so that the derivative corresponds to change

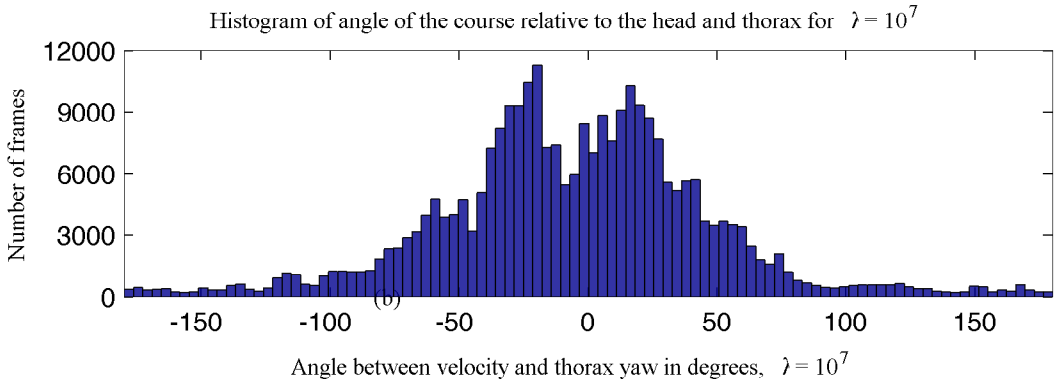

Figure 7: The slip angle (the difference between the body yaw angle and the course angle) is peaked away from zero, meaning that the body axis is often offset from the flight direction, and sideways motion is an important component of mosquito flight. Pure sideways flight, where the slip angle is 90 degrees, and pure backwards flight, where the slip angle is 180 degrees, are both relatively rare. 32 percent of frames are oriented within 20 degrees of pure forward flight, while 9 percent of frames are oriented within 20 degrees of pure sideways flight.

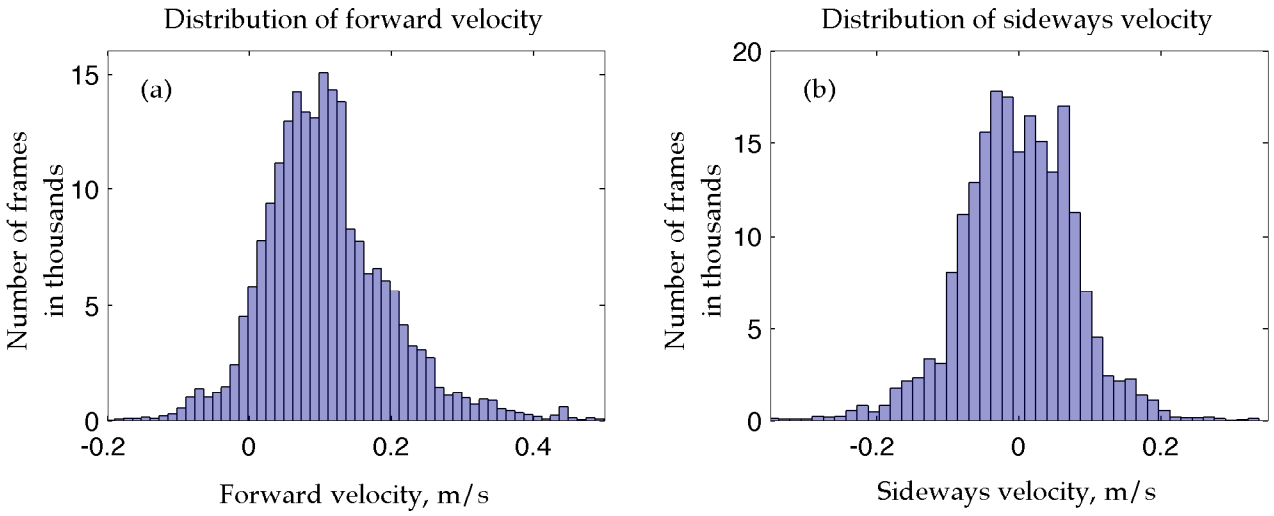

Figure 8: Mosquito velocities are shown broken in their forward components (see (a)) and their sideways components (see (b)). The distribution of forward velocity is similar to that found for hoverflies flying in a large enclosure ([32]).

in the underlying signal, not to rapid changes in position that are actually due to the noise process. To create this trade off between signal and noise, we use the functional data analysis package. We choose to use a b-spline fit to the data, placing nodes slightly less than once each wingbeat. Computing the derivative requires making a trade-off between how closely the b-spline fit matches the raw data and how spiky the second derivative is. With a perfect fit to the data, we are fitting the data as well as measurement noise, and the second derivative will oscillate rapidly and have high curvature. The relative importance of each of fit and low curvature is controlled by the smoothing parameter, λ. For a given value of λ, the spline fit is chosen to minimize the sum of squares error in the fit added to the net curvature weighted by λ. Increasing λ leads to a smoother curve with less oscillation in the second derivative, and decreasing it leads to a close fit to the measured data and noise. The variation of velocity measurements with smoothing is shown in figure 6. The oscillations visible in the velocity when the derivative is computed using lower values of the smoothing parameter have little impact on measurements of the course angle or magnitude of the velocity, so these results are not sensitive to the choice of λ. The difference between levels of smoothing becomes much more significant in acceleration calculations, as discussed in Chapter 3. The distribution of forward and sideways velocities during all recorded flights are shown in figure 8. The forward velocity distribution is similar to that of the hoverfly *Eristalis tenax* in a large arena (fig. 2 of [32]).

Figure 7 shows the relationship between the course angle and the body axis direction. There is little variation in the distribution with smoothing, so results for other values of the smoothing parameter are not shown. In this histogram, the orientation of the insect is peaked away from zero, where zero indicates exact alignment between the longitudinal body axis and the flight path in the horizontal plane. The mean of the positive side of the histogram is 37.7 ± 34.7 degrees, while the mean of the negative side is -42.8 ± 35.0 degrees. Although the insect occasionally exhibits pure sideways flight or nearly backwards flight, 32 percent of frames are oriented within 20 degrees of pure forward flight, while 9 percent

of frames are oriented within 20 degrees of pure sideways flight. A similar histogram for the hoverfly *Syritta pipiens* (fig. 12 in [12]) is peaked at zero, with about 45 percent of flight segments within 20 degrees of forward, and about 10 percent of flight segments within 20 degrees of pure sideways flight. The most substantial difference in orientation between these insects is that mosquitoes usually have a moderate to large sideways component to their motion, while hoverflies sometimes have little to no sideways component. Assumptions of gaze alignment with flight path, such as those that are common for fruitflies ([71], [19], [75]), are inappropriate for mosquitoes. Instead, direct observations of body alignment are necessary to draw conclusions about the magnitude of the slip angle at any instant. The predominance of sideways motion in mosquitoes may relate to their small roll moment of inertia, as Nematocera have slender bodies relative to Brachystera, and *Aedes aegypti* have a smaller stroke angle even than hoverflies (Chapter 4, [24]) potentially leading to reduced wing-based damping during roll.

The slip angle is typically nonzero, and also changes substantially during flight. Three examples of such changes are shown in figure 9(a), (b), and (d). In 9c is shown an example where the body axis and course angle change in tandem, resulting in little change in the slip angle. In the first row of the figure, lines are drawn at $-45, 0, 45$, and 90 degrees for reference and the slip angle is shown as it changes over time. In the second row of the figure, the body yaw angle (blue) and the course angle (black) are plotted for the same time interval and flights as in the first row. The trajectories associated with these changes are drawn (black) in the third row with the orientation of the body axis plotted as well. The head is a small dot (blue) and the body a thin line (blue).

In the first and second columns of figure 9, the insects undergo rapid changes in flight direction by utilizing sideslipping turns. During such turns, we find that changes in flight direction of over 100 degrees occur in as little as 35 ms (see figure 10). These turns are characterized by the generation of substantial sideways accelerations. The generation of sideways acceleration, which in mosquitoes is well explained quantitatively by the tilt of

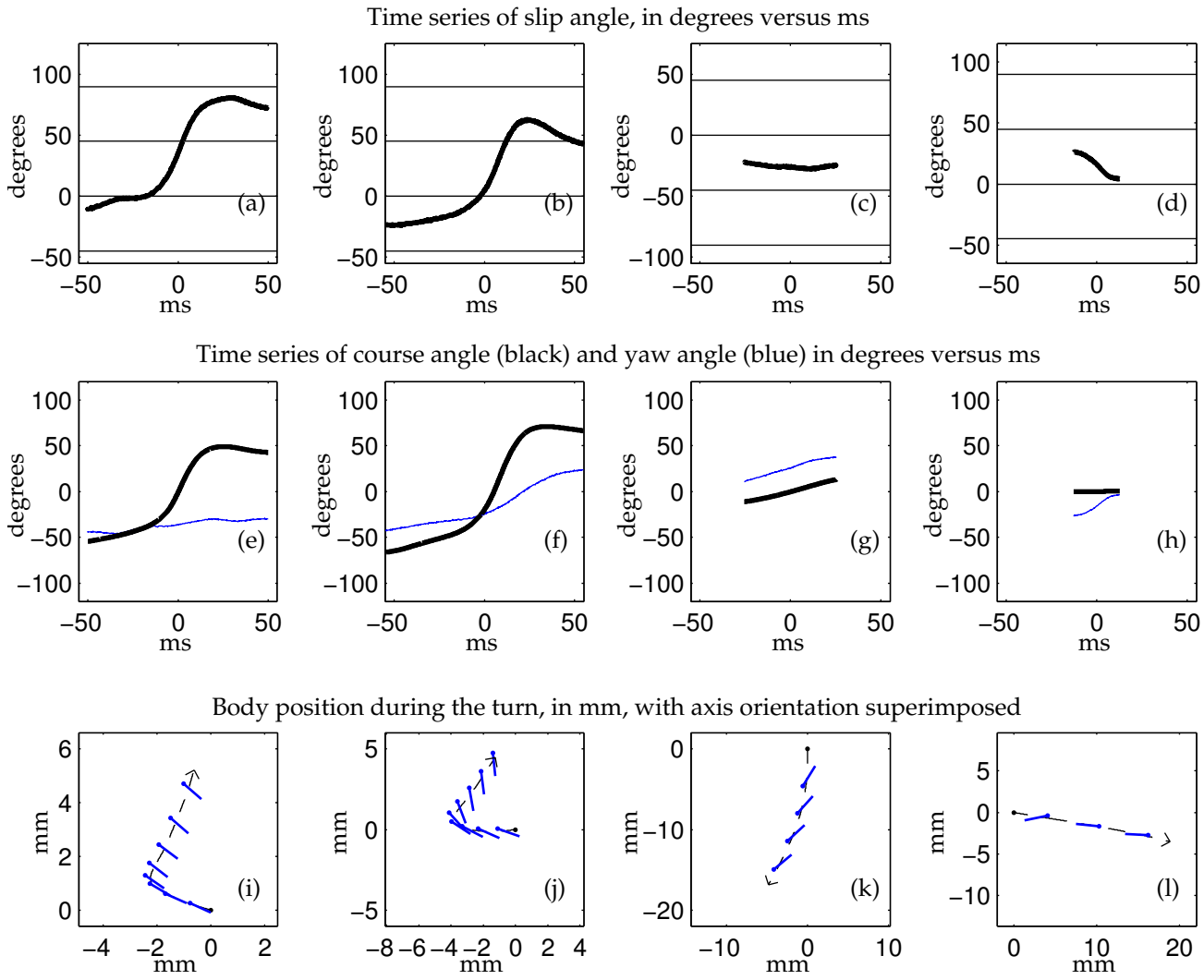

Figure 9: In this figure, we show four scenarios where either the slip angle, or the body yaw angle, changes during flight. In (a), the slip angle changes by 80 degrees in 35 ms. In (e), we show that this change in slip angle is driven by a rapid change in course angle (black line), accompanied by little change in the body yaw angle (blue line). The relationship between the trajectory (black) and the body angle (blue) is shown in (i). In the observed mosquitoes, changes in direction that are this rapid always correspond to turns with a large sideslipping component, such as this one. In the second column, the change in slip angle seen in (b) is due to a rapid change in course angle (black line in (f)) of over 100 degrees in 35 ms, accompanied by a slower, smaller, change in yaw direction, of 55 degrees in 50 ms (blue line in (f)). The trajectory and body angle for this flight are shown in (j). In the third column we show a yaw turn during which there is only a slight change in slip angle, as shown in (c), because the body yaw angle (blue line) and course angle (black line) change simultaneously (shown in (g)). In this turn, the body yaw changes by 40 degrees in 80 ms. In the fourth column we show a yaw turn where there is a commensurate change in slip angle (shown in (d)) because the course angle remains unchanged during the insect's yaw turn. The course angle (black line) and body yaw angle (blue line) for this turn are shown in (h) with the trajectory and body orientation shown in (l). This is a yaw turn of 20 degrees in 25 ms.

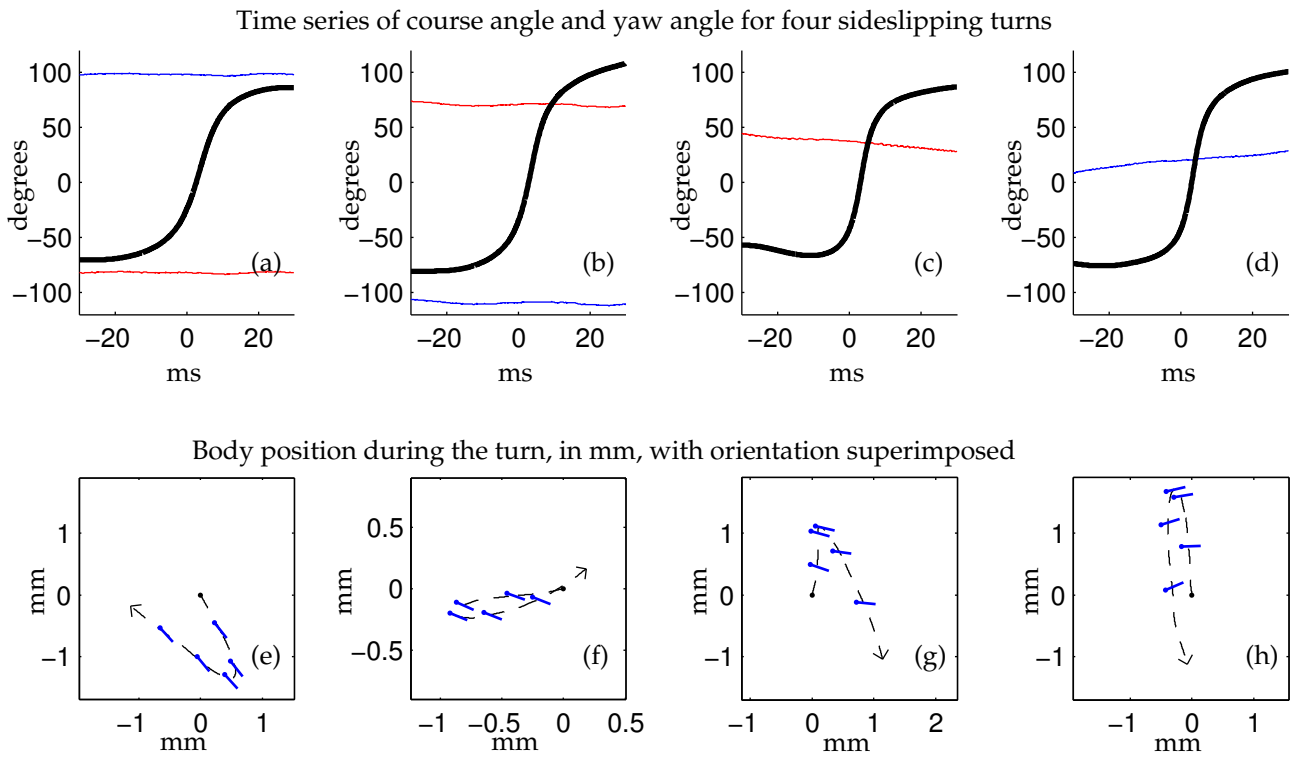

Figure 10: In the first row, the course angle (black) and body yaw angle (blue) are plotted versus time for four different sideslipping turns. In these turns, large changes in flight direction occur, and are not accompanied by rapid changes in body yaw angle. The backwards direction, 180 degrees offset from the body yaw, is also shown (red). In the second row, the corresponding flight trajectories are plotted (black) with the body orientation superimposed (blue).

their lift vector via roll, is discussed in chapter 3. During such rapid turns, rapid changes in body yaw may or may not occur. Such changes are always substantially smaller than the change in course direction. For the flight detailed in the first column of the figure, body yaw changes very little during the sideslipping turn, while for the flight shown in the second column, body yaw changes at a rate of approximately 1000 degrees/s, a rate typical of rapid yaw turns in mosquitoes (see figure 11(a)). Yaw turns also occur independently of changes in flight direction. An example of this type of turn is shown in the fourth column. In this case, the slip angle changes because the body yaw angle is changing while the course angle is not.

Rapid changes in flight direction that correspond to large changes in slip angle occur

frequently in mosquitoes. Using a rotation threshold of 400 degrees/s to define a turn, as in [44], we find that 54 percent of rapid changes in course angle ($N = 272$) are turns where the change in course angle is not accompanied by a yaw turn. In the extreme case, the flight direction nearly reverses in just 25 to 35 ms. Such large turns are observed in blowflies, where they have been referred to as U-turns. In blowflies, these turns are less common than are rapid changes in body yaw ([64]). For mosquitoes, sideslipping turns, including U-turns, are the most common type of turn. Four U-turns are shown in figure 10. They are distinguished by rapid changes in course angle accompanied by only small, slow, changes in body yaw angle. For each turn shown, the relationship between the course angle and the body angle is different. In the first column, the insect is moving backwards as it enters the turn and leaves moving forwards. In the turn in the second column, the insect is flying somewhat forward as it enters, and leaves flying with a backward component to its motion. In the turn in the third column, the insect is moving almost sideways, and is facing away from the turn direction. Finally, in the turn in the fourth column, the insect is also sideways, but is facing the turn direction. Sideways thrust is central to the actuation of these turns, and the mosquito simultaneously generates either forward thrust (columns 1 and 4) or backward thrust (columns 2 and 3). Because similar turns occur at a range of slip angles, when such turns are detected by identifying rapid changes in trajectory, there is no straightforward way to predict the orientation of the insect as it enters and exits the turn. Instead, estimating its orientation during motion requires direct measurement

In 46 percent of cases, rapid changes in flight direction are accompanied by yaw turns. Although both the course angle and the body yaw angle are undergoing rapid change in such turns, the body yaw angle often changes more slowly than the course angle. An example of this is shown in the second column of figure 9, where the course angle changes by 125 degrees while the body yaw angle changes by only 70 degrees. Across all turns, the body yaw angle rarely changes at rates faster than 1000 degrees/s. This is shown in the histogram on the right side of figure 11, where the turning rate rarely exceeds 10^3 degrees/s. Changes

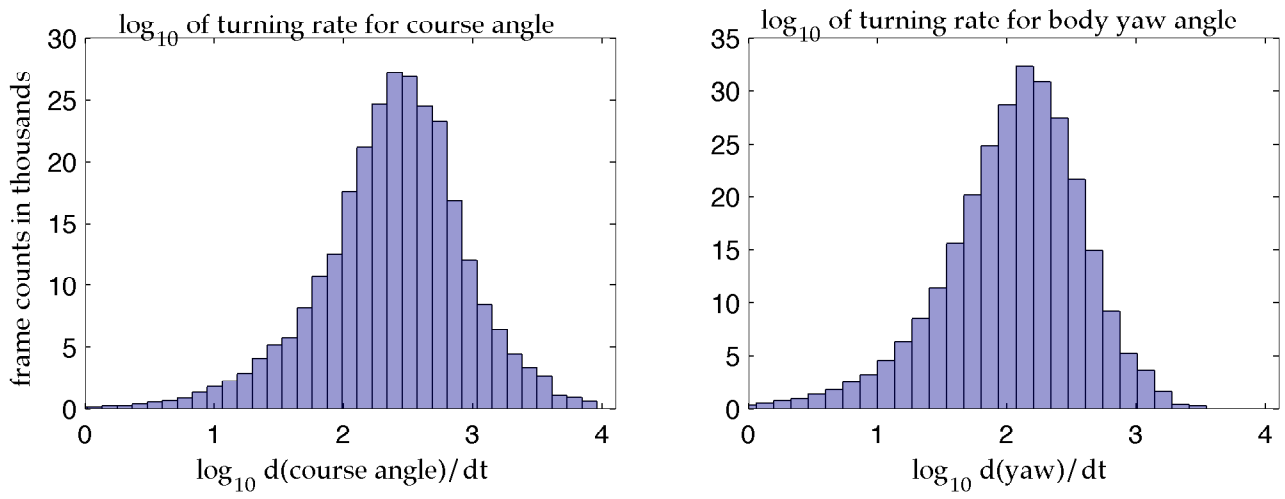

Figure 11: In the histogram on the left, the distribution of the $\log_{10}$ of the rate of change in the course angle is shown. Changes in course angle can occur at rates of over 3000 degrees/s. In contrast, the histogram on the right shows the distribution of the $\log_{10}$ of the rate of change of the body yaw angle, relative to a world-fixed coordinate frame. The rate of change of the body yaw angle exceeds 1000 degrees/s only infrequently. Because of this, changes in flight direction that involve rotations of more than 1000 degrees/s are very likely, in mosquitoes, to be sideslipping turns.

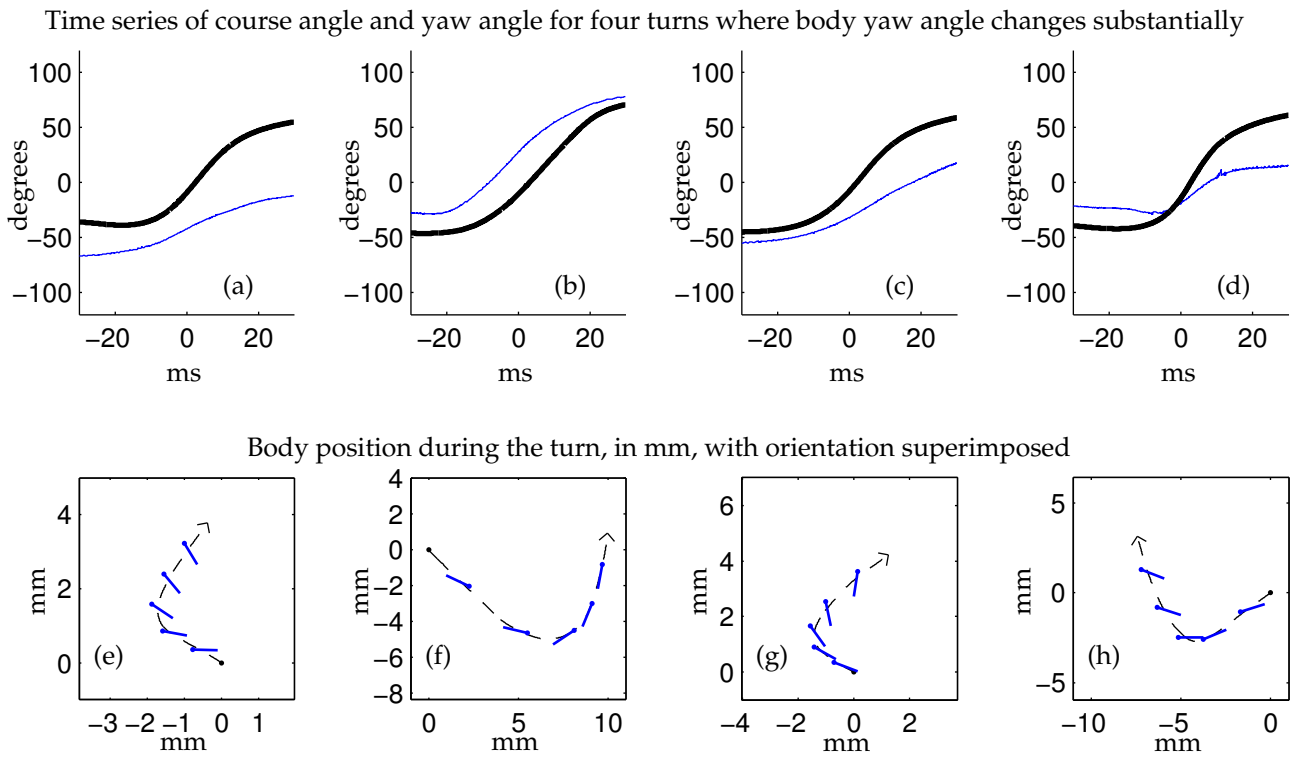

Figure 12: In the first row, the course angle (black) and body yaw angle (blue) are plotted versus time for four different turns involving large changes in body yaw angle. The yaw turns shown here last approximately 50 ms and involve directional changes of up to 50 degrees. In these turns, large changes in flight direction also occur. In (a), (c), and (d), these course angles changes are substantially larger than the changes in body yaw angles, which leads to changes in the slip angle. In the second row, the corresponding flight trajectories are plotted (black) with the body orientation superimposed (blue).

in course angle are frequently much more rapid, not infrequently reaching 3000 degrees/s, as seen in the histogram on the left side of figure 11. Mean turning rates are a factor of two larger for the course angle than for the body yaw angle. This contrast in turning rates results in significant changes in the slip angle during these maneuvers. For turns where the course angle changes by at least 20 degrees over the course of the turn, with the start and end of the turn considered to be the times where the rate of change of course angle drops below 200 degrees/s, the slip angle also changes by more than 20 degrees in 86 percent of the time ($N = 145$).

Four examples of turns where the body yaw angle is changing rapidly are shown in figure

12. In figure 12(a), (c), and (d), the slip angle changes substantially even as the yaw angle changes, while in (b) the slip angle only undergoes a moderate change. In the flights shown in the second and fourth columns, the slip angle is such that the body axis of the insect is tilted slightly towards the direction in which it will be moving after the turn. In the other two flights it enters the turn oriented away from its next direction. The variation in possible body orientations before and after turning events makes it difficult to predict mosquito slip angle without direct measurement.

Although it is rare, the body does at times turn in tandem with the change in path direction, in a true banked turn. The maximum rate of change of the body yaw is within 5 percent of that of the course angle in 3 percent of observed course angle turns. An example of this situation is shown in the third column of figure 9, where the body angle and course angle change in concert.

Just as rapid changes in course angle are sometimes accompanied by change in the body yaw angle, and are sometimes not, the body yaw angle can change without the insect changing direction. An example of this type of turn, where there is a yaw turning event but no course angle turning event, is shown in the fourth column of figure 9. In that turn, the body starts at a slip angle of 26 degrees and finishes at a slip angle of 4 degrees, while the course angle changes by only 1 degree. There is no accompanying course angle turn in 38 percent of body yaw turns ($N = 231$). Changes in the slip angle can be driven by changes in course angle alone, by changes in body angle alone, and by rapid changes in course angle accompanied by slower changes in body yaw angle.

2.3.2 Yaw oscillations

Large changes in body yaw are relatively infrequent, with turns of more than 20 degrees happening only once in every 900 ms of flight. This is in contrast to blowflies, where body yaw saccades happen approximately every 100 ms ([64]). Although large shifts in body orientation occur rarely in mosquitoes, small shifts occur almost constantly. The body yaw

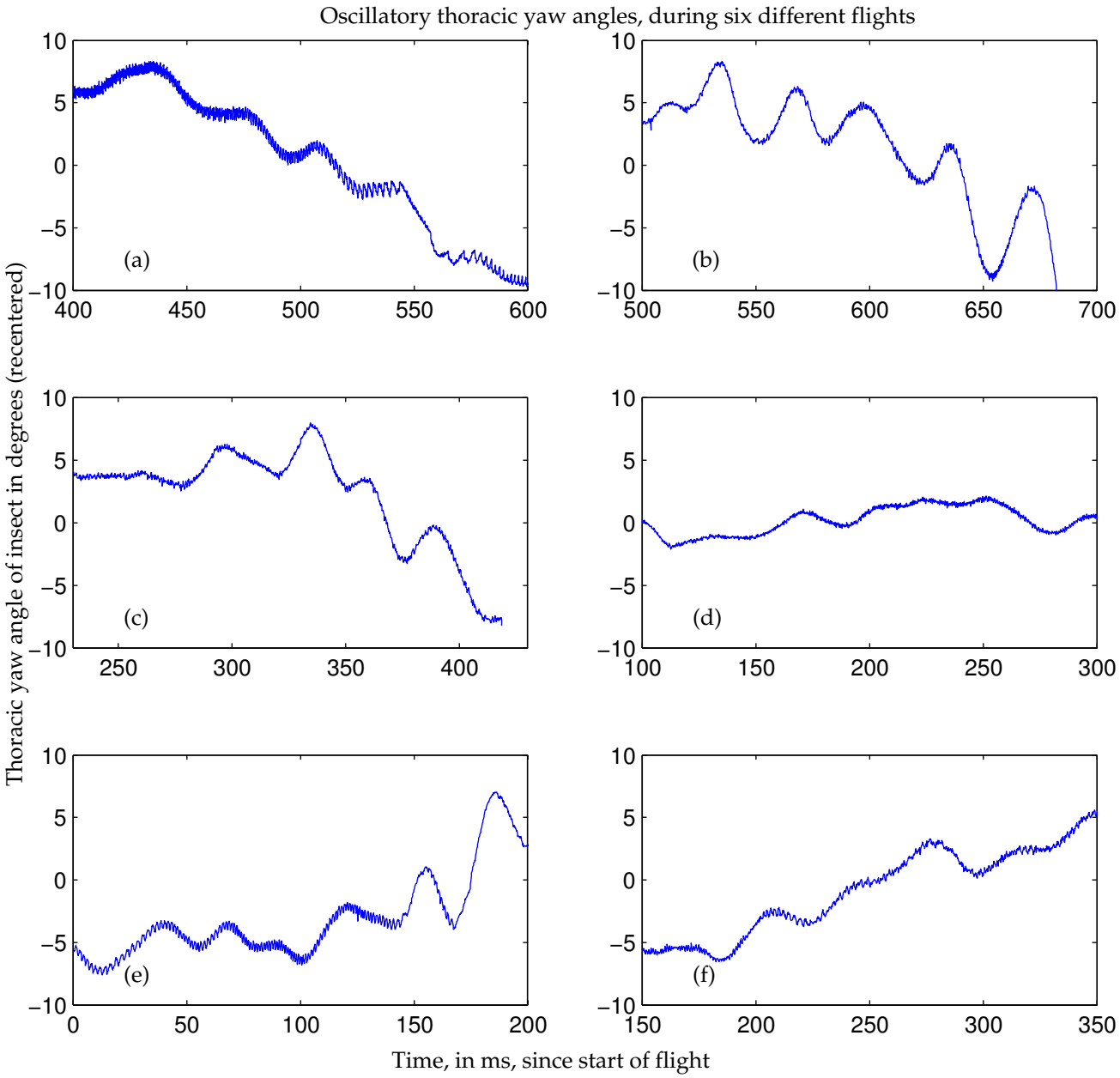

Figure 13: The six flight segments above each show a pattern of small oscillations in yaw. These are 200 ms segments excerpted from six distinct flights. The yaw angle, shown in degrees, has been recentered. The oscillations are between 1.5 and 5 degrees in amplitude have a mean peak-to-peak duration of 27.6 ± 10.4 ms. There is also a small oscillation visible in these yaw measurements on a one wingbeat timescale. Its amplitude is less than one degree and it is present because the yaw measurement algorithm is sensitive to the phase of the wingbeat. The 1 to 5 degree oscillations on a 30 ms timescale are observed in nearly all flights, and are more visible when there is a low background turning rate.

orientation is changing at a rate above 45 degrees/s in 79 percent of frames. These small rotations correspond to oscillations of approximately one to six degrees in body yaw. These oscillations, which can be seen in graphs of the body yaw angle as it changes over time for six different flights in figure 13, are also visible in wing data and in proboscis orientation data, so represent an oscillation of the thorax and of the head. The oscillations have a mean peak-to-peak interval of 27.6 ± 10.4 ms and occur in most flights. These oscillations occur on a timescale similar to that of fly visual processing systems ([81], [47]). Oscillations of this magnitude have been observed in other Dipterans on a single wingbeat timescale ([24]). The oscillations described here last tens of wingbeats, so are not due to inertial effects acting over a single wingbeat. These oscillations may be passive, rather than actively driven, as weakly stable oscillatory motion of the lateral system, which in mosquitoes includes sideslip, yaw, and roll, is a prediction of multiple flight stability models ([28], [90], Chapter 5).

2.4 Discussion

In observations of hundreds of free flights, mosquitoes frequently change their flight direction, with rapid changes of flight direction usually actuated using sideslipping turns. In these mosquitoes, yaw rotation rarely exceeds 1000 degrees per second, so rotational speeds above this value can be used as an indicator of sideslip during the turn. Sideslip-based turns are also observed in hoverflies ([32], [12]), and infrequently in blowflies ([64]). In more than half of the sideslip-based turns we observe, there is not an accompanying rapid change in the body yaw angle, so the insect's body yaw angle, and thus its sensory system orientation, change little during the turn. During a search process, where the insect is using sensory information to identify its target, there may be advantages to maintaining a consistent sensory orientation. In particular, if odor information is coming from upwind, then an upwind body heading could be advantageous even as flight is crosswing. This type of flight pattern is seen when moths track a pheromone plume upwing ([87]). Flight paths of female mosquitoes in odor

plumes are similarly meandering to those of moths ([3]), so it is potentially the case that mosquitoes use such a search strategy. Males have been observed to orient upwind during flight in swarms ([22]) while flying to and fro. Such flight may be actuated by sideslipping. During swarming the insect may face upwind so that it can maintain its flight position near a swarm marker while countering downwing advection. We observe many sideslip-based turns in free flight conditions without the presence of an odor plume or a swarm. Based on our observations, such turns are a central part of the insect's flight repetoire.

When a sideslipping turn is accompanied by a simultaneous yaw turn, the yaw turn typically results in body rotations that are much smaller in magnitude than the change in flight direction, so there is a change in the insect's slip angle. The slip angle also changes when the insect undergoes a body yaw turn that is unaccompanied by a change in flight direction. Almost 40 percent of body yaw turns are of this type. In these mosquitoes, the slip angle is more than 20 degrees in almost 70 percent of flights, and frequently changes, so the body angle and the flight direction are usually out of alignment. When changes in slip angle occur during a sideslipping turn, there is a detectable change in the flight direction. However, the magnitude of the change in slip angle varies. If a sideslipping turn also has a yaw component, then the change in slip angle is smaller than the change in flight direction. When changes in slip angle occur during a yaw turn, there may be no rapid change in flight direction. This makes the slip angle, and changes in the slip angle, unpredictable from flight trajectory information alone. In fruitflies the insect's sensory system is thought to align with its flight path ([75], [52], [70]). For mosquitoes, such an assumption is inappropriate.

Understanding mosquito visual experience during flight requires measuring both body position and orientation. For the *Aedes aegypti* mosquitoes observed here, based on examining images created by summing multiple frames recorded at 13000 frames per second, body position and orientation could be resolved clearly using frame rates as low as 600 frames per second, with noisy measurements still possible at 150 frames per second. Algorithms that use the insect's flight speed and direction to account for image blur could potentially

be developed, possibly creating accurate orientation measurements at lower frame rates.

Yaw does not play a clear dynamic role in mosquitoes, since the yaw angle is decoupled from their flight direction. Changes in yaw angle could potentially occur passively, as a result of coupling between yaw and roll or because of the effects of instability. The yaw angle of the insect is rarely constant and is usually changing by tens of degrees per second. The yaw angle sets the direction of the sensory system, so may be actively controlled for sensory reasons. We present observations of small oscillations in yaw angle that occur on a timescale of approximately 30 ms, or tens of wingbeats. These oscillations may be a passive signature of an oscillatory instability, or may occur under active control by the insects, perhaps aiding in sensory perception.

Chapter 3

Assessing a "helicopter model" of thrust generation

3.1 Introduction

In a tilt-based model of thrust generation, the insect uses its wing motion to generate a lift force, and then redirects that lift force by adjusting the angle of its stroke plane relative to horizontal. In tethered fruitfly flight, it has long been known that there is a direct relationship between the body angle and the direction of the net thrust vector ([76]). For forward flight, this relationship has also been found in free flight in a wind tunnel ([14]). Recent work has found a nearly exact fit between such a tilt model and forward acceleration in free-flying fruitflies ([50]). At the same time, a fruitfly's flight speed can be varied by wing-based mechanisms that act independently of the body pitch angle. Ristroph et al identified a downstroke/upstroke wing asymmetry resulting in a paddling stroke that generated sufficient forward thrust to balance drag during flights at different constant velocities ([58]). In female houseflies, Wagner ([77]) did not find a strong relationship between body pitch and forward velocity, while in males there is such a relationship. He also observed that, at times, male houseflies generate thrust that is aligned with the body axis, so the relationship between

body pitch and net longitudinal thrust direction is not necessarily straightforward in this insect. In locusts, the direction of the net force is less dependent on body angle ([89]). This is also the case in the hoverfly *Eristalis tenax* (also referred to as a dronefly) ([78]). The use of body angle adjustments for generating forward thrust appears to be species specific.

For sideways thrust generation, results in fruitflies have indicated that sideslipping may be driven by directly generated thrusts, rather than solely by tilting the lift vector via roll ([59], [68]). In blowflies, directly generated sideways forces also exist, and have about 1/4 the magnitude of directly generated forward forces ([2]). In houseflies, however, roll and sideways motion have long been known to be related ([77]), and this relationship has also been suggested for moths ([87]).

In male *Aedes aegypti* mosquitoes we probe the relationship between the tilt angle of the body or stroke plane and horizontal acceleration. We find that stroke plane roll almost entirely explains measured sideways accelerations in these insects, and that neither body pitch nor stroke plane pitch based tilt of the lift vector appears to be the dominant mechanism for generating forward accelerations. Because we measure the orientation of the body separately from that of the stroke plane, we also examine the relationship between these frames. Also, since sideslipping, roll-based, turns are much more common than yaw turns in mosquitoes (Chapter 2), we look at the relationship between roll and yaw in this insect.

3.2 Methods

Motion capture sequences were generated as described in Chapter 2. Horizontal position information as well as the thoracic yaw angle were extracted from the motion capture data as described in Chapter 2.

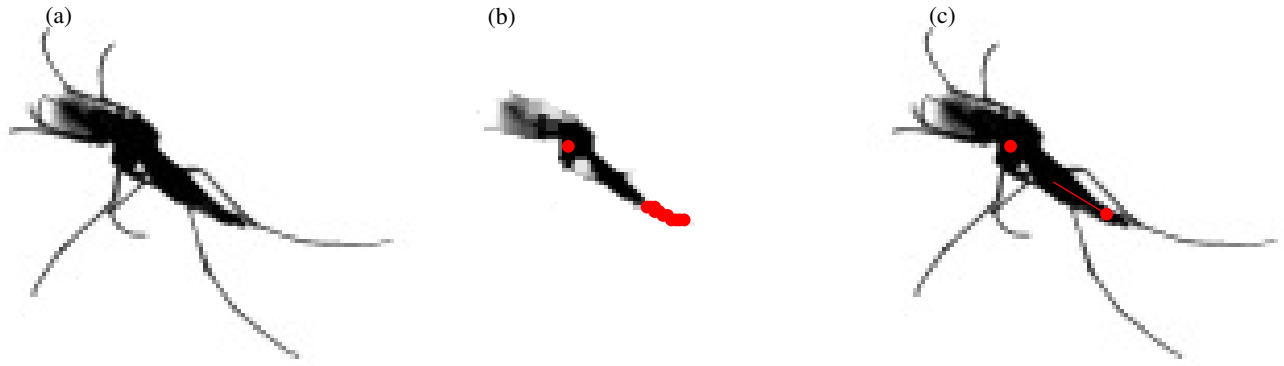

Figure 14: Using the xz view of the insect, we extract (x, z) coordinates of the insect as well as the location of a point along the abdomen and the approximate abdomen orientation.

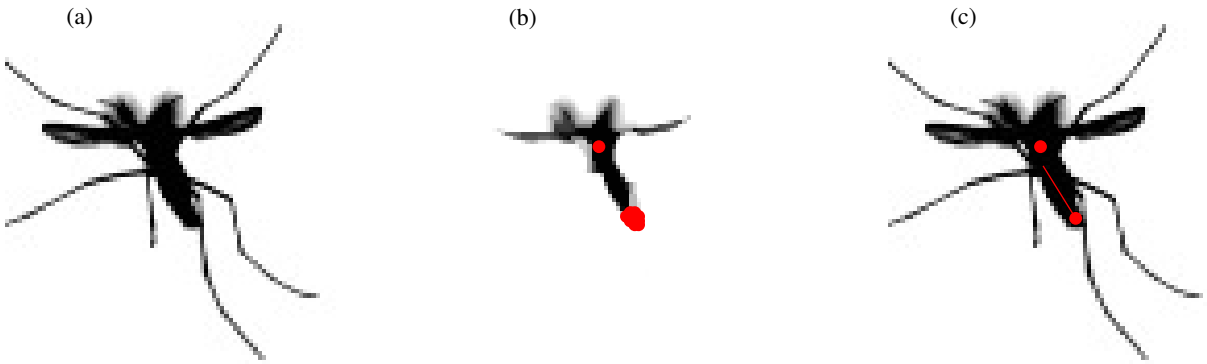

Figure 15: Similarly, for the yz view, we extract (y, z) coordinates, a point along the abdomen, and the approximate abdomen orientation. Depending upon the yaw orientation of the insect, the angle of the abdomen is more clearly visible in either the xz or the yz.

3.2.1 Extracting Position and Orientation from Motion Capture Data

To identify the z-coordinate of the body, the position of the abdomen, and abdomen orientation data, we process the side views of the insect using similar techniques to those described for extracting (x, y) position and yaw in Chapter 2. In the side views, the change in wing position from frame to frame is not large, so frame differencing is less effective in eliminating the wings. Despite that, we apply the same frame differencing techniques described above to subtract off as much of the wing as is easily identifiable. We then use an erosion width of $p = 3$ to erode away legs and wing remnants. This smaller width is necessary because the abdomen is a more slender feature in the side views. With the eroded images, shown in figures 14b and 15b, we use pixel intensity thresholding to identify pixels in the body. The mean pixel location, (xy_0, z_0), is indicated by a red dot on the thorax of the insect. We measure these locations for every frame of the motion capture sequence, and fit smooth lines through the measured locations, using cubic splines with derivative smoothing. For all numerical derivatives, we use fitting package *fdaM*, a functional data analysis package for Matlab, which is well described in [57] and is also described in Chapter 2. This allows us to estimate the location in frames where the central body is occluded momentarily in one of the views. To construct the (x, y, z) trajectory of the insect we retain the unsmoothed x and y coordinates identified in the overhead view and the unsmoothed z coordinate identified in the xz view.

Using the smoothed (x_0, z_0) or (y_0, z_0) positions, we identify all pixels that are within the eroded image and have a z coordinate such that they are located below the line $z = z_0$. Because the abdomen hangs down below the thorax, this criterion excludes the antennae and much of the thorax. For this reduced set of pixels, the slope of the principal component line through the pixels gives a measurement of $m = \Delta z/\Delta x$ or $n = \Delta z/\Delta y$. This line is shown in 14c and 15c as a red line. Using the reduced pixel set, we also identify ten pixels that maximize $(xy_p - xy_0)^2 + 4(z_p - z_0)^2$, where (xy_p, z_p) is the position of a pixel, and use

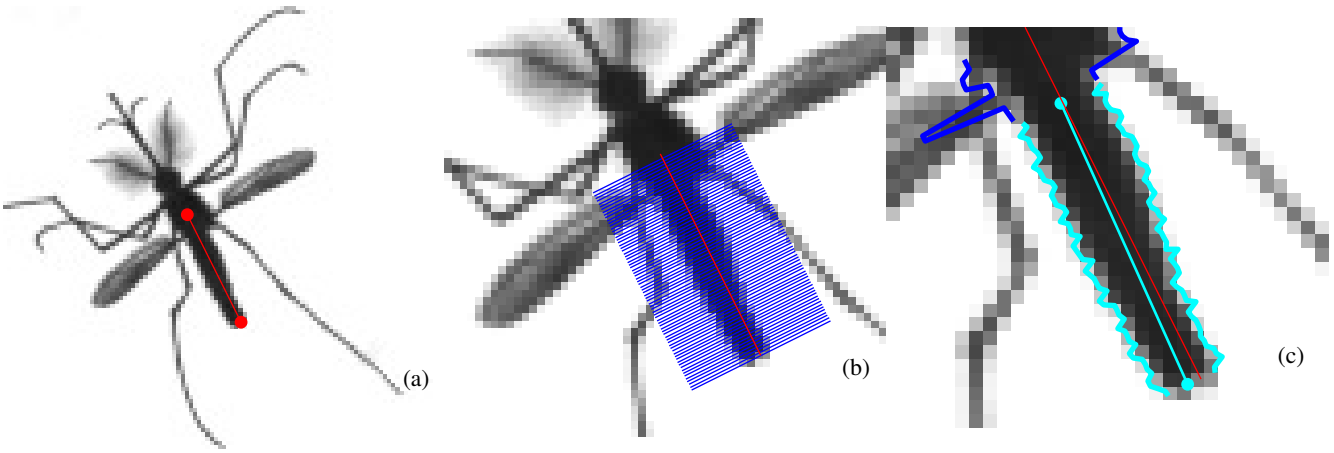

Figure 16: To find a yaw angle associated with the abdomen we analyze the overhead view. First, we draw a line connecting previously identified points in the thorax and near the tip of the abdomen. This is shown in (a). We then take cross sections of the image perpendicular to the line, as shown in (b). Each cross section has an associated intensity profile. Using linear interpolation, we identify points to the left and to the right of the center line where the intensity crosses a fixed threshold (set to 40 for these images). These points are plotted in cyan if they are in the abdomen and in blue if they are not in (c). The distance between the two points on the same cross section is referred to as the insect's width. The separation between abdomen and thorax is designated to be the point where the width first falls below the median width, moving from the thorax towards the abdomen. We find lines of fit for each set of cyan points, and their mean is drawn in cyan on the abdomen. The orientation of this line will be used as the yaw angle of the abdomen. The line joining the thorax and the abdomen tip is also plotted, in red, for reference. The location of the abdomen tip is also updated by this algorithm and is shown with a cyan dot.

the center of these points as the abdomen position. This point is plotted on 14c and on 15c as a red dot. The distance measure is reweighted because abdomen pixels are typically amongst the lowest points remaining in the eroded image. Using the values of m and n for a particular frame, $\begin{pmatrix} -1/m \\ -1/n \\ -1 \end{pmatrix}$ is a vector aligned with the abdomen, and $\sin^{-1} \frac{-1}{\sqrt{1+1/m^2+1/n^2}}$ is a measure of the abdomen pitch.

Combining abdomen information from the two side views is sufficient to create a measurement of the abdomen pitch. However, if the insect is aligned with its body axis along the x-axis, then the abdomen has significant extent in the xz view but is a thin vertical

feature in the yz view. In this case, Δy is nearly zero, leading to large errors in the slope. To avoid this, we find a vector aligned with the abdomen in the overhead view and use its slope, $\Delta y/\Delta x$, as part of the calculation. When $\Delta y/\Delta x > 1$, we use the yz view to contruct an abdomen vector and then calculate the abdomen pitch. Otherwise, we use the xz view for this purpose. The process of finding a vector aligned with the abdomen in the overhead view is illustrated in figure 16. To find a vector aligned with the abdomen from overhead, we draw a line from the thorax to the tip of the abdomen, shown in (a), use cross sections to identify the edges of the insect, shown in (b), and create a line of fit for each edge of the abdomen. The mean of the two lines, drawn in cyan in (c), is a vector aligned with the abdomen. To create the initial vector in (a) we use the point on the thorax identified above, and a point near the abdomen tip. To identify a point near the tip of the abdomen, we use the $\Delta z/\Delta x$ and $\Delta z/\Delta y$ information from above, with $\Delta z < 0$ for a vector pointing towards the abdomen from the thorax, and find the point in the insect furthest from the thorax in that direction. The orientation of this overhead vector aligned with the abdomen is the abdomen yaw angle, so this process yields an abdomen pitch and an abdomen yaw. We also measure the pitch of the stroke plane using a statistical technique described in Chapter 4.

In Chapter 4, we describe how we measure the insect's roll angle using the deviation angle of the leading edge of the wing. To measure the roll angle of the body, rather than of the stroke plane, we use the difference between the thoracic yaw angle and the abdomen yaw angle as a proxy for roll. Let the abdomen join the thorax at the point $(0, 0, 0)$, with the abdomen tip located at point $(-x_A, 0, -z_A)$, and the thorax in a neutral position, so that the roll angle is zero. When the thorax then rolls by angle ψ, the point $(0, 0, 0)$ is unmoved. Once rolled, the tip of the abdomen is deflected to the point $(-x_A, z_A \sin\psi, -z_A \cos\psi)$. In figure 17, the initial body position is shown in dark blue. The lighter colored insect is rolled by $\pi/7$ radians. We use the thoracic yaw angle to define the neutral position. When the insect is rolled, the yaw angle of the abdomen is deflected by α radians where $\tan\alpha = \frac{z_A}{x_A}\sin\psi$. For the insect, $z_A < x_A$ and roll angles are less than 15 degrees, or 0.26 radians, in 95 percent of

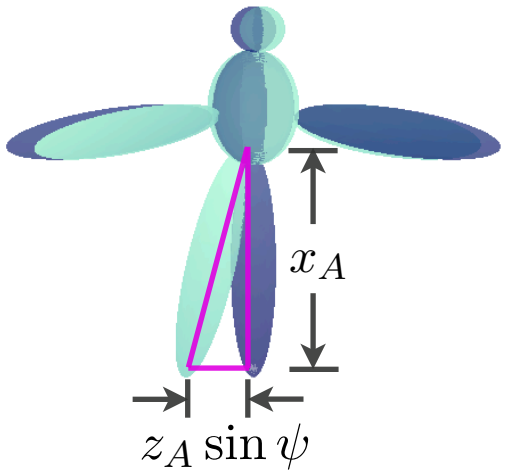

Figure 17: The insect in dark blue has a roll angle of zero while the light colored insect is rolled by $\pi/7$ radians about the body axis, which extends through the center of the thorax and head. The abdomen joins the thorax at the point $(0, 0, 0)$, and the tip of the abdomen is located at $(-x_A, 0, -z_A)$ in the zero roll case. The difference angle, α, is the angle between the centerline of the abdomen of the rolled insect and of the roll zero insect. $\alpha = tan^{-1}\frac{z_A}{x_A} \sin \psi$, where ψ is the roll angle of the insect. For small values of the roll angle, this difference angle is approximately $\frac{z_A}{x_A}\psi$, a linear multiple of the roll angle. The centerline of the thorax and head aligns with the centerline of the abdomen when the insect is not rolled. When the insect is rolled, the difference angle between the centerline of the abdomen and the centerline of the thorax is equivalent to the difference angle between the rolled and the roll zero insect.

wingbeats, so $\alpha \approx \frac{z_A}{x_A} \sin\psi \approx \frac{z_A}{x_A}\psi$. The difference, α, between the thoracic yaw angle and the abdomen yaw angle, is thus approximately a linear multiple of the roll angle.

Computing Acceleration

We use the functional data analysis package for Matlab, described in [57] to compute the velocity and acceleration of the insect using the position measurements described above. To compute the velocity of the insect we use cubic b-splines with knots spaced every 2 ms, which is every 1.6 wingbeats for an insect with an 800 Hertz wing beat. To calculate acceleration we use quartic b-splines smoothed on the third derivative, with smoothing parameter λ where $10^{6.0} \leq \lambda \leq 10^9$. In Chapter 2, *lambda* weighted the curvature of the second derivative so that the functional fit minimized a combination of the curvature and the sum of squares error between the fit and the data. Here, λ is used to weight the curvature of the third derivative. The value of the generalized cross validation is minimized when $\lambda = 10^7$. This is one way of selecting λ. There is oscillatory noise in our measurements on short timescales. On the one wingbeat timescale, measurement techniques are sensitive to the phase of the wingbeat, so we are unable to measure motion of the insect on this timescale. In addition, as the insect translates, the relationship between its position and the pixel grid of the images changes. This occurs on a timescale of five to ten wingbeats, and is another source of systematic measurement error. Although the generalized cross validation suggests that $\lambda = 10^7$ is an appropriate value, the five wingbeat timescale noise is retained as this λ value. By $\lambda = 10^9$ this error signal is no longer impacting the computed acceleration, so we use a value of $\lambda = 10^9$ for our analysis. These results are very sensitive to the choise of λ, as we show below.

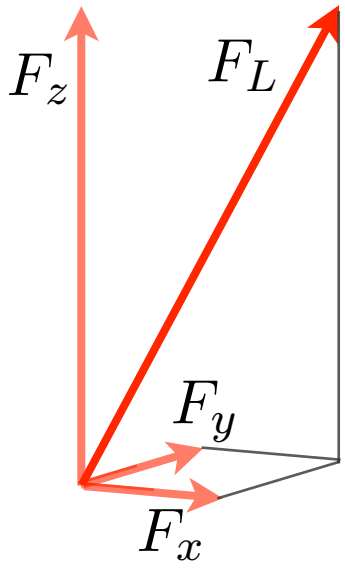

Figure 18: If the insect generates a lift force of $\mathbf{F}_L$ while its body is tilted, this results in an upward force component $\mathbf{F}_z = F_z\mathbf{k}$ and horizontal force components $\mathbf{F}_x = F_x\mathbf{i}$ and $\mathbf{F}_y = F_y\mathbf{j}$.

3.3 Results

The force vectors given a tilt-based model are shown in figure 18. Here $\mathbf{F}_L$ is the lift force generated by the insect, and $F_z\mathbf{k}$, $F_x\mathbf{i}$, $F_y\mathbf{j}$ are the resulting force vector components due to inclination of the lift vector away from vertical. We choose $\mathbf{i}$ to align with the projection of the body axis into the horizontal plane. This is the forward thrust due to tilt, while $F_y\mathbf{j}$ is the sideways thrust due to tilt. Given insect trajectories, we compute $a_z\mathbf{k}$, the vertical acceleration of the insect, where $F_z = m(g + a_z)$, with g is the gravitational acceleration and m is the mass of the insect. Given a measured stroke plane pitch of θ and stroke plane roll of ψ, the resulting horizontal forces from this model are $F_x = m(g + a_z)\tan\theta$ in the forward direction and $F_y = m(g + a_z)\tan\psi$ in the sideways direction. To assess this model in the context of our data, we compare the components of the insect's acceleration along each axis with its measured vertical acceleration, body pitch, and roll. We use both the body-based roll measurement, $\frac{z_A}{x_A}\sin\psi$ in place of $\tan\psi$, and the directly measured stroke-plane based roll angle in the comparison. We also use θ for the abdomen, not the thorax, because the

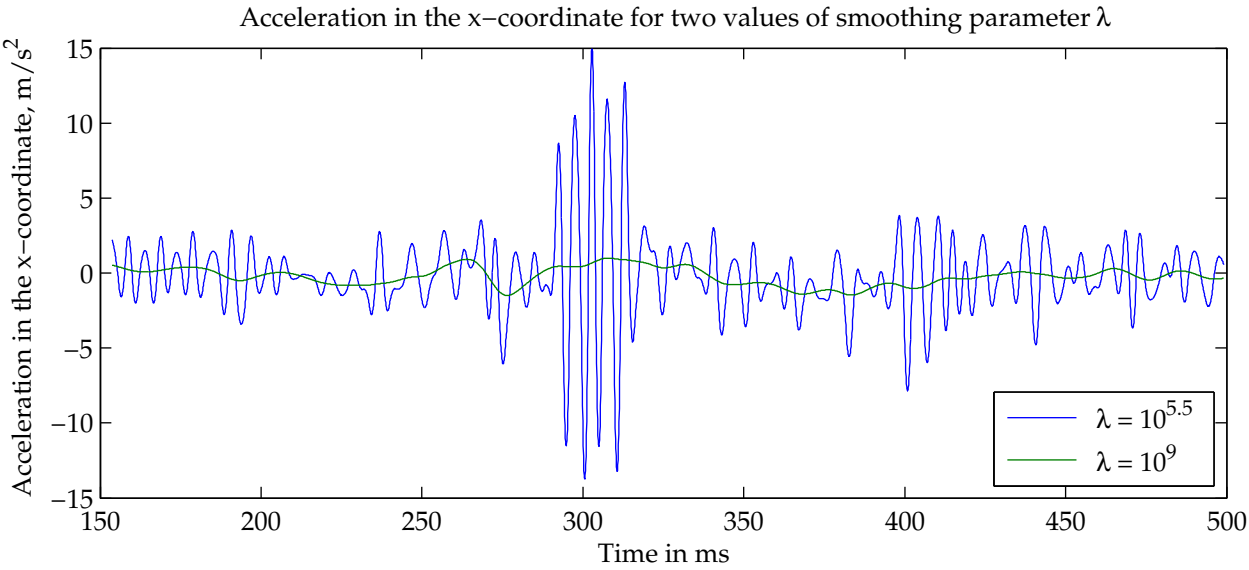

Figure 19: The acceleration along the x direction in the world frame is shown for a 345 ms excerpt of a 840 ms movie. This acceleration is computed using two different values of the smoothing parameter, λ. The $\lambda = 10^{5.5}$ line, in blue, retains high frequency components of the acceleration, some of which are due to measurement noise, while the $\lambda = 10^9$ line, in dark green, is smoother and is not impacted by high frequency noise.

abdomen is a much longer feature, which leads to more accurate measurements, and the pitch angle measured for the stroke plane itself. There is an offset of approximately 30 degrees between these.

Computing acceleration from noisy data requires us to differentiate between signal and noise in the position data stream. The parameter λ controls the tradeoff between smoothness in the acceleration data and a closer fit to the noisy position data. In figure 19, acceleration along the x direction computed with $\lambda = 10^{5.5}$ is shown in blue, with nodes of the b-spline fit positioned in every other wingbeat. At this low smoothing parameter, the acceleration exhibits large oscillations because it is capturing variation that occurs on the single wingbeat timescale. Such variation is due to systematic measurement error, rather than white noise, so $\lambda = 10^{5.5}$ is too low a value of λ. At $\lambda = 10^9$, shown in green, the fast time scale, high frequency, oscillations are no longer present. The frequency spectrum associated with six values of λ, evenly spaced from $\lambda = 10^{4.5}$ to $\lambda = 10^9$ are plotted in figure 20. In figure 20(a),

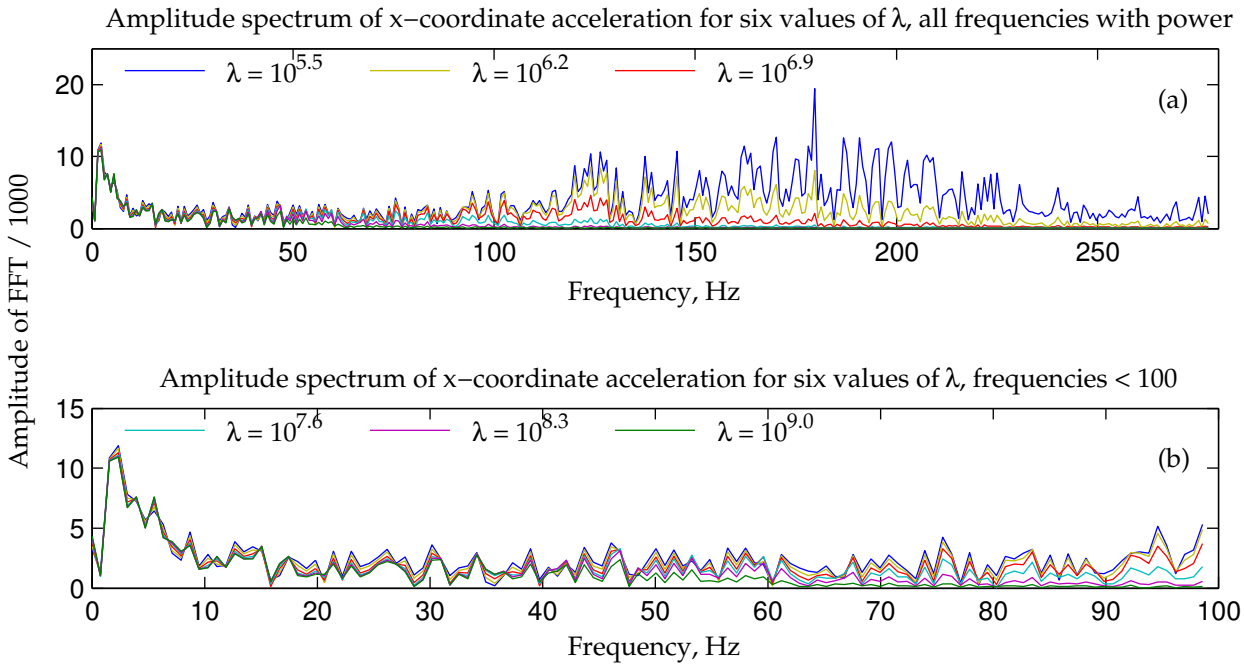

Figure 20: The acceleration along the x-direction in the world frame is computed using six different values of smoothing parameter λ for the 840 ms movie mentioned above. For each acceleration time series, the amplitude of its spectrum is identified using a fast Fourier transform. This amplitude information is shown for frequencies from 0 to 300 in (a) and for frequencies from 0 to 100 in (b). At lower values of λ there is substantial power in higher frequencies. Measurement noise is present on timescales of between one and ten wingbeats, or 800 to 80 Hz, so second derivatives computed using these lower values of λ will be impacted by that noise. At higher values of λ, the high frequency contributions to the acceleration disappear while the low frequency contributions to the acceleration remain. At all six values of λ, the spectrum is similar for frequencies below 50 Hz. This similarity means that the low frequency structure of the acceleration is not sensitive to smoothing. We use $\lambda = 10^9$ to compute the acceleration in much of our analysis, retaining the slower timescale structure of the acceleration.

the spike at 180 Hz in the blue line corresponds to high frequency oscillations in the $\lambda = 10^{5.5}$ acceleration curve above. As λ increases, the high frequency components are damped. At lower frequencies, plotted in figure 20(b), there is little difference in the frequency spectrum between the six levels of smoothing. For $\lambda = 10^9$, frequencies above 50 Hertz, or motions on a timescale faster than 20 ms, are substantially damped while the slower timescale structure of the acceleration is retained. We use this level of smoothing to compute the insect's acceleration for the analysis below because there are no systematic sources of measurement error on such long timescales, and instead we capture the structure of the insect's acceleration. On shorter timescales, systematic noise contributes to the computed acceleration and it is not possible to differentiate between signal and noise on those timescales.

The high and low frequency aspects of these computed accelerations correspond to different types of motion. In figure 21 we show a histogram of the direction of the horizontal acceleration vector relative to the head and thorax. At low values of the smoothing, higher frequency acceleration components that are either aligned or anti-aligned with the body axis are present. Anti-alignment corresponds to backwards acceleration. There is an error signal in the position data that occurs on a single wingbeat timescale because the wing removal algorithm is wingbeat phase dependent, so it is not possible to determine whether this acceleration is solely a measurement artifact. However, there is potentially a genuine signal on this timescale, as the forward/backward motion of the wings drives a small forward/backward oscillation through conservation of momentum. Determining whether such oscillation is present would require higher fidelity measurements. To examine the correspondence between acceleration and body angle, we are interested in measurements over tens of milliseconds, not over single wingbeats, so figure 21(c) is most relevant. The longer timescale components of the acceleration, which become visible at large values of λ, are uniformly distributed, and are without a preferential direction. The lack of preferential acceleration direction indicates that particular values of the forward acceleration are not associated with any particular sideways acceleration. Rather, a given forward acceleration is compatible with a range of sideways

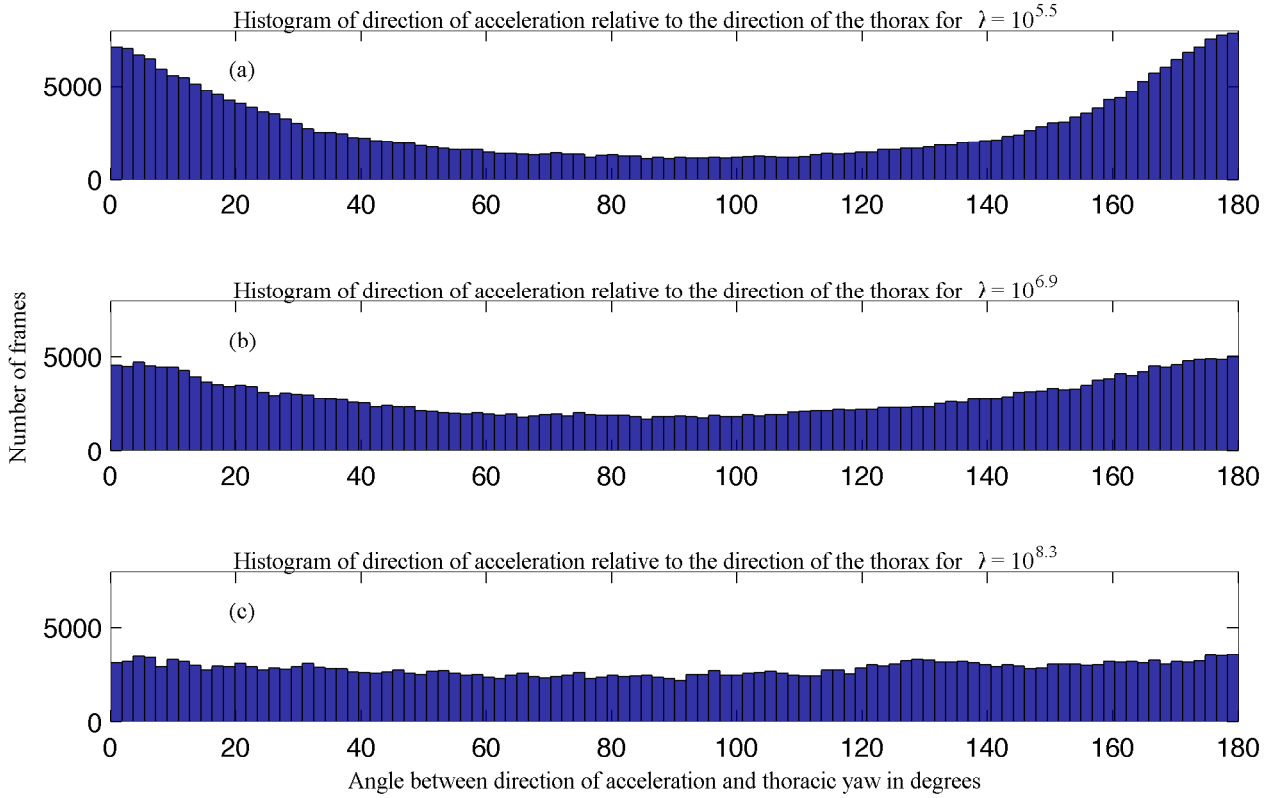

Figure 21: The absolute value of the direction of the acceleration relative to the direction of the thorax and head is shown for three different values of smoothing parameter λ in the histograms above. Each histogram includes 282097 frames of data, because the angular relationship during each frame of each of 231 separate movies is shown. At lower values of λ there is frequently substantial forward acceleration, corresponding to the peak near 0 degrees in (a). There is similarly frequent backwards acceleration, corresponding to the peak near 180 degrees. These forward/backward motions disappear at larger λ. By $\lambda = 10^{8.3}$, corresponding to components of the acceleration with frequency below approximately 60 Hertz being undamped, the acceleration is nearly uniformly distributed, with no preferential direction of acceleration. In (a) and (b) it is not possible to differentiate between the insect's motion and the contribution to acceleration due to measurement noise. Higher resolution images would make it possible to determine whether the strong forward/backward acceleration we see in (a) and (b) is a feature of the insect's flight or is an artifact of systematic measurement errors.

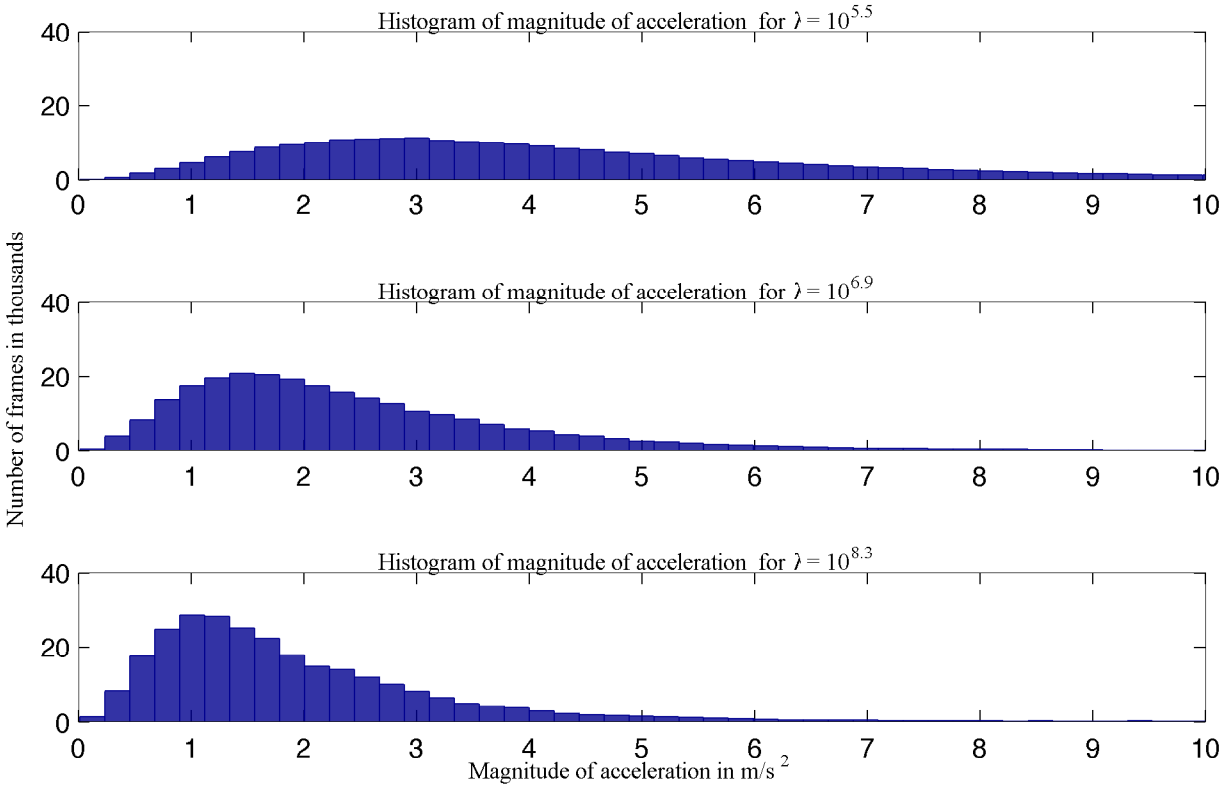

Figure 22: The magnitude of the acceleration in the horizontal plane during each frame analyzed is shown in the histograms above for three different values of smoothing parameter λ. At lower values of smoothing the magnitude of the acceleration is larger and has higher variance than at higher values of smoothing, meaning that short time scale oscillations in acceleration are also of high magnitude. These high magnitude, short timescale, contributions may be a measurement artifact.

acceleration values, and vice versa.

The distribution of magnitudes for the horizontal component of the acceleration is shown in figure 22. In figure 19, the $\lambda = 10^{5.5}$ acceleration line exhibited intermittent high amplitudes while the $\lambda = 10^{9}$ line did not, so the $\lambda = 10^{5.5}$ distribution has a mean of 5.8 m/s^2 and the the $\lambda = 10^{9}$ distribution has a mean of 2.0 m/s^2. We decompose the acceleration into its forward component, which is aligned with the body yaw direction, and its sideways component, which is perpendicular to the body yaw axis. The distributions of forward acceleration and of sideways acceleration are shown in figure 23. The distribution of sideways acceleration is less sensitive to smoothing than that of forward acceleration. The mean of

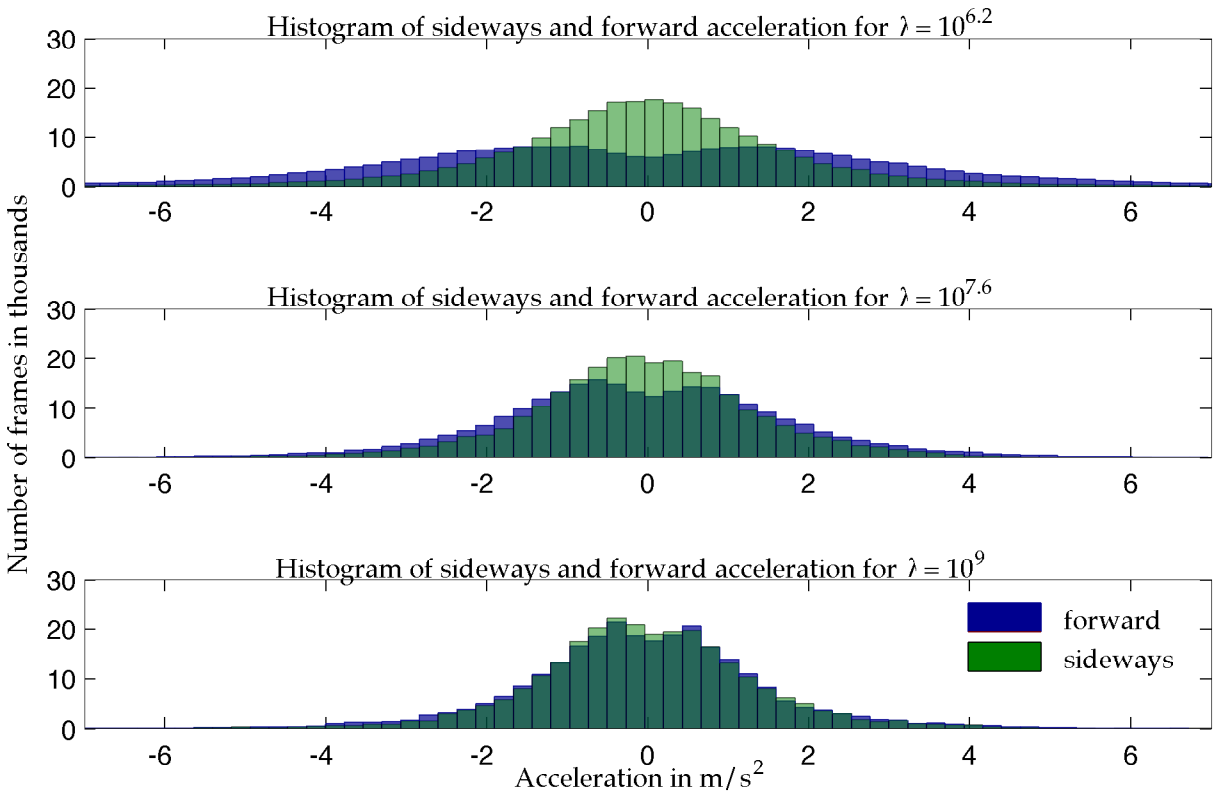

Figure 23: Histograms of the forward and sideways acceleration components are shown for three different values of the smoothing parameter λ. The distribution of forward and backward acceleration is shown in dark blue, while the distribution of sideways acceleration is shown in light green. When the two distributions overlap there is a darker region. The distribution of sideways acceleration changes slightly with λ while the distribution of forward acceleration has mean amplitude approach zero much more rapidly, while remaining bimodal. At all smoothings, forward acceleration is accompanied by substantial backward acceleration.

positive sideways amplitudes ranges from 2.3 m/s^2 when $\lambda = 10^{5.5}$ to 1.3 m/s^2 when $\lambda = 10^9$. The distribution of sideways acceleration is peaked around zero, while the distribution of forward acceleration is bimodal, and is more sensitive to the smoothing parameter. The mean amplitude of positive forward acceleration shifts from 4.7 m/s^2 to 1.3 m/s^2 as λ changes from $10^{5.5}$ to 10^9. We observe forward deceleration as frequently as we observe acceleration. At the same time, the insects exhibit positive forward velocities much more frequently than they exhibit negative forward velocities (Chapter 2). This is likely because the insects enter the field of view with a forward component to their motion.

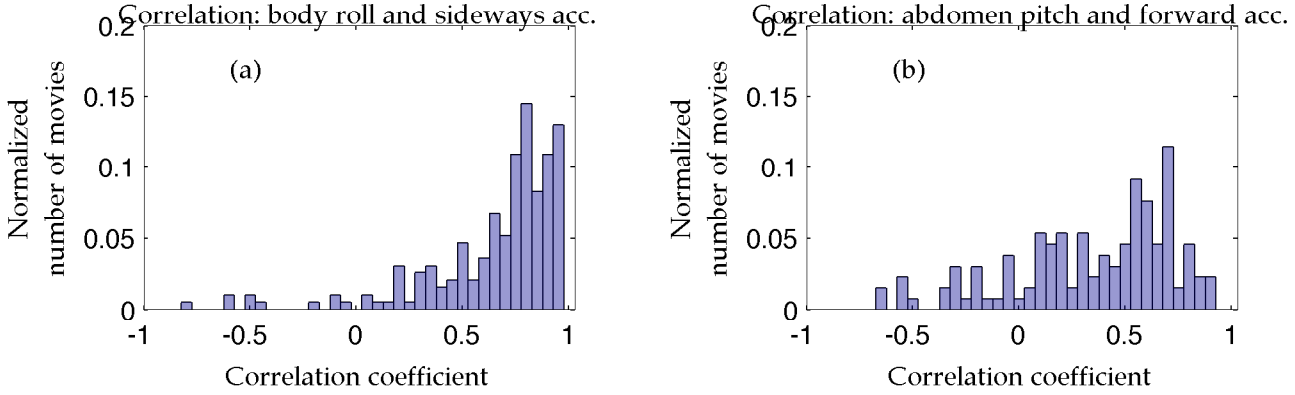

Figure 24: In (a), the cross correlation between sideways acceleration and body roll angle is computed for 188 flights. The results are displayed using a normalized histogram. Correlations of greater that 0.5 occur in 79 percent of movies in the sideways case. In (b), we compute the cross correlation between forward acceleration and abdomen pitch angle in 131 flights. Correlations of greater that 0.5 occur in only 43 percent of movies in the forward case.

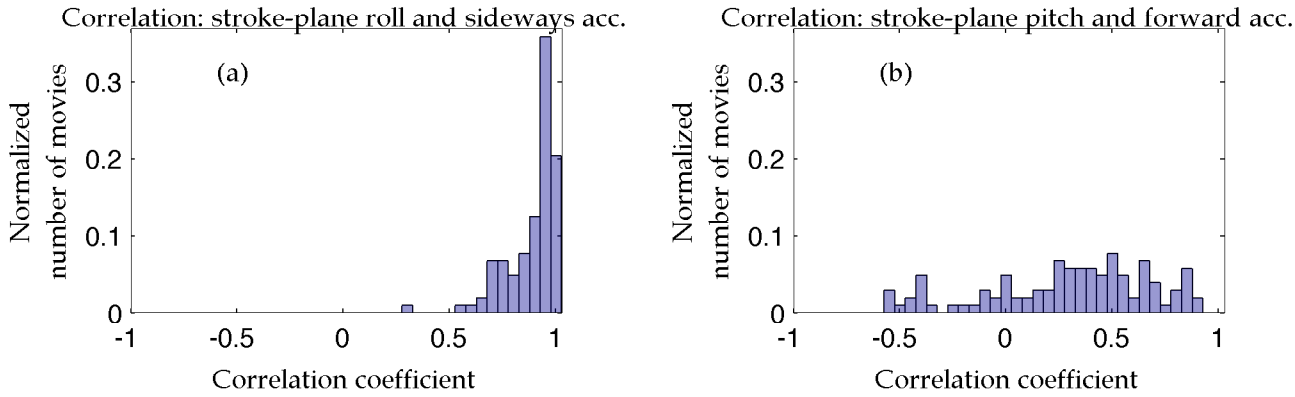

Figure 25: In (a), the cross correlation between sideways acceleration and stroke plane roll angle is computed for 103 flights. The results are displayed using a normalized histogram. Correlations of greater than 0.5 occur in all but one flight. Correlations of greater than 0.8 occur in 80 percent of flights. In (b), we compute the cross correlation between the forward acceleration and the stroke plane pitch angle for 103 flights. The correlation is greater than 0.5 in 33 percent of flights.

Using the longer timescale acceleration calculations, which correspond to $\lambda = 10^9$, we examine the cross correlation over the duration of each flight between abdomen pitch angle, θ, and forward acceleration, for 131 flights. The forward direction is defined using the body yaw angle. A flight is included in the analysis if the variation about the trend line of the pitch angle is less than 1.7 degrees for more than 95 percent of the frames in the flight. This excludes flights where the pitch algorithm has failed. Cross correlation is shift and scale invariant, so we do not need to compute the offset between the abdomen pitch and the stroke angle pitch. We use θ instead of $\tan\theta$ for the comparison because the offset angle between the abdomen pitch and the thoracic pitch varies between insects, and cross correlation is insensitive to this shift. Errors due to the small angle approximation, $\tan\theta \approx \theta$, are less than 4 percent for values of θ less than 20 degrees. Using this approximation, the simplest model of thrust generation via tilt in the absense of drag, reduces to $F_x \approx mg\theta$. The distribution of cross correlations between F_x/m and θ are shown in figure 24(b). The correlation does not improve at other values of smoothing parameter λ. It is almost always weakly positive, and is greater than 0.7 for only 15 percent of flights. The mean cross correlation observed is 0.34. We also compute the cross correlation between the stroke plane pitch angle and forward acceleration for 103 flights, where the forward direction is defined using the stroke plane yaw angle. The distribution of these correlations is shown in 25(b). These are slightly less correlated than the abdomen pitch and the acceleration, with a mean of 0.30 and the correlation greater than 0.7 for 13 percent of flights. These cross correlation values suggest that in the majority of flights there is not a strong association between the observed forward acceleration and the body or stroke plane pitch angle.

For sideways acceleration, with the sideways direction defined using the body yaw angle, we examine the cross correlation over the duration of each flight between F_y/m and $\frac{z_A}{x_A}\sin\psi$, the thorax/abdomen difference angle. A flight is again included if the variation about the trend line is less than 1.7 degrees for more than 95 percent of frames. There are 188 flights included in the correlation analysis. The distribution of cross correlations are shown in figure

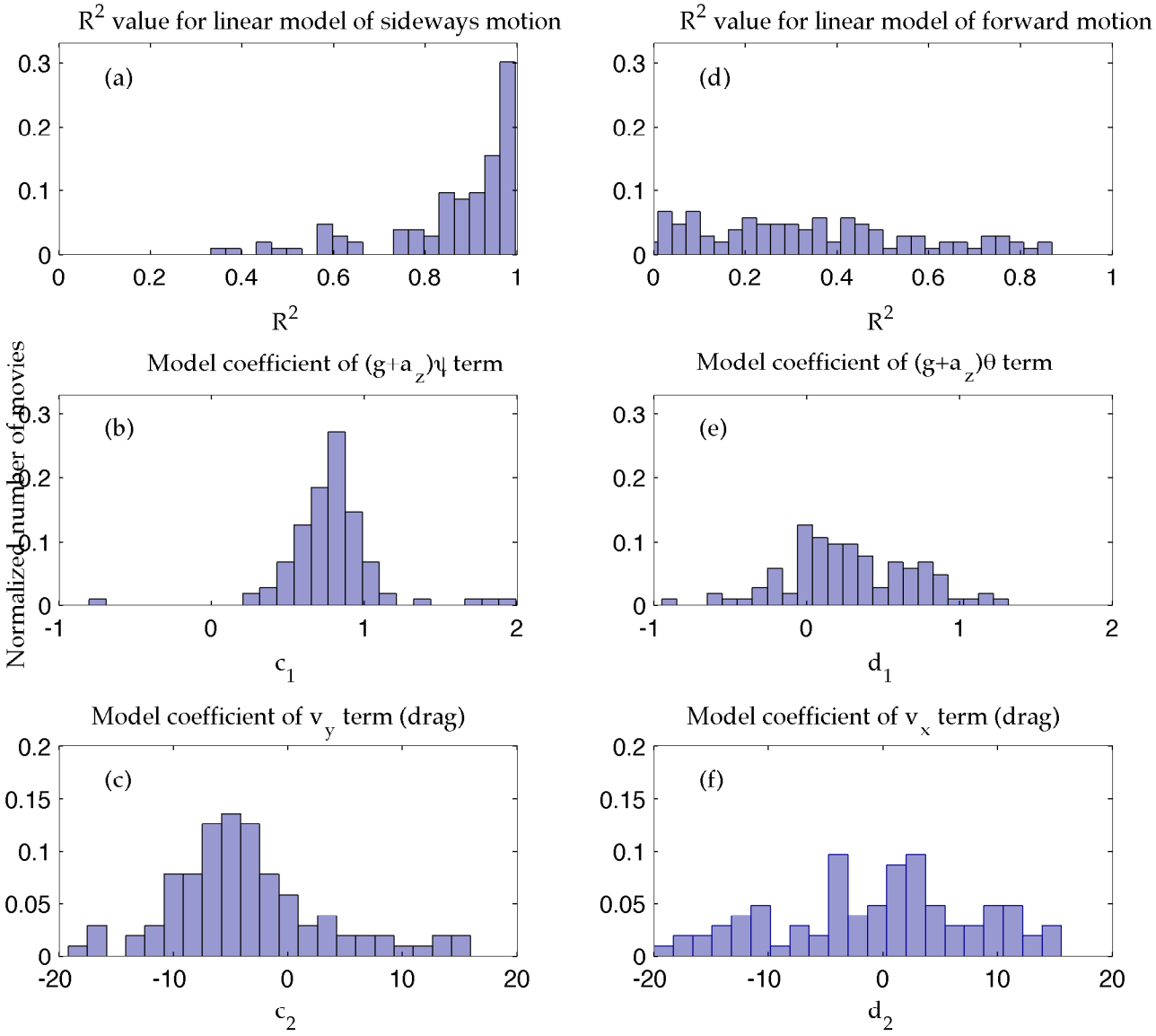

Figure 26: We use the linear model $a_y = c_1(g + a_z)\psi + c_2 v_y + c_3(g + a_z)$ to fit the measured sideways acceleration time series data in each of 103 different movies. The c_1 term is the thrust generation term for a tilt-based thrust model. The c_2 term is a drag term, proportional to the sideways velocity of the insect, and the c_3 term is a correction term in case of systematic errors in the roll value. The R^2 for this model is shown for each flight in (a). It is greater than 0.5 in over 95 percent of movies. The distribution of values of c_1 across all movies is shown in (b) and has a mean of 0.82 ± 0.45. The distribution of values of c_2 across all movies is shown in (c). Its mean is -4.4 ± 13.3. The c_3 term has mean 0.003, and is near zero in most flights. For the measured forward acceleration we use the model $a_x = d_1(g + a_z)\theta + d_2 v_x + d_3(g + a_z)$. The d_1 term is again a thrust the thrust generating term given a tilt-based model, the d_2 term is a drag term, and the d_3 term corrects for the offset between the abdomen pitch and the stroke plane pitch. The R^2 for this model, which is almost uniformly distributed, is shown in (d). Values of d_1 have a mean of 0.19 and are shown in (e). Values of d_2 are shown in (f).

24(a). The cross correlation is greater than 0.7 for 62 percent of flights, and the mean value observed is 0.65. We also compare the measured sideways acceleration, with the sideways direction defined using the stroke plane yaw angle, to the stroke plane based roll angle for each flight. These time series are more strongly correlated, as shown in figure 25(a). The cross correlation is greater than 0.7 for 91 percent of flights using a wing based measurement of the roll angle, rather than a body based measurement. Based on the stronger relationship between angle and measured motion in figure 25(a), the stroke plane coordinate frame is more useful for gaining insight into the flight forces.

For each flight analyzed above, we fit a linear model corresponding to the helicopter thrust model to the data. For sideways motion we use the linear model $a_y = c_1(g + a_z)\psi + c_2 v_y + c_3(g + a_z)$, where a_y is the measured sideways acceleration in the stroke plane frame, a_z is the measured vertical acceleration, ψ is the stroke plane roll angle, and v_y is the measured sideways velocity. For the helicopter thrust mode, we expect $c_1 = 1$ where θ is the pitch of the abdomen, $c_2 < 0$ because it is a drag term, and $c_3 \approx 0$. The presence of c_3 is for statistical analysis purposes so it is straightforward to find a p value for the linear model. In figure 26a we show the distribution of R^2 values for this model when it is fit to timeseries from 103 different movies.

The R^2 value is greater than 0.5 for 95 percent of movies and is greater than 0.75 for 49 percent of movies. The distribution of c_1 is shown in figure 26(b). The mean of c_1 is 0.82 with standard deviation 0.45. This is the term that corresponds to thrust generation. The distribution of c_2, the coefficient of the drag term, is shown in figure 26(c). The mean of c_2 is -4.4 1/s with a standard deviation of 13.8. This is very similar to the drag value of 4.03 1/s found for fruitflies in forward flight by Medici ([50]). The distribution of c_3, the roll shift term, is not shown. It has a mean of 0.003 and a standard deviation of 0.12, so remains small in almost all cases. The high R^2 values for the fit of the linear model, coupled with physically plausible values for the thrust coefficients and the drag coefficients in many flights, indicate that the model offers a useful description of sideways acceleration.

For forward motion we use the linear model $a_x = d_1(g + a_z)\theta + d_2 v_x + d_3(g + a_z)$, where a_x is the measured forward acceleration, θ is the stroke plane pitch, and v_x is the measured sideways velocity. In figure 26c we show the distribution of R^2 values for this model fit to timeseries data from 103 movies. The R^2 value is greater than 0.5 for 23 percent of movies and is greater than 0.75 for 8 percent of movies. The distribution of d_1 is shown in figure 26(e). The mean of d_1 is 0.35 with standard deviation 23. This is the term that corresponds to thrust generation. The distribution of d_2, the coefficient of the drag term, is shown in figure 26(f). The mean of d_2 is -0.023 with a standard deviation of 0.65. The distribution of d_3, the error term, is not shown. It has a mean of -0.23 and a standard deviation of 2.0. The poor R^2 values for this model, coupled with the physically implausible parameter values it produces, indicate that it has little explanatory benefit. This is in marked contrast to fruitflies, where a nearly identical linear model relating body pitch and forward acceleration has an R^2 value of 0.997 ([50]).

3.3.1 Stroke plane reference frame

The differences between figures 24 and 25 indicate that the body based reference frame and stroke plane based reference frame are not identical. The stroke plane yaw, which is the average of the two wing stroke angles, often lags behind the body yaw by a few milliseconds. This is visible in figure 27. Thoracic turns (in blue) precede stroke plane turns (in green) in each of the four flights shown. This time lag may be a result of large wing drag relative to body drag during yaw turning, a phenomonon which is well explored in the yaw turns of fruitflies ([38], [10]). Based on the correlation and modeling results presented above, the stroke plane coordinate frame is a more natural frame than the body frame for predicting sideways thrust. However, the presence of rotational offset between the stroke plane frame and the body frame during yaw turns complicates the analysis of turning maneuvers, since torques generated along a single axis in the stroke plane frame correspond to torques along a combination of axes in the body plane.

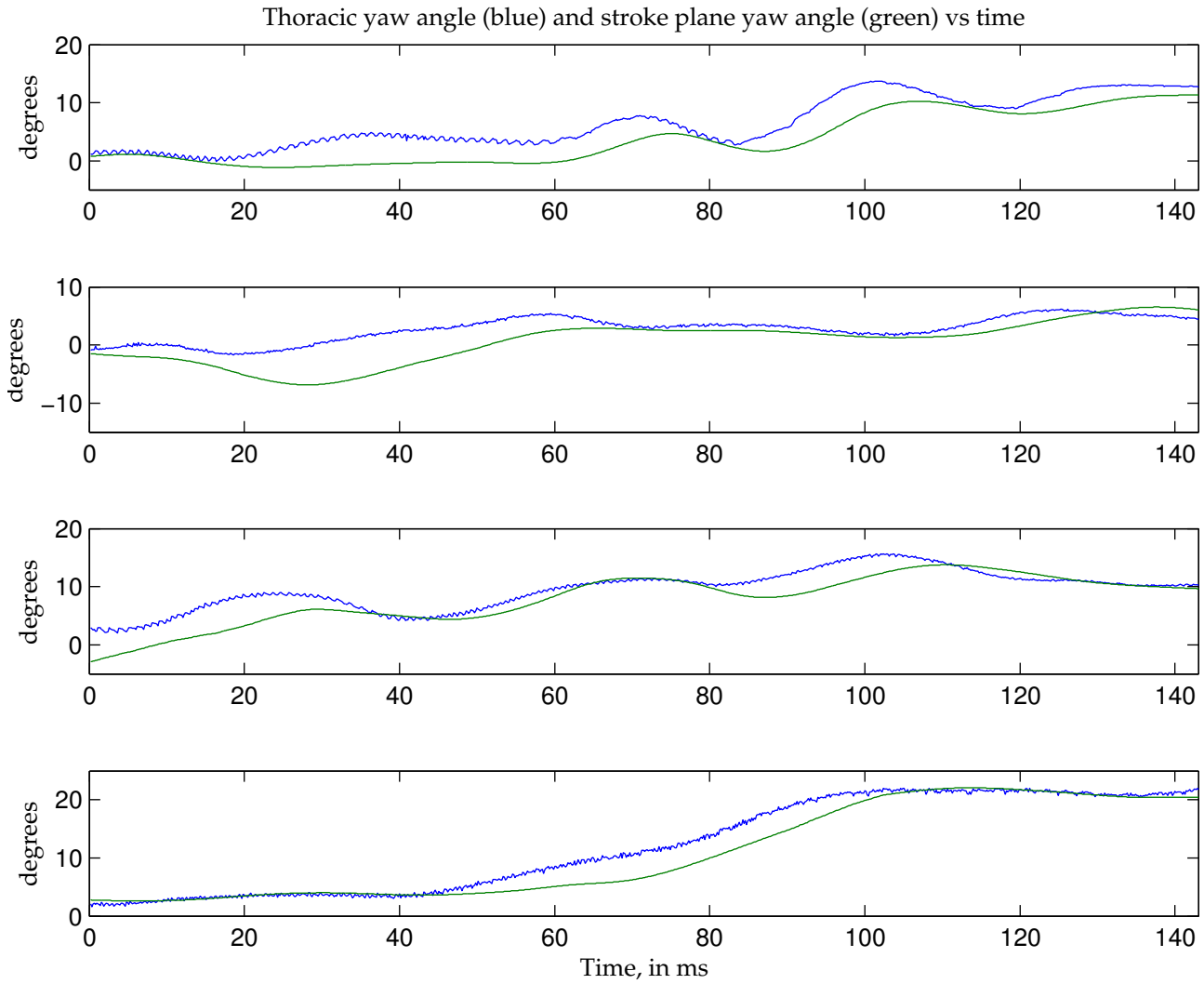

Figure 27: The thoracic yaw angle of the body (blue) and the yaw angle of the stroke plane (green), which is equivalent to the mean of the wing stroke angles at each instant, are plotted against time for 140 ms segments of four different flights. Changes in yaw angle occur first in the body. The center angle of the wings adjust with a time lag of a few milliseconds.

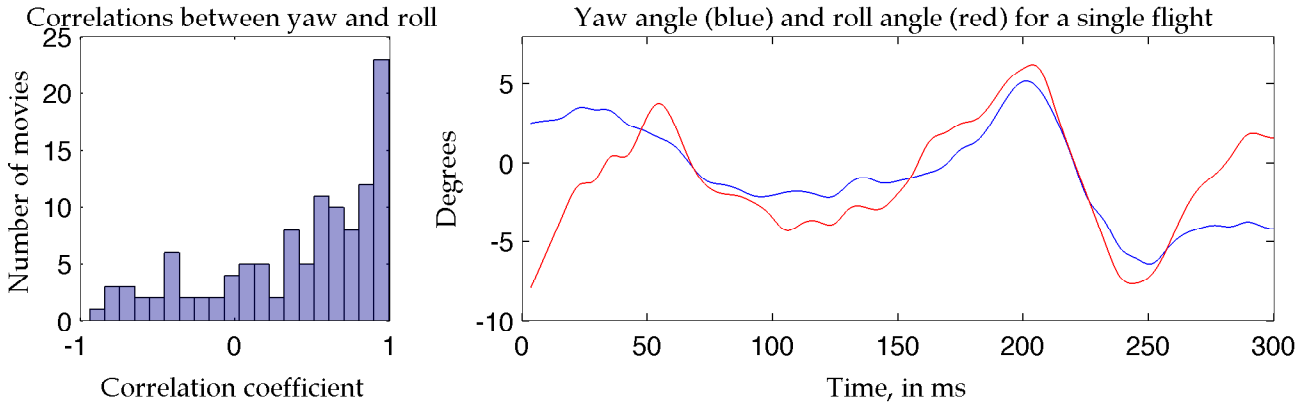

Figure 28: On the left, the distribution of correlation coefficients between the roll angle and the yaw angle in the stroke plane reference frame is shown for 116 flights. Change in yaw often occurs simultaneously with change in roll, leading to correlations near 1. On the right, the yaw angle (blue) and roll angle (red) are shown for a flight where the correlation is 0.76. The variation in roll is slightly larger than the variation in yaw, which is typical for the measured mosquitoes.

We compute the principal axes of the mosquito body for an inertial tensor constructed using ellipsoids to model the thorax, abdomen, and head. The principal axes are not quite aligned with the axes of the body frame. We find the principal axis nearest the body axis is tilted -15 degrees from the axis, an upward tilt. The moment of inertia about this axis is approximately 0.8×10^{-13} N m s^2, while the moment about the pitch axis is 4.7×10^{-13} kg m^2 and that about the third axis, which is inclined 15 degrees away from the body yaw axis, is 4.1×10^{-13} M n s^2. The moment of inertia about the yaw axis is about 20 percent smaller than that computed for similar weight fruitflies in [29]. In mosquitoes, the midgut and hindgut are located in the abdomen, so these moments may change as the insect's weight distribution changes with feeding. In particular, the center of mass moves backwards and downwards and the inclination of the principal axis away from the body axis is reduced when the abdomen is heavier.

When the stroke plane is not pitched to align with the principal axis, then force asymmetries between the two wings may drive motion about both the roll and yaw axes. The mean stroke plane pitch measured over approximately 10000 wingbeats was 8.6 ± 9.5, so

the stroke plane is slightly tilted in a direction that may exacerbate any yaw-roll coupling. Such a coupling has been suggested previously ([67]). We observe frequent high correlations between the roll angle and the yaw angle, consistent with the presence of coupling. These correlations are shown for 116 different flights in figure 28(a). In figure 28(b) is a timecourse of roll and of yaw for a single flight. While variations in roll and yaw consistently occur together, their angular velocities are not correlated. Correlations between the pitch and roll angles or between the pitch and yaw angles also vary substantially from flight to flight.

Within single flights, roll shows substantial variation, with the angular velocity of the insect about the stroke plane roll axis larger than that about the stroke plane yaw axis during most wingbeats. At the same time, the stroke plane roll angle remains within 10 degrees of horizontal in over 85 percent of wingbeats, and within 15 degrees of horizontal in 95 percent of wingbeats. The narrow window of observed roll values, along with its large variations and dynamic importance, may indicate that roll is tightly controlled in this insect.

3.4 Discussion

For the mosquito data we analyzed, given angular measurements in the stroke plane frame, measured sideways accelerations closely corresponded to those predicted by a roll-based model of thrust generation. This relationship has been observed qualitatively in many insects ([77], [87]) and is supported by quantitative evidence in mosquitoes. In contrast, in both the body frame and the stroke plane frame, the pitch angle did not show a correspondence with the forward acceleration. While a change in pitch angle must change the direction of the lift force, this force is not the dominant driver of forward acceleration in mosquitoes. Instead, forward thrust may be generated directly by wing based mechanisms. This lack of correspondence aligns with measurements in droneflies ([78]) and is in contrast to fruitflies, where a quantitative correspondence has been established ([50]), even as other mechanisms of forward thrust generation are known to exist ([58]).

Mechanisms such as pitch asymmetries during the two half strokes ([58]) or changes in the speed of the wing flip generate large forces ([1]), and such mechanicms could also potentially be used to generate forward thrust. By using deflection of the lift vector to generate sideways acceleration, and utilizing non-lift based mechanisms as important contributors to the forward acceleration, forward and sideways thrust become decoupled controls. This decoupling means that the insect may be able to increase its total acceleration beyond what is available from lift alone, by simultaneously using separate mechanisms to generate forward and sideways thrust.

The centrality of roll to sideways thrust generation, and the importance of sideways motion to control of direction during mosquito flight (Chapter 2) implies that the generation and control of changes in the roll angle are fundamental to the control of mosquito motion. Despite the low moment of inertia on the principal axis of the insect most closely aligned with the roll axis, and the rapid rates at which the insect rotates about the roll axis, the roll angle remains within -15 to 15 degrees in almost all flights. With roll and yaw closely correlated in these insects it is potentially possible that active control of the roll angle drives some of the variation we observe in the yaw angle. From an inertial perspective, the small torques needed to generate changes in the roll angle would not generate substantial changes in yaw. However, there may be substantial damping forces associated with wing motion during roll ([37]). There are known to be large damping forces associated with yaw motion ([38]).

Since mosquitoes have the ability to generate thrust in an arbitrary direction, and their pitch angle does not correspond to their forward acceleration, the dynamic importance of their yaw and pitch angles may be reduced. The degree to which tight control of yaw and pitch angles is necessary during mosquito flight is not clear.

Chapter 4

Mosquito wing motion

4.1 Introduction

In Dipterans, the flapping motion of the wings is central to their force and torque production during flight. Wing motion has been studied extensively during tethered flight ([54], [34], [55], [88], [18], [17], [38], [39], [2]), and also during free flight ([29], [79], [24], [30], [26], [49], [5], [78], [1]). Identifying how changes in wing motion generate maneuvers has been a central question driving the study of wing kinematics. Many different changes in stroke motion have been identified and found to correspond to the forces and torques that create changes in body motion. In blowflies, for example, wingbeat frequency strongly correlates with lift ([54]), and in fruitflies asymmetries in stroke amplitude between the two wings are common during yaw turns ([29], [38]). Asymmetries in wing pitch between the two wings have been linked to turning maneuvers ([5]), and pitch asymmetries between the upstroke and downstroke account for variations in forward thrust needed to overcome drag at different forward velocities ([58]). In some cases, patterns of wing motion have been linked to measurements of muscular activity, with the identification of distinct modes of motion activated by specific flight muscles in blowflies ([2], [74], [55]).

Mosquito wing motions differ in basic aspects from those of many well studied Dipterans.

Many measured Dipterans use stroke amplitudes of well over 100 degrees to propel their flight ([24]), although the hoverfly *Episyrphus balteatus* is an exception. It displays a stroke amplitude of $66-95$ degrees ([24]). The hoverflies *Eristalis tenax*, referred to as a dronefly by Ellington and in [49], also sometimes display lower stroke amplitudes. Walker et al. found its stroke amplitude to vary from 67 to 130 degrees in measurements of five individuals ([78]). For *Aedes aegypti* mosquitoes, we find typical stroke amplitudes to be much smaller even than those of hoverflies, with stroke amplitude ranging from 34 to 54 degrees across thousands of measured wingbeats.

In male *Aedes aegypti*, this remarkably small stroke amplitude is accomponanied by a high wingbeat frequency. The free flight wingbeat frequency of male *Aedes aegypti* has been previously measured as 750 ± 66 Hertz in [51] and as 715 Hertz by [7]. These studies involved audio recording insects and analyzing the resulting signal. In work by Brogdon, higher harmonics of the flight tone were also identified, and for a female *Aedes aegypti*, there was almost equal power in the first two harmonics, with less than half as much power in the third. In tethered work described in [9], the male flight frequency is reduced to 637 ± 15 Hertz, and harmonics of the wing frequency are found to be used during mating. In the motion capture data collected here, tethering to the thorax distorted the wing motion of males. In fruitflies, tethering is also found to distort the wing motion ([30]). We measure the wingbeat frequency for free flying male *Aedes aegypti*, finding a frequency of approximately 800 Hertz. The combination of a small stroke amplitude and a high wingbeat frequency means that these mosquitoes have an associated Reynolds number only slightly lower than that of fruitflies.

We observe many asymmetries in wing motion between the two wings and between the downstroke and upstroke of the wing. The wing flip is frequency asymmetric. After the wing passes through vertical, its angle will fall to nearly horizontal at one end of the stroke. At the other end of the stroke, it will drop to approximately 45 degrees. When this asymmetry in the amount of rotation after the wing flip is present, it occurs in both wings. A period

of wing translation with low rotation is sometimes present in one wing, the other, or both, and is often absent, so that the wing rotates continuously during the stroke. The timing of the wing flip relative to the stroke turnaround also varies, and can be different for the two wings. These variations lead to asymmetries in the pitch angle between the downstroke and upstroke or between the two wings. Such asymmetries generate torque ([5]) and thrust ([58]). In addition, forces can be elevated depending on the speed of the wing flip or its timing relative to turnaround ([1], [20], [63]).

4.2 Methods

To describe the orientation of the wing in each frame we identify two vectors. The span vector is a vector that aligns with the leading edge of the wing and points away from the body. The chord vector is perpendicular to the span vector, lying in the plane of the wing. The chord vector is chosen so as to originate at the leading edge and point toward the trailing edge of the wing. The wing vein of the mosquito lies along the leading edge, and is directly attached to the wing hinge, so it is the position and orientation of the leading edge that are directly influenced by the insect.

For a given motion capture sequence, the span vectors and chord vectors of the two wings are identified in each frame of the movie. Wing kinematics are most easily compared in a stroke plane based coordinate system [24]. We generate such a wing based reference frame from the span vectors from sequential frames, using a method described below. After we identify the stroke plane based coordinate system, we transform the measured span and chord vectors into this continuously changing coordinate system for comparisions of wing motion over time and across flights.

To find the span and chord vectors, we identify pixels in the overhead and side views that correspond to the wing leading edge. We construct the span vector so that it aligns with these pixels. In addition, using the projection of the wing into the xy-plane, we generate

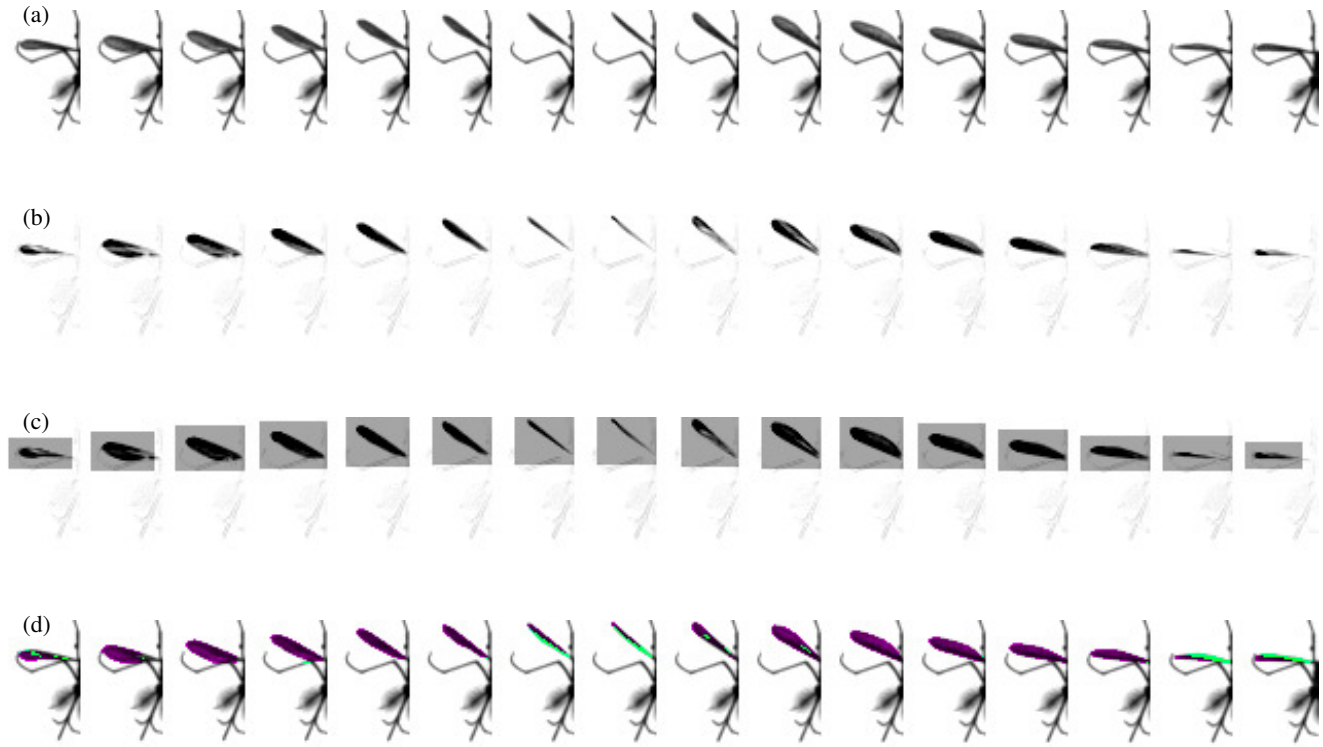

Figure 29: Wing motion of the right wing of the insect over a complete wingbeat. The wing is moving backwards for the first half of the stroke and forwards for the second half. We use a simple tracker to identify the pixels in this wing in each frame. In (a) we shown the unprocessed image over 16 frames, which make up a single wingbeat. In (b), the wings have been isolated using image subtraction. The pixels that are above a fixed threshold in (b) are colored magenta in (d). The gray boxes in (c) show the location of the automatically generated mask that is used to isolate the wing from other features. In (d), all pixels that are identified as part of the wing are colored green or magenta. Green pixels were identifed by augmenting the difference image by restoring pixels that were part of the wing in the prior frame to their initial intensity before applying a threshold for identifying wing pixels.

constraints for calculating the chord vector.

To find leading edge pixels, we start by identifying all wing pixels in each frame of the overhead view. The first principal component axis through the pixel coordinates yields an initial estimate of the wing orientation. The minor chord length associated with fitting an ellipse to the pixels yields a wing width estimate. By identifying changes in the wing orientation and wing width, we find the direction of the wing's motion. Each frame is then classified as part of the forward or backward stroke. For this classification, at the ends of the wing stroke, when the wing orientation remains nearly fixed as the wing rotates, we assume that the wing has changed direction once the wing width as seen from overhead begins to increase.

Using this direction information, one of the edges of the wing is considered the leading edge. We identify the pixels associated with that edge of the wing in the overhead view. In the side views, the leading edge lies along the top edge of the wing. In each frame, we shift the image downward by one pixel and subtract this shifted image from the original image. This isolates the upper edges of the insect's body, including the leading edges of any visible wings.

Identifying wing pixels

The first step in this process was to identify all pixels in each wing for each frame of the overhead view. We use a simple tracker for this. This tracker works by applying a mask to the next frame based on the location of an object of interest in the current frame. Often we draw a rectangle around the location of the object in the current frame and use this rectangle as a mask in the next frame.

For the overhead view, once preliminary wing motion information has been measured, we use a linear model to identify where the mask should be drawn. For motion capture sequences imaged at 13029 frames per second, the mask is centered at an angle of $(0.84 - 0.93(\phi_{n-1} - \bar{\phi}) + 0.39(\phi_n - \bar{\phi})) + \phi_n$ where $\phi_{n-1} - \bar{\phi}$ is the angle of the wing relative to the

average position of both wings in the previous frame, and $\phi_n - \bar{\phi}$ is that relative wing angle in the current frame. These coefficients were determined by fitting 70 flights of preliminary angle data. The linear model generates an angle within 5 degrees of the predicted stroke angle. For the sequences imaged at 6309 frames per second, the mask is centered at $(0.22 - 0.95(\phi_{n-1} - \bar{\phi}) + 0.75(\phi_n - \bar{\phi})) + \phi_n$. We then restrict our search for the new location of the object to the pixels within the masked region.

Raw images of the right wing of a flying insect are shown over a full wingbeat in figure 29a. Difference images created by subtracting frames 1/8 of a wingbeat apart are shown in figure 29b. In the first frame of a sequence we identify the two largest blobs visible in the difference image via the Matlab *regionprops* command. These two blobs correspond to the two wings. Tracking the blobs one at a time, we use thresholding to identify pixels that are within the wing. These pixels are shown in magenta in figure 29d. When we are not using prediction, we create a mask that isolates a region slightly larger than the area where we found the wing pixels. When we are, we locate the mask using the linear model given above. The masks are shown as gray boxes in figure 29c. Note that when the number of pixels identified as part of the wing falls below some threshold, we do not update the mask. Thus the mask does not change from frame to frame when we are near the end of the wingbeat and the wing is rotating more than it is translating.

This technique identifies the majority of the wing pixels, particularly at times when the wing is translating rapidly, as it does near the center of the stroke. If a particular pixel is part of the wing during a sequence of multiple frames, as happens near the wing turn-around points, differencing methods will not identify that pixel. We thus must augment the pixels identified via wing differencing by adjusting the difference image. For each pixel that was part of the wing in either of the previous two frames, we assign that point in the difference image the intensity associated with the pixel in the current frame. This restores high intensity values at points in the wing that are improperly eliminated by taking differences. We then use thresholding to identify the pixels in the wing in the augmented difference image. In this

way we identify additional wing pixels, shown in green in figure 29d. These green pixels are pixels that are part of the wing but which were not identified by a combination of simple differencing and then thresholding.

Find the leading edge of the wings

Once the wing pixels are identified, the next step is to isolate the pixels along the leading edge. The leading edge corresponds to the location of the wing vein. However, the location of the wing vein is not straightforward to determine, even by eye, given the resolution of our images. Instead, we use information about the wing's motion to find the leading edge. When the wing, as seen from overhead, is in the center of the stroke, there are large changes in the angular position of the wing between frames. In its projection into the horizontal plane, the wing subtends approximately 45 degrees, or 0.8 radians, over the course of a half stroke. With frames taken 1/16 of a wingbeat apart, the distribution of change in angle of the wing principal axis between frames is shown in figure 30a. When this change is sufficiently large we use it to identify the direction of wing motion. Near the wing turning points, the leading edge becomes nearly fixed, as the wing width increases. Using an average orientation of all wing pixels in place of the orientation of the leading edge leads to an overestimate of the stroke angle, because the increase in wing width during turning shifts the average orientation outward. The change in average orientation due to wing rotation is approximately $\tan^{-1} \frac{\Delta width/2}{wing\ length}$. Near the end of the stroke, most change in average orientation corresponds to wing rotation rather than to wing translation. A histogram of the change in the chord width of the xy projection of the wing is shown in figure 30b.

A change in wing width of 0.25 mm from one frame to the next corresponds to an apparent change in stroke angle of 4.5 degrees. This is a change of nearly half the wing chord, so we use 4.5 degrees of change in the principal axis orientation of the wing as a threshold for differentiating true wing translation from apparent wing translation that is

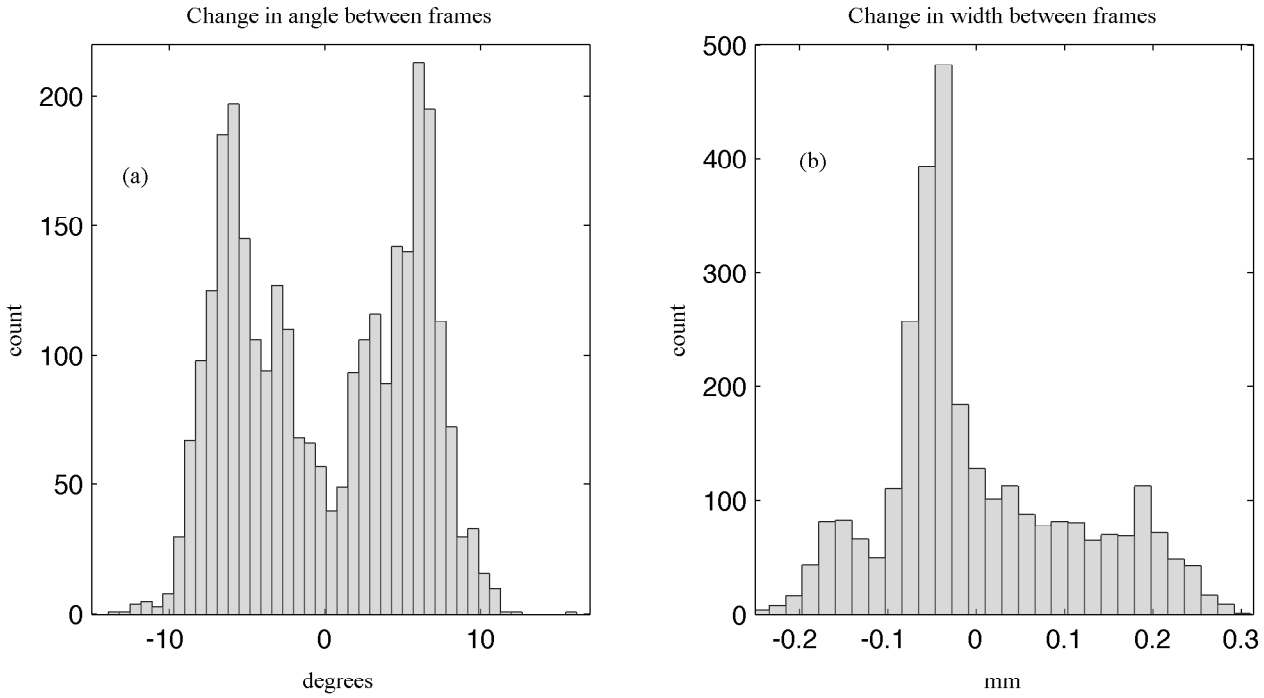

Figure 30: Given the angle of the principal axis of the wing pixels identified in the overhead view, as well as the estimated wing width, we compute the change in angle between consecutive frames. The frames are recorded approximately 1/16 of a wingbeat apart. The change in angle between frames has the distribution shown in (a). Changes are usually on the order of 7 degrees. Near the wing turnaround, they become very small, and at the center of the stroke they can be larger. Changes of more than 4.5 degrees are attributed to wing translation, while smaller changes may be an artifact of wing rotation. In (b) we show the distribution of changes in wing width between frames. The distribution has a longer tail on the positive side because the wing width increases very rapidly when the wing plunges from vertical to nearly horizontal at wing rotation. The peak at -0.04 mm indicates corresponds to small increases in wing pitch angle and in the angle of attack as the wing becomes more vertical.

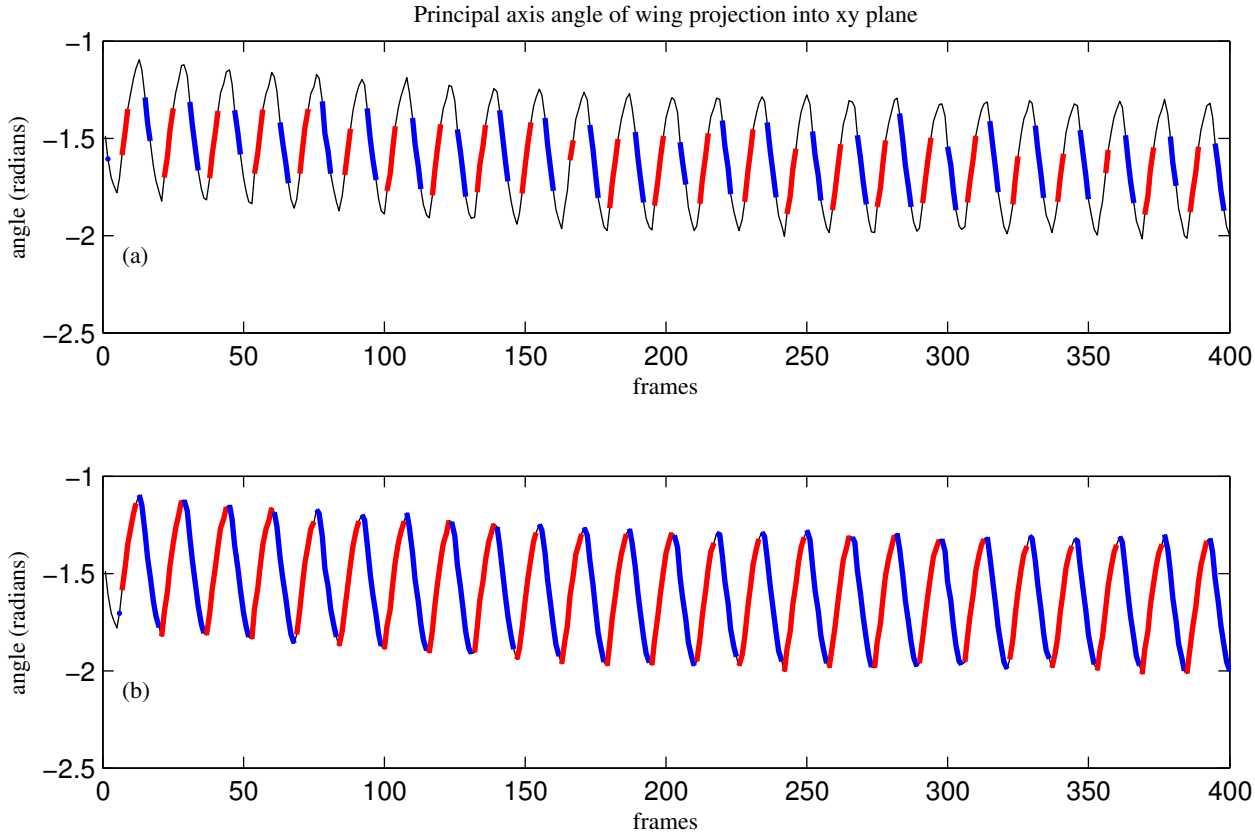

Figure 31: The angle of the principal axis of a wing is plotted against time (black). Using 4.5 degrees of change to identify translational motion in the downstroke or upstroke direction results in the red and blue lines shown in the top graph. In the bottom graph, these classifications have been extended by using the transition from a decreasing wing width to an increasing wing width to identify when the wing flips. This classification is used to identify which side of the wing is the leading edge, not to identify the stroke angle reversal, so the wing width criterion is appropriate.

actually due to wing rotation. When this threshold is met over three consecutive frames, we assign a direction to the wing motion of the middle frame. In figure 31a, the orientation of the principal axis of the projection of the wing into the xy plane is shown by a black line. Successive frames that meet the directional criterion for increasing angle are colored red, while those that meet the criterion for decreasing angle are colored blue. To classify the rest of the frames, we identify frames in which the wing width is increasing but had previously been decreasing. Increasing wing width is associated with the wing flipping from being a flag out to one side of the leading edge to being a flag out on the other side. Thus the edge of the wing that we should associate with the leading edge changes at this time. This does not imply that the leading edge must change its direction of motion at this frame, only that we should change which edge of the wing we classify as the leading edge at this point. In figure 31b, all frames of the sequence are classified using this criterion to identify direction changes. For frames colored red, we will look to the edge of the wing that is rotated clockwise from the orientation to find the leading edge, and for frames colored blue we use the counter-clockwise edge as the leading edge. When misclassifications occur they are at the wing turning point, where the wing is narrow, and the leading and trailing edges are very close together in the overhead view.

Once we have determined which edge of the wing to consider the leading edge, we find the pixels which make up the leading edge. We create a base image that includes the leading edge of the wing and few other pixels. We subtract excess pixels to find just the leading edge. For most frames, using the difference image between the current frame and the previous frame produces an appropriate base image where the leading edge is present. In frames where the visible portion of the wing decreases significantly or when wing translation is low, we retain the whole wing. The portion of the wing retained over the course of a wingbeat is shown in black in figure 32a. It is superimposed over the image of the insect for reference. Next we apply a mask so that we retain only the wing itself. We use the measured orientation of the wing centerline to create a rectangular mask that aligns with the wing. The masks are

Figure 32: To identify the pixels that are part of the leading edge of the wing in the overhead view, we begin with the difference image between the current frame and the previous frame. In frames where there was little translation between the previous frame and the current frame, we retain the entire wing. The retained portions are shown in black in (a). To retain only the wing of interest, we use the measured orientation of the wing centerline to generate a rectangular mask along the wing. These masks are shown in light gray superimposed n the wing image in (b). For the leading edge, we identify the pixels at the very edge of the wing, so we segment the edge pixels from the interior pixels using image erosion. The interior pixels are dark in (c) while the edge pixels are green. In some cases the difference image in (a) contains pixels from both the leading edge and the trailing edge of the wing. We dilate the interior pixels in the direction away from the leading edge so that trailing edge pixels become part of the dilated interior. These dilations are shown as dark pixels in (d). We subtract the dilations in (d) from the initial images in (a) to isolate the leading edge. The leading edge pixels identified using this algorithm are shown in (e).

shown as gray parallelograms on the wing images in figure 32b.

To retain just the pixels at the very edge of the wing, we segment the edge pixels and the interior pixels To do this, we erode the original image using an erosion width of three pixels, thus isolating all interior pixels on the insect. These are shown in figure 32c as dark pixels. The intact insect is in green for contrast. To isolate the pixels on the leading edge, we use our directional and angular information to dilate the wing interior. We dilate the interior in the x direction associated with the trailing edge and also in the y direction associated with the trailing edge. The results of the dilation in y is shown in figure 32d. Given the current orientation of the insect, this dilation is more important for eliminating the trailing edge. We subtract these two dilations from the initial image to isolate the leading edge pixels. When the wing is narrow, so that there are no interior pixels, we retain the entire wing. In all other cases this technique isolates the leading edge. These leading edge pixels correspond to the projection of the wing vein into the xy plane. We find the orientation of this projection by identifying the principal component axis through pixels that are between 0.6 and 1.8 mm from the mean location between the two wings. This allows us to find the relationship between Δx and Δy in the span vector, $\mathbf{v}_s$, where $\mathbf{v}_s = \begin{bmatrix} \Delta x \\ \Delta y \\ \Delta z \end{bmatrix}$.

To find the relationship between Δx or Δy and Δz and thus reconstruct the direction of the spanwise wing vector, we also require information about its change in z with respect to either x or y. This means we must incorporate information from a side view. In the side views, the leading edge of the wing corresponds to the top edge of the wing, so we isolate pixels along the top edges of the wing. A side view of the insect, over 8 successive frames, is shown in figure 33a. To isolate the upward edge pixels, we subtract a downward shifted copy of the current image from the unaltered image. The result of this subtraction is shown in black, superimposed on a gray insect, in figure 33b. This subtraction isolates the upper edge of the abdomen, the wing, some of the legs, and the proboscis. Using these upper edge images as the source images, we then use the same tracking algorithm as we described for

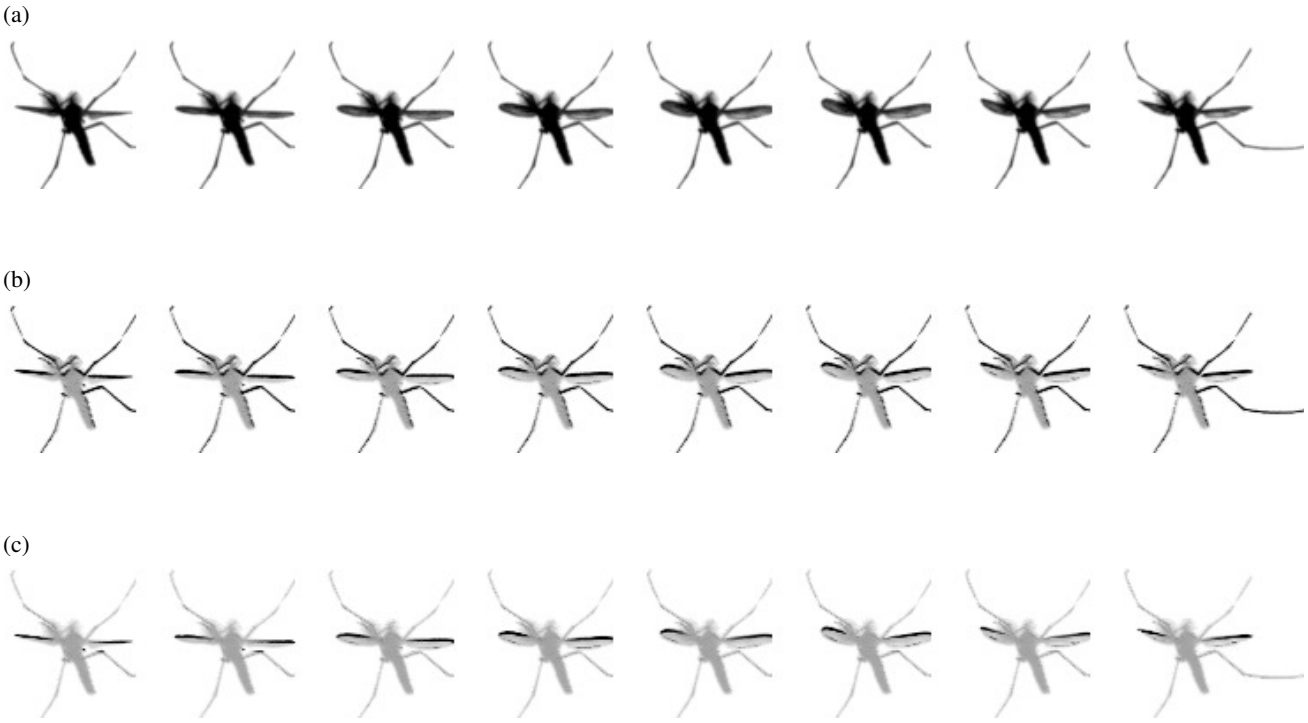

Figure 33: To construct a vector in the direction of the leading edge, we require information from a sideview. For each wing we use the sideview where it is least occluded by the thorax. The leading edge corresponds to the top edge of the wing. Beginning with the images in (a) we create a copy of each image that is shifted downwards by one pixel and subtract this shifted copy from the initial image. The result of this subtraction is shown in (b). This technique isolates the upper edge of the wings as well as some pixels in the legs and along the upper edge of the abdomen. We use these edge images as source images for the tracking tracking algorithm we illustrated in figure 29. This leads to the wing pixel identifications seen in (c).

identifying the wing pixels in the overhead view, including the frame differencing steps. The frame differencing steps lead to the wing edge images that are visible in black in figure 33c. Usually, each wing is only visible in a single side view. In the other side view, the wing will be occluded by the thorax. By identifying the body and wing positions in the overhead view, it is possible to identify the appropriate side view to use for tracking a particular wing. The appropriate side view may change over the course of the flight as the insect rotates in flight. Selecting which view to use is done by hand.

4.2.1 Computing span and chord vectors

Once the leading edge pixels are identified in one of the side views we find the first principal component associated with these pixels. We use this principal component vector to find the relationship between either Δx or Δy and Δz. We then use this information to construct the span vector, $\mathbf{v}_s$. This is a vector in 3-space that is consistent with the leading edge information from the overhead view and the selected side view. To fully specify the orientation of the wing, we also construct a second vector, perpendicular to the span vector. This is the chord vector, $\mathbf{v}_c$. The chord vector is a vector of magnitude c_M, where c_M is the maximum chord length encountered along the length of the wing. The projection of this vector into the xy-plane, $\mathbf{v}_{cxy}$, must be consistent with the measured location of wing pixels in the overhead view. Since the wing is close to ellipsoidal, and we have measured the width of the wing perpendicular to a known orientation, we are able to create a vector $\mathbf{v}_{xy} = \begin{pmatrix} -\sin\theta, \cos\theta \end{pmatrix}$. Here θ is the known wing orientation in the xy-plane. The projection of $\mathbf{v}_{cxy}$ onto $\mathbf{v}_{xy}$ is of length $2b$ where $2b$ is the measured width of the wing perpendicular to θ. Thus we have

$$\mathbf{v}_s \cdot \mathbf{v}_c = 0, \quad \|\mathbf{v}_c\| = c_M, \text{ and } \left(\begin{pmatrix} 1 & 0 & 0 \\ 0 & 1 & 0 \\ 0 & 0 & 0 \end{pmatrix} \mathbf{v}_c \right) \cdot \mathbf{v}_{xy} = 2b.$$

Let $\mathbf{v}_c = \begin{pmatrix} x_c \\ y_c \\ z_c \end{pmatrix}$ and $\mathbf{v}_x = \begin{pmatrix} x_s \\ y_s \\ z_s \end{pmatrix}$. Then $x_c^2 + y_c^2 + z_c^2 = c_M^2$, $x_c x_s + y_c y_s + z_c z_s = 0$, $|x_c \sin\theta - y_c \cos\theta| = 2b$. This system has four solutions due to the squared terms in the first equation and the absolute value in the third. We determine whether $x_c \sin\theta - y_c \cos\theta = 2b$ or $= -2b$ by using the directional information calculated above. It will be negative if the leading edge of the wing is on the clockwise side of the wing and it will be positive if the leading edge is on the counterclockwise side. Let $c_{xy} = 2b$ or $-2b$, as appropriate. We choose to have the chord vector originate along the leading edge of the wing so that the z component is negative. Thus $z_c = -\sqrt{c_M^2 - x_c^2 - y_c^2}$. We find that $x_c = -N_2/(2N_1) \pm \sqrt{N_2^2 - 4N_1N_3}/(2N_1)$ and $y_c = x_c \sin\theta/\cos\theta - 2b/\cos\theta$ where $N_1 = z_s^2 + (x_s \cos\theta + y_s \sin\theta)^2$, $N_2 = c_{xy}(-2z_s^2 \sin\theta - 2x_s y_s \cos\theta - 2y_s^2 \sin\theta)$, $N_3 = z_s^2 c_{xy}^2 + y_s^2 c_{xy}^2 - c_M^2 z_s^2 \cos^2\theta$ and the root of x_c is chosen such that $x_c x_s + y_c y_s + z_c z_s = 0$.

4.2.2 Wing centered reference frame

The span and chord vectors are measured in a reference frame relative to the world, not relative to the insect. To compare two wingstrokes, we need to compensate for changes in body orientation over time. We express the span and chord vectors in a stroke plane centered coordinate frame so that they are comparable even as the insect changes orientation. To determine the orientation of the stroke plane frame in a given instant, we use span vectors drawn from two consecutive wingbeats. Given the locations of the tips of the unit span vectors from each wing over two wingbeats, we compute the principal component analysis axes of these points. The first principal component vector points from one wing to the other. We force it to point from the wing to the right of the head, as seen from the dorsal side, towards the wing to the left. This vector is the pitch axis of the reference frame. The second principal component vector lies within the stroke plane. We construct a vector within the stroke plane that lies perpendicular to the pitch axis and points toward the head

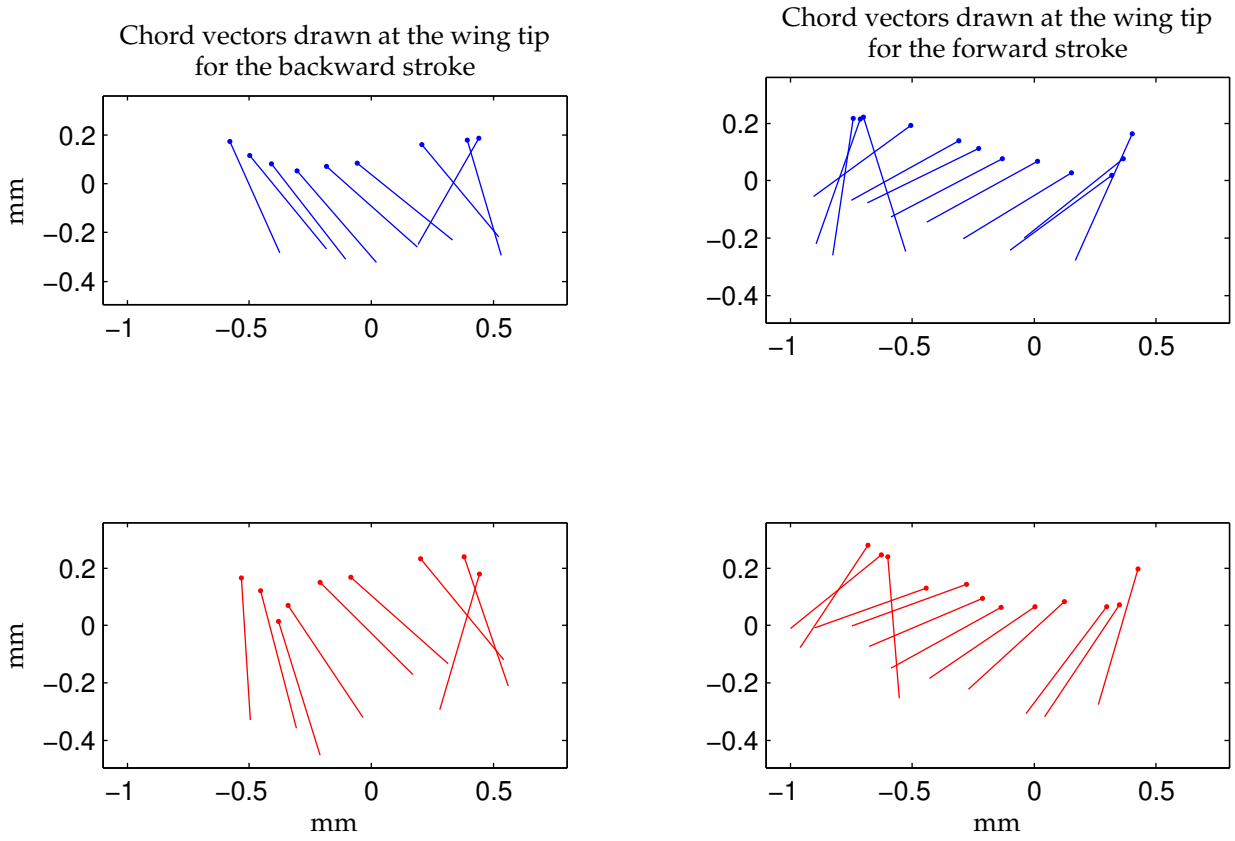

Figure 34: Using phase averaged data from 5 wingbeats, the orientation of the wing during the backward (upstroke) and the forward (downstroke) are plotted for each wing. The dots are plotted at the location of the tip of the leading edge of the wing. The lines are drawn to be aligned with the wing chord. The left wing, as determined from a dorsal view, is shown in blue. The right wing is shown in red. In all four half strokes shown here the wing flip is delayed, occurring after the wing vein has changed direction. For these strokes, the ratio of the distance subtended by the wing at a point located at 0.7 of the full span to the length of the chord, A_0/c, is 1.75. $A_0 = 0.7R\Phi$ where R is the length of the wing span and Φ is the stroke amplitude. On the backward stroke the left wing has little variation in deviation, since there is only a small change in the height of the dots during the stroke. For both wings, the forward stroke is more downward, with a rapid recovery at the end. The stroke angle dictates the horizontal location of the wing tip. It is changing more slowly when the dots are close together and more rapidly when they are further apart. The pitch angle of the wing is the angle of the wing chord relative to horizontal. For these wing motions, it is smallest near the beginning of the forward stroke, after the wing flip occurs. It must pass through 90 degrees during the flip.

of the insect. This vector forms the roll axis. The third vector of the coordinate system is perpendicular to both the pitch axis and the roll axis. It points upward, and is often nearly vertical. This is the yaw axis. The yaw, pitch, and roll axes form the wing stroke coordinate plane. $P_{\mathcal{B}} = [\mathbf{b}_1\ \mathbf{b}_2\ \mathbf{b}_3]$ is a matrix whose columns are the basis vectors of this frame. The wing span and chord vectors have been measured relative to the world frame. To reexpress these vectors in wing frame coordinates, we define $\mathbf{v}_{s\mathcal{B}}$, the span vector expressed in wing coordinates, as $\mathbf{v}_{s\mathcal{B}} = P_B^{-1}\mathbf{v}_s$ and $\mathbf{v}_{c\mathcal{B}}$, the chord vector expressed in body coordinates, as $\mathbf{v}_{c\mathcal{B}} = P_B^{-1}\mathbf{v}_c$.

A wing stroke expressed in the wing frame is illustrated via its chord vectors in figure 34. The x and z components of the chord vectors $\mathbf{v}_{c\mathcal{B}}$ are plotted in in figure 34. We draw a circle at a location 1.7 mm along the span vector, $\mathbf{v}_{s\mathcal{B}}$, at each point during the wingbeat. This point is near the tip of the wing. The circles represent points on the leading edge of the wing. We use these points as an origin for our depictions the chord vector, and draw a 0.54 mm chord vector. This chord length is consistent with measured values. The chord lengths and distance are at the correct scale for the actual insect. The leading edge of the wing subtends a distance of approximately 2.5 chord lengths on each half stroke, while the ratio A_0/c, which is computed at 0.7 of the span, is 1.75. The backward motion of each wing is represented separately in the first column of figure 34. For each wing, the wing flip occurs after the wing vein has changed its direction of motion. The wing translates rapidly just after the wing flip and then translates more slowly as it moves towards the abdomen of the insect. The forward motion of the wings is represented in the second column of the figure.

Given these vector descriptions of the wing stroke, expressed in the wing coordinate frame, we compute angular descriptions of the wing stroke using the xyz convention. The stroke angle of the wing is $\tan^{-1}(\mathbf{v}_{s\mathcal{B}}(1), \mathbf{v}_{s\mathcal{B}}(2))$, the angle relative to the x-axis of the projection of the span vector into the horizontal plane. The deviation angle is $\sin^{-1}\mathbf{v}_{s\mathcal{B}}(3))$, the angle of the span vector relative to the xy-plane. The wing pitch angle is $\sin^{-1}\mathbf{v}_{c\mathcal{B}}$, the angle of the chord vector relative to the xy-plane.

To characterize the wing motion over a wingbeat, we compute the Fourier approximation of each angular description of the wing motion, and retain the most energetic Fourier modes. In the wing coordinate frame, the stroke angle of the right wing of the insect is typically centered about $-\pi/2 - 0.1$ radians, and passes through $-\pi/2$ on each stroke. Our measurement error is particularly low at the center of the stroke when the wing is translating most quickly, so we find all frames where the stroke angle transitions from greater than $-\pi/2 - 0.1$ to less than $-\pi/2 - 0.1$. We linearly interpolate to identify a crossing time, and use this time to demarcate the start of a new wingbeat. We segment each flight into sequences of approximately twenty wingbeats, linearly rescaling time within each wingbeat so that the wingbeat has a duration of 2π time units. Given the wing stroke, deviation, and pitch angles describing the motion of each wing as a function of rescaled time, we use the Fourier approximation capabilities of the functional data analysis package ([57]) to compute Fourier approximations to the three angles.

The stroke angle is closely approximated by $\phi(t) = A_1 + A_2 \sin t + A_3 \cos 2t + A_4 \sin 2t + A_5 \cos 3t + A_6 \sin 3t$, the pitch angle by $\psi(t) = B_0 + B_2 \cos(t + B_3) + B_4 \cos 2t + B_5 \sin 2t + B_5 \cos 3t + B_7 \sin 3t$, and the deviation angle by $\theta(t) = C_1 \cos^2 t + C_2$, where these coefficients are determined for each set of 20 wingbeats. By creating Fourier approximations for each wing we are able to compare coefficients to search for asymmetry between the wings. In addition, we probe which aspects of the wing motion are associated with changes in the body orientation or velocity.

4.3 Results

4.3.1 Flight frequency

In blowflies, wingbeat frequencies are under 200 Hz ([86]) while in fruitflies they are just above 200 Hz ([38]). In male *Aedes aegypti*, wingbeat frequencies are known to be much higher ([51],[7], [9]). The insects we observed were drawn from multiple cohorts, and wingbeat

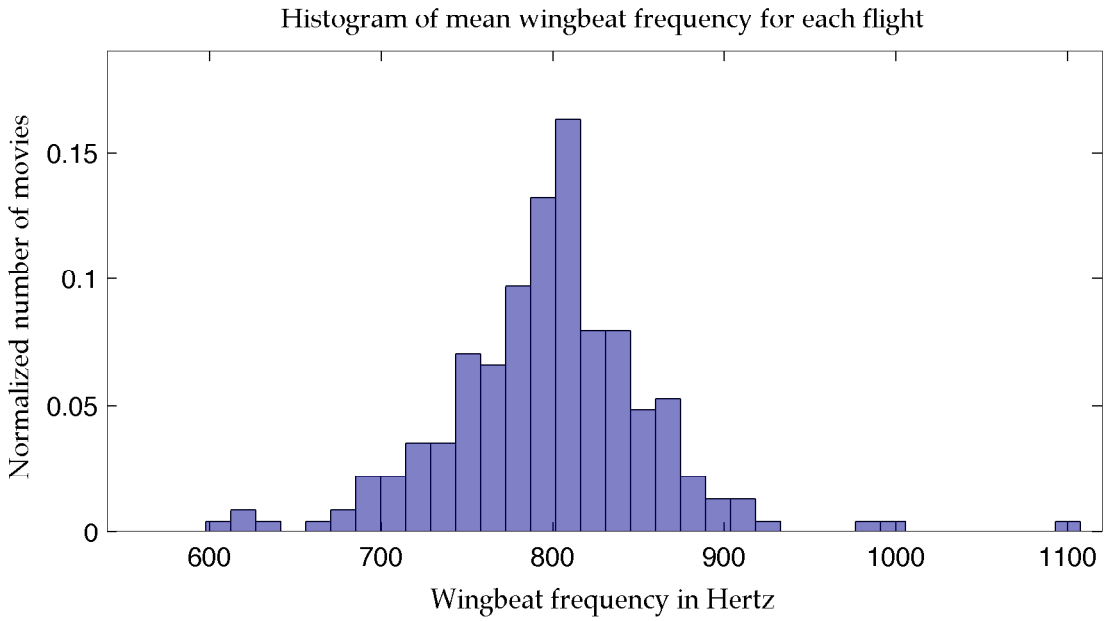

Figure 35: The distribution of the mean wingbeat frequency during a single flight is shown for data compiled from over 200 separate flights. 800 Hz is a typical wingbeat frequency for these free flying male *Aedes aegypti*.

frequency appears to vary by cohort. In one set of 76 recordings, the mosquitoes were reared to be small, and had a mean wingbeat frequency of 839 ± 55 Hz. Two cohorts of mosquitoes reared to be larger had a mean wingbeat frequency of 762 ± 49, over 103 flights. These values are consistent with the measurements in [51]. Using the two-sided Kolmogorov-Smirnov test ([66]), we found that the wingbeat frequency distributions between the two populations were different, with a p-value of $1e-18$. In the cohort of mosquitoes with flight stimulated by female motion, we measured a mean wingbeat frequency of 811 ± 40 during those 48 flights. This distribution was only somewhat different from that of the first cohort, with a p-value of only 0.049. Based on these measurements, the wingbeat frequency of *Aedes aegypti* males appear to vary by cohort. The distribution of wingbeat frequency over all flights, with a single mean frequency recorded for each flight, is shown in figure 35a. At the extreme, in a single flight, seen at the far right of the plot, an insect exhibited a wingbeat frequency of approximately 1100 Hertz, the maximum wingbeat frequency observed.

In blowflies, wingbeat frequency changes have been observed with ambient temperature, with the wingbeat frequency ranging from 138 Hertz in 15 C air to 198 Hertz in 30 C air, a change of more than 40 per cent ([86]). These results are unlikely to translate directly to mosquitoes, as blowflies exhibit enhanced flight performance as temperature increases, while mosquito performance diminishes between 21 C and 27 C ([61]) and is further reduced at higher temperatures. However, mosquito wingbeat frequency may vary with ambient temperature. Our measurements were taken at room temperature, which was approximately 24 C.

We observed variation in wingbeat frequency between flights, and in 73 percent of flights we observed frequency variation over the course of a single flight. When frequency varied during the flight, there was a mean variation of 21 ± 15 Hertz. For flight in the presence of females variation was observed in 71 percent of flights, with a mean variation of 17.8 ± 9.2 Hertz. In the extreme case, we recorded one flight in which the insect increased its wingbeat frequency from 619 ± 16 to 746 ± 12 over 90 ms of flight. This is a 21 per cent increase in frequency. Since flight forces are proportional to the wing area and to the square of the velocity of the wings relative to the air [25], and changes in wingbeat frequency change the wing velocity, changing the wingbeat frequency could potentially be used to adjust the flight forces. A direct dependence of lift force on wingbeat frequency has been found in blowflies ([54]). We find no significant correlations between variation in the wingbeat frequency over the course of a single flight and acceleration or velocity during the flight, however, we average over approximately 20 wingbeats to produce a frequency data point, so the frequency data examined here is somewhat sparse. Perhaps because of the high variation in baseline wingbeat between individuals, comparing across individuals also yields little insight.

Across all individuals, there is a cross correlation of 0.14 ± 0.07 (95 percent confidence interval) between sideways velocity and wingbeat frequency, which is positive with a p-value of less than 0.0001. There is a correlation of 0.10 ± 0.07 between wingbeat frequency and the

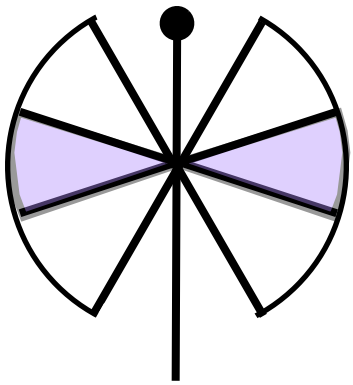

Figure 36: The inner arc (light purple) subtends 36 degrees, or 85 percent of an average mosquito stroke. The outer are subtends 120 degrees, or 85 percent of an average fruitfly wingstroke ([39]). With a larger wing stroke, aerodynamic forces are applied farther from the body pitch axis, potentially leading to larger aerodynamically driven pitch torques over the course of the stroke.

magnitude of roll, which is positive with a p-value of 0.003, and a correlation of 0.30 ± 0.06 between wingbeat frequency and pitch, which is positive with a p-value of less than 10^{-13}. This means that lower wingbeat frequencies weakly correlate with the stroke plane tilting backwards, while higher frequencies correlate with the stroke plane being tilted more forward. The details of how roll and pitch are computed for these calculations are given in Chapter 3. The correlations between pitch and frequency may reflect that wingbeat frequency affects the optimal pitch angle of the insect. In addition, the weak positive correlation between wingbeat frequency and sideways velocity, and with roll, along with no correlation between wingbeat frequency and sideways acceleration, could potentially indicate that the wingbeat frequency is impacted by sideways motion. Although the wingbeat frequency is associated with the insect's pitch, based on this data, the wingbeat frequency is not directly correlated with the insect's thrust.

4.3.2 Stroke angle

The wing stroke amplitude, Φ, is the angle subtended by the wing on each half wingbeat. Many two-winged insects have stroke amplitudes of approximately 140 degrees. The crane flies (*Tipula obseleta* and *Tipula paludoa*), bees (*Apis mellifera*, *Bombus hortorum*, and *Bombus lucorum*) recorded by Ellington in [24] each have stroke amplitudes of greater than 120 degrees. For *Apis mellifera*, Altshuler et. al. find a shorter wing stroke of about 95 degrees during hover, and Dudley and Ellington measure bumblebees as having wingstrokes between 95 and 130 degrees ([23]). Fruit flies consistently subtend between 120 and 160 degrees on each half stroke ([30], [39]). The dronefly *Eristalis tenax* has a stroke amplitude of above 100 degrees ([24]. In contrast to these insects, the hoverfly *Episyrphus balteatus* has a smaller stroke amplitude, subtending $66-95$ degrees on each half stroke ([24]). These large variations in measured stroke amplitude for the same species indicate that stroke amplitude varies between individual insects. In addition to varying between flights, stroke amplitude is often not constant within a single flight. For example, in tethered flights, the blowfly *Calliphora vicina* exhibits large deviations in stroke amplitude at the dorsal end of the stroke ([2]).

We measured Φ for 25 free flights of *Aedes aegypti* males, all recorded at 13029 fps. These flights are made up of $N = 4383$ wingbeats of data, with the stroke amplitude of the downstroke (towards the head) and upstroke (away from the head) measured separately for each wingbeat for each wing. The stroke amplitude was defined as the maximum angle between any two span vectors within the half wingbeat. The mean stroke amplitude over single flights ranged from 34 to 54 degrees. These measurements have an intrinsic error of up to 2 percent due to the limited number of frames recorded per wingbeat. Over all wingbeats, the mean stroke amplitude was 42.8 ± 7.2 degrees. During the course of each flight the stroke amplitude was not fixed. It varied with a mean standard deviation within each flight of 5.4 degrees, or 13 percent of the mean stroke amplitude for the flight. The stroke amplitudes of these insects are substantially smaller than those of the Dipterans described above. They are

approximately half those of the hoverfly *Episyrphus balteatus*. These short stroke amplitudes mean that the wing translates by only a few chord widths on each stroke. For a mosquito with a typical wing span of 1.8 mm and a chord width of 0.54 mm, the leading edge of the wing translates by only 2.5 chords over a typical forward or backward stroke, while a point 0.7 of the way along the span translates 1.75 chords. The latter value is the non-dimensional ratio A_0/c. Wing force generation has been studied experimentally and computationally for the range of A_0/c of 2.8 to 4.8, which are values considered relevant to fruitfly wing motion ([80]). These short wing strokes correspond to a Reynolds number of $Re = A_0 f \pi c/\nu = 76$ where f is the wingbeat frequency and ν is the kinematic viscosity. The comparable Reynolds number derived from crane fly data is 290 ([40]) and from fruitfly data is 150 ([30]).

At the ends of the wingstroke, the wing undergoes rapid rotation. When the stroke amplitude is large, a substantial portion of the stroke is spent in almost pure translation. For mosquitoes, moving their wings with a very small stroke amplitude, the wings are rotating during most of the wingbeat, as is clear from the distribution of changes in wing width shown in figure 30(b). Wing forces during steady translation are well approximated by a quasisteady model, but rapid wing rotation, even at a Reynolds number of 75, causes associated spikes in the wing drag that are not as well captured. Slower wing rotation does not cause these transients ([80]). With the short wing stroke of *Aedes aegypti*, the wing turn-arounds could potentially be an important contributer to net flight forces. This question is examined for bees with a stroke amplitude of approximately 90 degrees by Altshuler et al ([1]). A short wing stroke also may change the magnitude of wing based drag during changes in rotation. Such drag is thought to be an important contributer to turning dynamics ([38], [37]). With a short wingstroke, the location of the center of pressure of the wings varies much less over the course of a wingbeat than it does in an insect with a larger stroke amplitude.

The short stroke angle of the mosquito may reduce the pitch torque that the insect experiences on each wingstroke. During the wing stroke, as the center of the wing moves forward and and then backward along the body relative to the wing attachment point, the

location where aerodynamic forces are acting is similarly shifted. For insects with a large stroke angle, aerodynamic forces are applied at points farther from the pitch axis. This is shown using a schematic in figure 36. This difference may partially account for why pitch actuation is less important to forward thrust generation in the mosquito (Chapter 3) than it is in flies ([50]).

In the measured *Aedes aegypti* free flights, variation in stroke amplitude has a weak positive correlation (0.16) with upward acceleration. In tethered fruit flies, total stroke angle is not always closely coupled to net force production. Instead, at force production below maximum, individuals exhibit variation in the stroke amplitude of about 2.7 degrees, accompanied by variation in the wingbeat frequency. This means that various wing motions generate the same magnitude of force at forces away from the insect's maximum generating capacity ([48]). Thus maximal stroke amplitude corresponds to maximal thrust, but reduced stroke amplitudes may not be accompanied by a proportionate reduction in thrust. Our observations are consistent with this possibility. In addition, variation in stroke amplitude does not correlate with upward velocity, the magnitude of the velocity or the magnitude of the acceleration.

4.3.3 Asymmetries in wing motion

In tethered fruitflies, stroke amplitude varies independently for the two wings in response to visual patterns ([33]), and they exhibit discrete changes in stroke amplitude that can occur independently on each side ([34]). While measuring the intrinsic damping coefficient of the body-wing system in tethered fruit flies during a visual tuning task that required yaw torque, Hesselberg and Lehmann observed stroke amplitude asymmetries of approximately 7 degrees between the two wings ([38]). Large stroke amplitude asymmetries are also observed in tethered blowflies ([54]). Differences in the stroke amplitude between the wings are associated with yaw rotation in fruit flies ([29]). Stroke amplitude asymmetry is also associated with roll torques ([54]), which are more central to mosquito flight than yaw rotation (Chapter 3).

We find that stroke amplitude asymmetry is a subtle effect, if it is present. This is also the case in hoverflies, where the centerpoint of the wingstroke often shifts substantially but there is little asymmetry in stroke angle between the two wings ([78]). In figures 37(d), 38(b), (d), (f), and 40(f), stroke amplitude asymmetries may be present. However, the magnitude of the deviation is approximately 2 degrees, so may be due to measurement error. Mosquito wingstrokes exhibit much more prominent asymmetries between the two wings in their pitch angle than they do in the stroke angle.

The graphs in figures 37, 38, 39, 40, and 41 illustrate the motions of both wings during three flight segments selected from five different flights. In these figures, the time course of stroke plane orientation angles during flight is shown in the top row, The dynamics of insect flight are invariant to changes in yaw (Chapter 5), so yaw (blue) is set to zero at time zero for the purposes of plotting, while pitch (green) and roll (red) are shown with their measured values. Sections of each orientation plot are highlighted in cyan, magenta, and gray. The stroke angles and pitch angles of the wings during the period highlighted in cyan are shown in the first column of each figure, while those from the magenta period are shown in the second column and those from the gray period are shown in the third. The wing pitch angle ranges from 0 to 90 degrees in these plots, with 0 degrees corresponding to a horizontal wing and 90 degrees corresponding to a vertical wing. The wing must pass through 90 degrees during each wing flip. With only 15 frames per wingbeat, errors of a single frame in identifying the wing flip have a dramatic impact on the shapes of the curves, so the pitch angle values do not include directional information. The wing angles are shown relative to the stroke plane, not relative to the direction of insect motion, however, the insect is moving at less than 20 cm/s in all flights shown here, and the maximum wing velocity is approximately 220 cm/s, so the difference between the pitch angle in the stroke plane and the wing angle measured relative to the direction of motion does not exceed 5.3 degrees.

The highlighted sections of each flight last from 5 to 30 wingbeats. During these periods, the motion of the wing during each individual wingbeat is graphed separately, so many

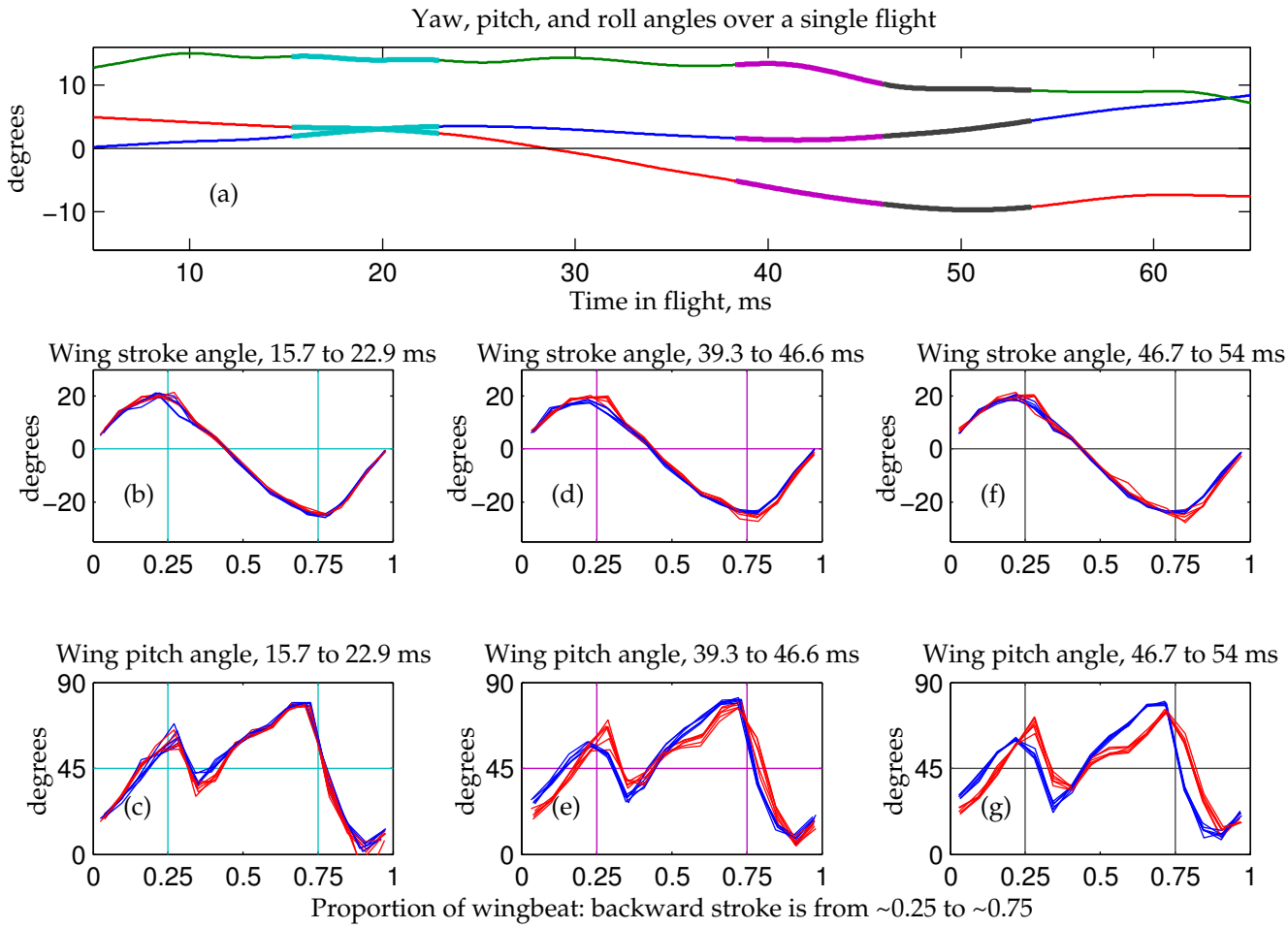

Figure 37: In (a), yaw (blue line), pitch (green line), and roll (red line) angles describing the orientation of the stroke plane are plotted against time for a single flight. Yaw is plotted with the initial yaw set to zero in the plot. Roll (red) varies from positive to negative over the course of the flight, and pitch remains at near 15 degrees until about 40 ms when it drops to 8 degrees. In (b) and (c) the wing stroke angle and pitch angle are shown for five superimposed wingbeats corresponding to the time period marked in cyan in (a). All wing angles are shown relative to the stroke plane frame of reference. The stroke angle is recentered so that positive angles correspond to positions closer to the head and negative indicate locations further from the head. The angle itself is the angle of the projection of the wing leading edge into the stroke plane, and is measured relative to the pitch axis. This means that zeroes correspond to a location 90 degrees away from the yaw angle of the frame. The wing pitch angle is the angle of the wing chord relative to the stroke plane so that zero corresponds to the wing lying flat in the stroke plane and 90 corresponds to the wing being perpendicular to the stroke plane. In (d) and (e), wing stroke angle and pitch angle are plotted for six wingbeats corresponding to the magenta period in (a). In (f) and (g), wing stroke angle and pitch angle are plotted for six wingbeats corresponding to the gray period in (a). A downstroke/upstroke asymmetry in the wing flip appears in all three segments. In (e) and (g), pitch angle asymmetries between the two wings are also present.

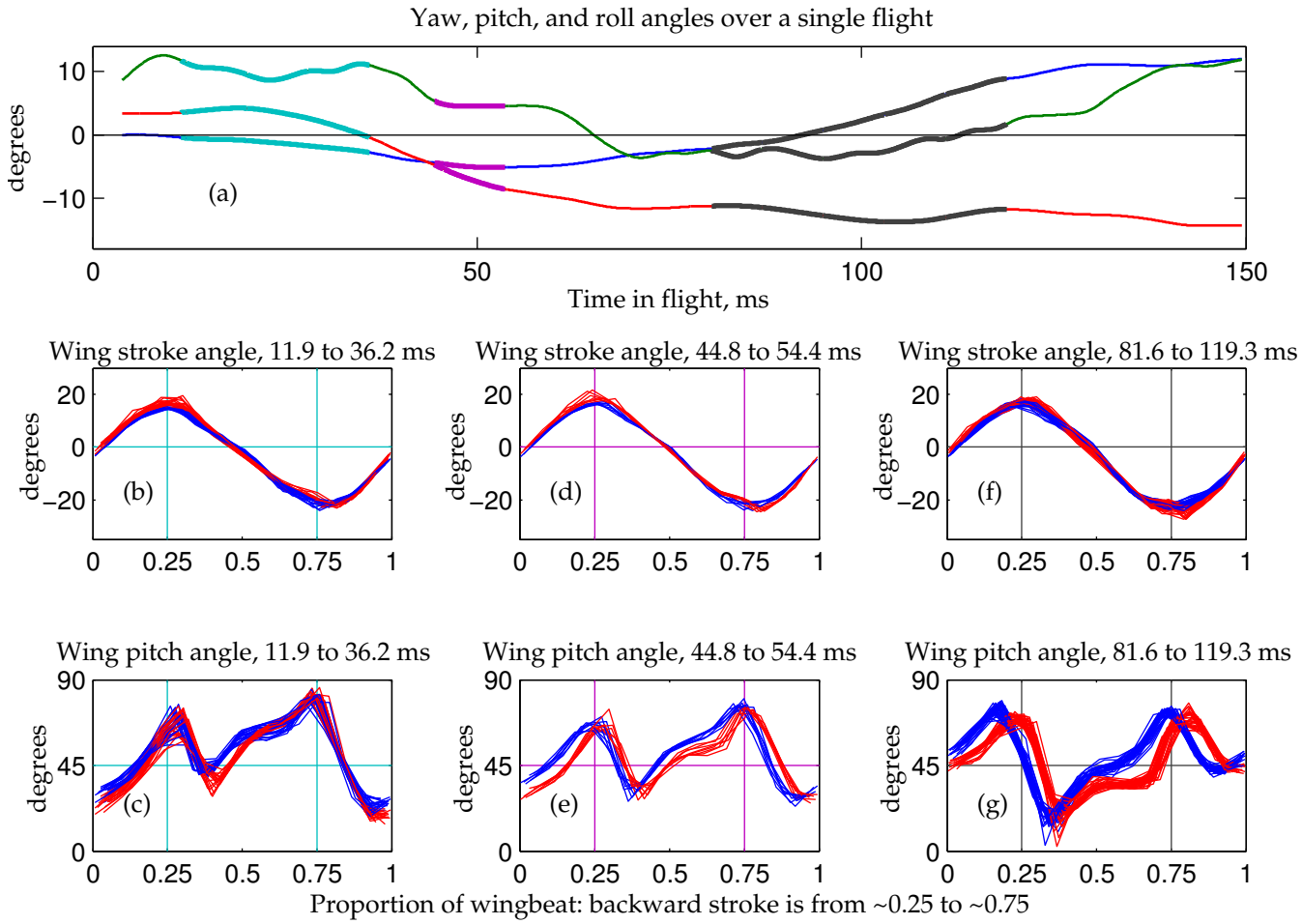

Figure 38: In (a), the stroke plane angles are shown during 150 ms of flight. The yaw angle (blue), pitch angle (green), and roll angle (red), are each varying over the course of the flight. The wing motion during the segment highlighted in cyan is shown in (b) and (c). This period is 20 wingbeats in duration. The motion of the wing during each wingbeat is plotted separately and is consistent over time during this period. The wing motion during the magenta period, which is 8 wingbeats in duration, is shown in (d) and (e). Wing motion during the gray period, which lasts 31 wingbeats, is detailed in (f) and (g). A downstroke/upstroke asymmetry in the wing flip appears in (c) with the opposite asymmetry appearing in (g). Asymmetries in pitch between the two wings are clearly present in (e) and (g), with the left wing (blue) delayed at the downstroke/upstroke wing flip and the right wing (red) delayed at the upstroke/downstroke wing flip in (g). These wing motions also include periods of steady translation during the upstroke.

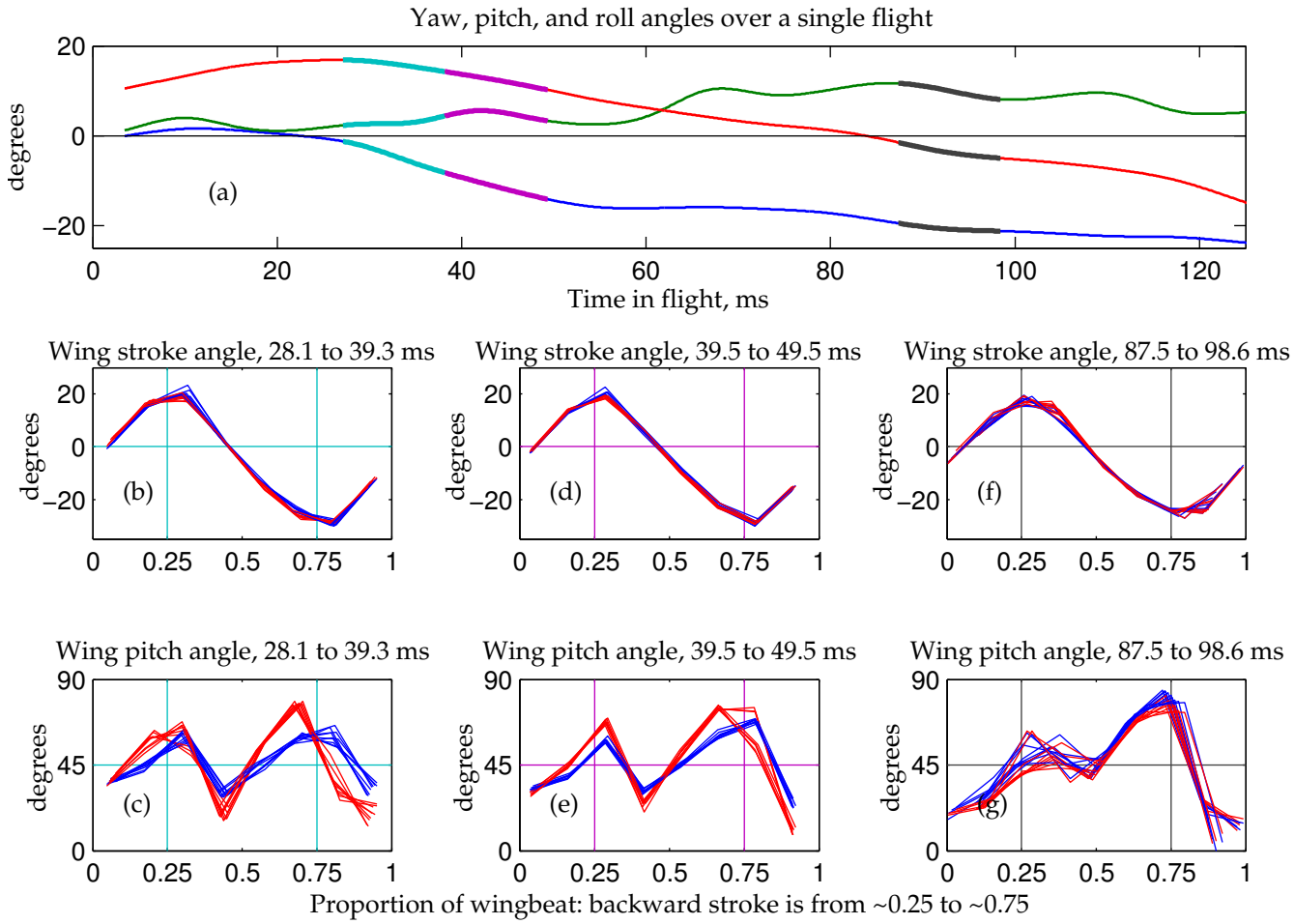

Figure 39: In (a), the stroke plane angles are shown during 125 ms of flight. The yaw angle (blue), pitch angle (green), and roll angle (red), are each varying over the course of the flight. The cyan period (9 wingbeats) is detailed in (b) and (c), the magenta (10 wingbeats) in (d) and (e), and the gray (9 wingbeats) in (f) and (g). This data was collected at 6309 frames per second, so there is sparse information from each wingbeat. However, during the cyan and magenta time periods, wing pitch asymmetries are clearly visible in (c) and (e).

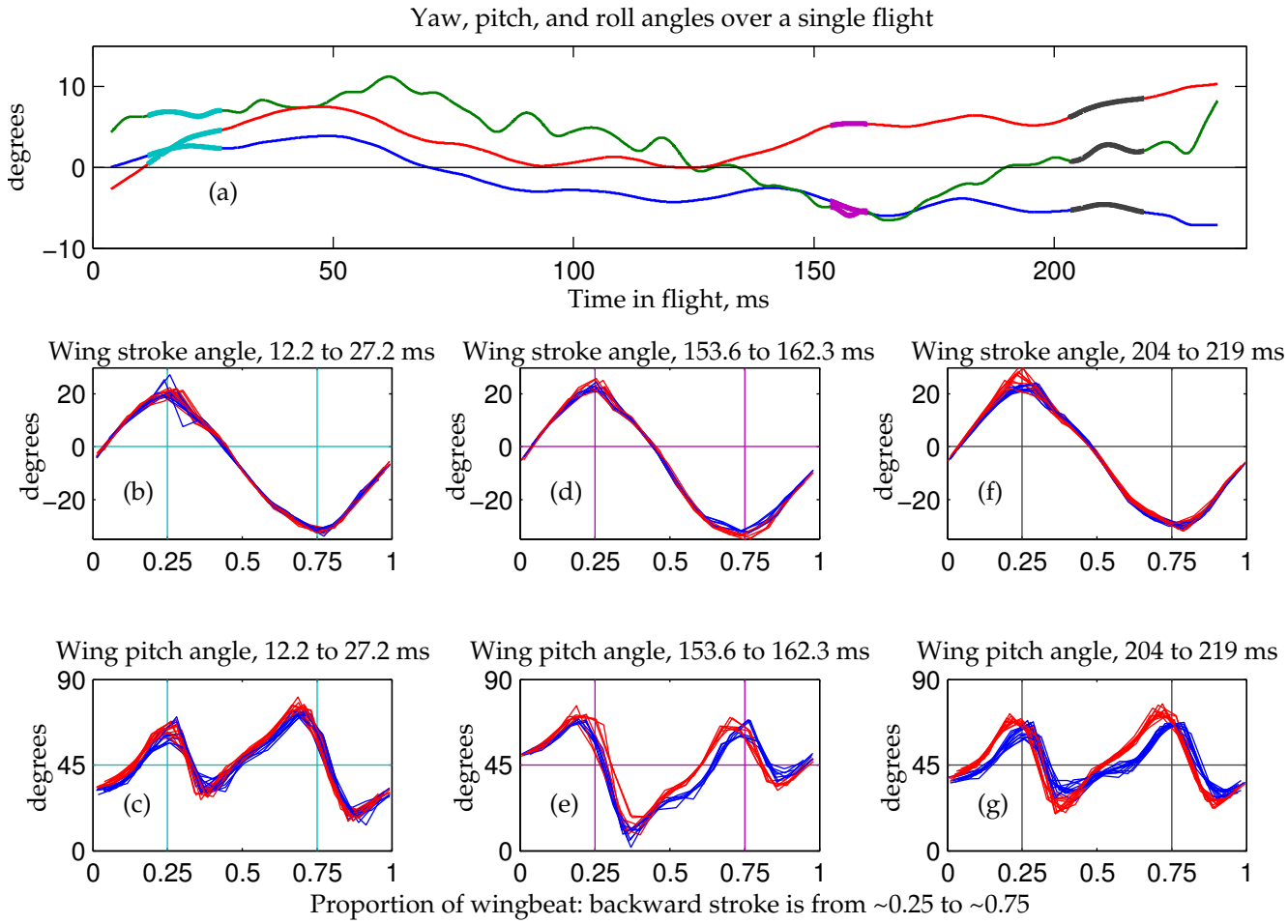

Figure 40: In (a), the stroke plane angles are shown during over 200 ms of flight. The yaw angle (blue), pitch angle (green), and roll angle (red), are each varying over the course of the flight. The cyan period (12 wingbeats) is detailed in (b) and (c), the magenta (7 wingbeats) in (d) and (e), and the gray (12 wingbeats) in (f) and (g). The downstroke/upstroke wing flip asymmetry appears in (c) and (e). The upstroke/downstroke transition is advanced in (c) and there are timing asymmetries between the two wings in (e) and (g).

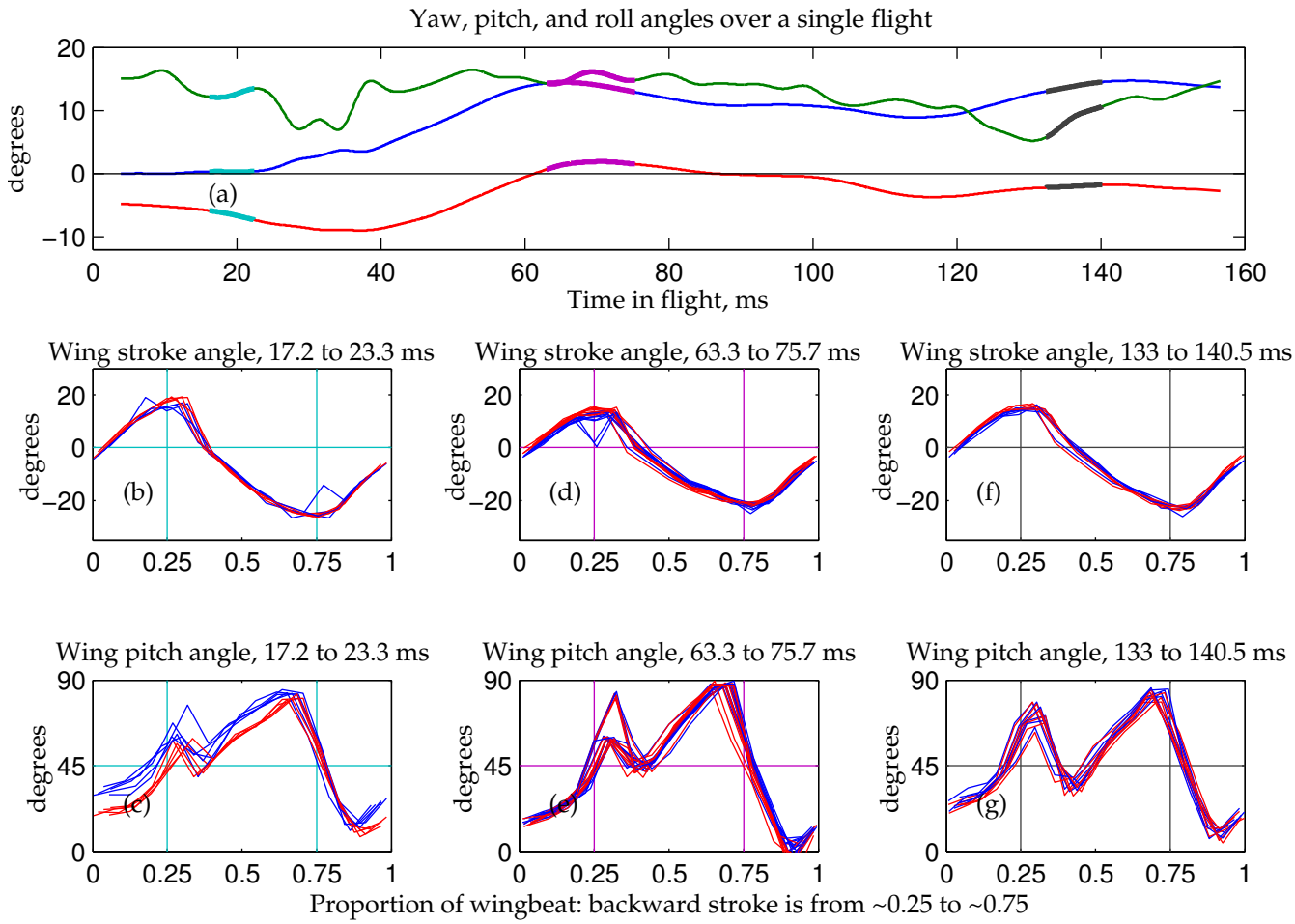

Figure 41: In (a), the stroke plane angles are shown during approximately 150 ms of flight. The yaw angle (blue), pitch angle (green), and roll angle (red), are each varying over the course of the flight. The cyan period (5 wingbeats) is detailed in (b) and (c), the magenta (10 wingbeats) in (d) and (e), and the gray (6 wingbeats) in (f) and (g). The downstroke/upstroke wing flip asymmetry appears in all three segments. In (e), the downstroke/upstroke wing flip appears to be delayed while the upstroke/downstroke flip is advanced, relative to the stroke. Advancedment is also present in (c) while delay is present in (g).

wingbeats of data are superimposed upon each other in the graphs. The agreement in stroke motion during these times indicates that the structure of wing motion is persistent. The wingbeats were segmented based on when the stroke angle of the left wing (blue), as seen from the dorsal side of the insect, passed through -0.1 radians, with the crossing time determined using linear interpolation. Each wingbeat was individually rescaled to a duration of one time unit. In rescaled time, the backstroke occurs from time 0.25 to time 0.75. In actuality, wingbeats typically last approximately 1.25 ms.

In figure 37, variations in motion between the two wings are readily apparent in graphs (e) and (g), where the timing of rotations in wing pitch angle differs between the two wings. During the cyan period in (a), where stroke plane pitch is steady while yaw and roll are changing slowly, the wing motions, shown in (b) and (c), are symmetric between the two wings within the resolution of these measurements. During all three periods a downstroke/upstroke asymmetry is present in the wing motion, where the plunge in pitch angle after the upstroke brings the wing close to horizontal, while the plunge at the end of the downstroke falls to only slightly below 45 degrees. After a wing flip, during the upstroke, the wing pitch angle either increases steadily throughout the rest of the half stroke (37(c) both wings, (e), (g) left wing, 40(c) left wing, 41(c), (e), (g) both wings), or rotates, then enters a period of translation, and then rotates again (37(e), (g) right wing, 38(c), (e), (g) both wings, 40(e), (g) both wings). The asymmetry in the wing flip, where the wing plunges to horizontal after the upstroke and to 45 degrees after the downstroke, is also present in 38(c), 39(g), 40(c), and 41(c), (e), and (g). When it is present, the wing spends most of the downstroke more horizontal than 45 degrees, and most of the upstroke more vertical than 45 degrees. This within-stroke asymmetry occurs in both wings when it is present.

The opposite asymmetry, where the wing approaches horizontal during the wing rotation after the downstroke and approaches 45 degrees during the rotation after the upstroke, also occurs in 38(g), and 40(e), and also occurs in both wings simultaneously. These types of strokes are associated with a drag asymmetry that produces nonzero net thrust, because

the wing has a narrow profile relative to its direction of movement one half stroke and a wide profile during the other ([58]). If we account for the acceleration needed to overcome drag, then the total forward acceleration $a_x + 4v_x$ is positive during the first set of flight segments and negative during the second set, as expected. Here, a_x is the measured forward acceleration and v_x is the measured forward velocity. The drag coefficient of $k = 4\ \mathrm{s}^{-1}$, is the coefficient we found for sideways motion (Chapter 3), and is consistent with that measured for fruitflies during forward motion ([50]).

In figure 37(c), the asymmetry in rotation between the upstroke and downstroke is dramatic. In addition, during these wingbeats the wing flip occurs in advance of the downstroke, rather than simulteously with the wing turnaround. In this case, this advanced rotation is not present before the upstroke. The advanced rotation of the left wing (blue) persists in figures 37(e) and 37(g), while the motion of the right wing (red) changes over the course of the flight. Advanced rotation can also occur before the upstroke, as exemplified by the left wing in figure 38(g). The wing flip can also be delayed, as in the right wing in figure 38(g). In figure 41(g), rotation is slightly delayed at the end of the downstroke and is slightly advanced at the beginning of the upstroke, while in figure 40(e) and (g) the wing flip may be slightly advanced during both strokes for the right wing (red). We thus observe a number of combinations of flip timing: synchronized at the down to up transition and delayed on the up to down transition (38(g)); delayed and then synchronized (38(c)); advanced and then synchronized (38(g)); synchronized and then advanced (37(g)); delayed and then advanced (41(e)); and synchronized on both (38(e)). Unlike the downstroke/upstroke wing flip asymmetry, these timing shifts can appear in just one wing. This effect is most pronounced in the flight segment shown in figure 38(g), but is also apparent at other times.

The downstroke to upstroke transition appears to be delayed more often, while the upstroke to downstroke appears to be advanced more often. In work by Sane et al, delayed rotation causes substantial enhancements to the drag force at the beginning of the half stroke as compared to a symmetric stroke, and advanced rotation causes transient increases in drag

at the end of the half stroke while still producing a peak in drag at the beginning of the next half stroke ([63]), so delay at the beginning of the upstroke and advancement at the end of the upstroke may be forward thrust generating mechanisms. Delay and advancement of the wing flip create the appearance of a timing asymmetry in the wingstroke. While the leading edge of the wing spends the same amount of time on the upstroke and the downstroke, the upstroke can appear to be substantially shorter than the downstroke if the time of wing flip is used to measure stroke timing. Judging timing in this way, in over one quarter of flights ($N = 73$), at least 10 percent more frames are part of the downstroke compared to the upstroke, while only 2 flights (3 percent) have more than 10 percent more frames in the upstroke as compared to the downstroke.

The percentage of excess downstroke frames in a flight correlates strongly with the mean forward velocity of the insect during the flight (correlation coefficient of 0.75), has a moderately positive correlation with mean forward acceleration (0.29) and a moderately negative one with mean sideways acceleration (-0.22). The correlation with the mean of $a_x + 4v_x$, the drag adjusted forward velocity, is 0.48. It is lower than the correlation with forward velocity alone, but is consistent with the potential for these shortened strokes to lead to enhanced drag during wing rotation. The strong correlation with forward velocity may indicate that a passive response to increased forward velocity plays a role in generating the timing asymmetry. Applying a model developed by Ishihara et al, the wing flip will be advanced in the mosquito via a passive process if the normalized spring constant for pitch is greater than 50 g/s^2, and will be delayed if the spring constant is less than this value, where crane flies have an estimated normalized spring constant of 190 ([40]). However, the impact of forward velocity on passive pitching was not included in the model.

The impact of adjustments to the timing of the wing flip on flight forces has been studied experimentally ([20], [63], [80]). In an experiment by Wang et al, advanced rotation causes a lift enhancement during the wing flip that is beyond the lift due to simultaneous rotation in every other half stroke ([80], see figure 2A). In experimental work by Dickinson et al, it

causes a lift enhancement before and after rotation on each half stroke ([20], see figure 3A). We find a weak negative correlation (-0.19) between the percentage of excess downstroke frames and the insect's mean vertical acceleration. It is beyond the scope of this work to differentiate between strokes shortened due to a wing flip delay at the end of the downstroke, those shortened by a wing flip advance at the beginning of the upstroke, and those strokes shortened because both occur. Higher resolution data near the wing flip might make it possible to assess the role of advanced or delayed rotation in generating lift for these insects. The speed of the wing flip is also important to the generation of transient flight forces ([1], [80]). Whether the speed of rotation before the wing flip, which varies substantially with the presence or absence of a translational phase in the half stroke, rather than the speed of the wing flip itself, creates these transients requires further investigation.

Asymmetries in force generation between the two wings lead to torques that are likely central to the generation and control of body rotation. Body orientation changes constantly in mosquitoes, as is visible in graph (a) of the flight figures, and the insect's roll orientation is of particular dynamic importance (Chapter 3). We detail asymmetries between the two wings that may contribute to roll control. Although the depth of the wing flip is always similar between the two wings, the timing of the wing flip, as well as the presence or absence of a translational phase in the wing motion, varies. When a translational phase is present in one wing and absent in the other (37(c), (g)), it creates a pitch asymmetry between the two wings. Such asymmetries drive turns in fruitflies ([5]) and certainly generate torque. When the timing of the wing flip varies between the two wings, this may directly generate torques because of the importance of the relationship between wing flip timing and stroke turnaround in force generation ([20]). However, it also creates a pitch angle asymmetry between the two wings, because the wing that flips first has a lower pitch than the other wing during initial rotation and thus produces reduced drag. The pitch angle of the advanced wing begins to recover its pitch first as well, so for the 3/4 of the half stroke during which the wing pitch is steadily increasing, it produces enhanced drag. Often, it is further from 45 degrees during

this time, so may be producing reduced lift (see 37(g), 40(e), 41(g)) compared to the lagging wing, however this is not always the case (see 40(g)).

4.4 Discussion

There are a number of prominent asymmetries in motion between the two wings that likely generate the torques that drive the frequent body rotation exhibited by mosquitoes. The wing motion patterns we present are persistent for up to tens of wingbeats with little variation, maintaining any asymmetry between the two wings or between the upstroke and downstroke throughout that time. In blowflies, persistent variations in wing motion are associated with the activation of particular flight muscles ([54], [2]) and this is also potentially the case in mosquitoes. In these mosquitoes, we do not observe obvious variation in stroke amplitude between the two wings. Low variation in stroke amplitude has also been observed in droneflies ([78]) and is in contrast to measurements of fruitflies ([38]). The motion of the leading edge of the wing is consistent between the two wings, and also between the upstroke and the downstroke. Although apparent upstroke/downstroke timing asymmetries exist when the length of the wingbeat is quantified using the time of wing flip, the motion is symmetric when the stroke turnaround time is used instead. Speed asymmetries in the motion of the leading edge are considered a potential mechanism for generating roll ([82]) but do not appear to be present in mosquitoes.

Wing pitch asymmetries are a prominent aspect of mosquito wing motion. As the wing flips during wing rotation, it reaches a minimum angle, which is between horizontal and 45 degrees, before immediately increasing. This flip often reaches substantially different angles on the upstroke and downstroke, with the minimum angle differing by more than 30 degrees. This angle is relatively symmetric between the two wings, with differences of less than 10 degrees, so appears to be set for both wings together.

Although both wings experience a similar depth of plunge at the wing flip, the timing

of this varies between the wings, with one wing sometimes plunging 5 percent of the stroke before the other. This variation in timing drives force asymmetries between the two wings in multiple ways. From experimental work on scale models, variation in the timing of wing rotation relative to the timing of wing turnaround has been associated with transient force spikes ([20], [80]). Variation in the speed of wing rotation is also associated with large variations in the force associated with the wing flip [1]. In experiments with actively actuated wings, these transients are strongly dependent on the the geometry and timing of the turn. They are slightly reduced when the wing is allowed to pitch passively verses when the same motion is imposed actively ([40], see figure 6). Whitney and Wood find that inertial contributions by the wing during rotation are an important contributor to net force production ([82]). These may not be well captured by experimental measurements on actively, rather than passively, pitched wings. Estimating the magnitude of the force asymmetries generated by this gap in the timing of rotation requires further investigation.

The alteration in the timing of rotation between the two strokes also directly adjusts the relative pitch angle of the wings. When the left wing rotates first, it is closer to horizontal than the right wing during the plunging portion of the half stroke (see figure 37(e), (g), and figure 38)(e), (g)). Its pitch then increases before that of the right wing, so that it is more vertical for the remainder of the half stroke. This type of pitch asymmetry, observed without the difference in wing flip timing, has been shown to drive turns in fruitflies ([5]). Whether this timing alteration is itself important because of the transient forces produced by varying wing timing, or its main contribution is from shifting the motion of the two wings so that their angles of attack are maintained at a persistent offset, is not clear from this data and would require further investigation. The mechanisms by which mosquitoes are able to independently vary the timing of the two wings, is also an area for further study.

In these mosquitoes, shifts in the timing of wing rotation also occur in both wings simultaneously, as can be seen at the end of the upstroke in figures 37(c), 40(c), and at the end of the downstroke in figure 41(g). Such simultaneous shifts do not generate roll or yaw torque,

but could constribute to force asymmetries between the upstroke and the downstroke, driving forward thrust. With most observed forward thrust unexplained by body pitching in mosquitoes, upstroke/downstroke asymmetries are likely an important component of thrust production. Shifts that either advance the wing flip at the upstroke/downstroke transition, or delay the wing flip at the downstroke/upstroke transition, are common and correlate with estimated forward thrust. At the same time, they correlate strongly with forward velocity so may be partially a passive phenomenon that occurs in response to motion.

Mosquito wings move at a lower Reynolds number even than fruitfly wings, subtending remarkably small angles on each stroke, and wing rotation and timing asymmetries between the two wings are prominent aspects of the stroke. Although the importance of the speed of wing rotation and of wing flip timing to force generation has been well documented ([40], [20], [80], [1]), Reynolds numbers relevant to mosquitoes are not always included, and short wingstrokes with short or missing translational periods have not been studied. Further work has the potential to illuminate the mosquito's ability to tightly control its roll angle, the most dynamically important of its body orientation angles. Understanding how mosquito wing motion drives maneuvering also has the potential to unveil novel flight control mechanisms, and is an important area for future investigation.

Chapter 5

Simulation for understanding mosquito stability

5.1 Introduction

Determining the timescale on which active control by the insect is necessary for sustaining flight is central to understanding insect flight control. If a flying Dipteran is vulnerable to instabilities that grow quickly relative to the timescale of feedback from its visual system and its halteres, then it could potentially be constrained to a narrow range of wing motions and body positions and velocities to be able to fly successfully. In blowflies, feedback from the halteres reaches the neck muscles within 5 ms ([62]) while the visual system shows latencies of 25 to 50 ms ([81]). If instabilities grow on a slower timescale then mosquitoes may avoid the limits of their flight capabilities, or may be able to fly under visual control. Bees are not Dipterans, and lack halteres, so they face a slightly different stabilization problem from that of mosquitoes and fruitflies ([6]). However, for bees trying to fly forward in the face of turbulent wind, flight control does appear to become difficult, with side to side rolling developing at intermediate forward flight velocities. This rolling is more common at higher speeds, and eventually forces the insects to cease their flight ([13]). For fruitflies, constraints

in wing motion occur when they are generating maximal thrust. Such constraints may compromise their maneuverability and stability ([48]). These results suggest that some insects can reach body states during flight that are at the limit of stabilizability.

To study insect stability, it is common to use time averaged models ([72], [56]) where insect stability is treated similarly to helicopter or airplane stability. Insects fly by flapping their wings, which means that, in contrast to airplanes, they can generate lift without forward motion. For mosquitoes, sideways thrust is generated by tilting the body, but forward thrust is generated independently (see Chapter 3), so their control environment is also unlike that of helicopters. In time averaged models, the insect is modeled as a single rigid body whose motion is forced by time averaged aerodynamic forces and whose stability is analyzed using aircraft equations of motion ([56]). Neither airplanes nor helicopters are a good analog for insect flight controls, and while time-averaged models neglect interactions between the wings and body that distinguish insect flight from non-flapping flyers, Wu and Sun found that this approximation has little impact on the computed eigenvalues of the system for droneflies. This is because dronefly body oscillations are small during the stroke ([84]). The largest eigenvalues they identified were $1.046 \pm 0.101i$ using a map computed for a coupled body-wing system, and $0.047 \pm 0.094i$ for the time averaged analogue. These values are comparable in terms of their stability implications because eigenvalues of a map transition from stable to unstable when $|\lambda|$ increases through 1 while eigenvalues of a flow move from stable to unstable when $Re(\lambda)$ passes through 0. Computing singular values for the matrices identified by Wu and Sun, the largest singular value for the coupled model is 1.61 in their flapping system, while the largest singular value for the flow is 1.0. For the dronefly, while the time averaged technique captures information about asymptotic stability by replicating the eigenvalues, is does not preserve all relevant structure.

Using a time-averaged model, Xu and Sun compute lateral stability of a bumblebee during hovering and forward flight ([85]), and find that lateral motion transitions from unstable to weakly stable as forward speed increases. This is in contrast to the observations by

Combes and Dudley described above, where they find that bees appear to encounter an oscillatory lateral instabilities when flying at intermediate speeds ([13]). Gao et al apply such simplified models to *Drosophila*, and find divergence in at least one state variable for the six perturbations that they study ([31]). Karásek and Preumont examine the impact of varying the aerodynamic model on stability results in the time averaged system ([42]). They find that longitudinal results were consistent across a range of aerodynamic models while translational quasi-steady models and CFD models are not in agreement for the lateral stability of the system. Faruque and Humbert also apply time averaged techniques to fruitfly stability. They find an oscillatory motion on the stable side of the stability boundary during lateral motion ([28]) and an unstable oscillatory longitudinal mode ([27]).

We use the numerically robust rigid body simulation software, TREP, developed by Johnston and Murphey ([41]) coupled with a quasisteady aerodynamic force model to assess the stability of mosquito motion. The six degree of freedom mosquito body is coupled to two wings, each with three degrees of freedom relative to the body. Periodic wing motion is imposed based on wing motions measured in Chapter 4. The wings are forced to move symmetrically at all times during this analysis. We identify body initial conditions that correspond to periodic motions of the body under the periodic forcing imposed by aerodynamic and inertial forces generated by wing flapping. By examining the growth or decay of perturbations to the body initial conditions, we find that these periodic body motions lie near the boundary between stability and instability. They are weakly unstable at low forward velocities and weakly stable at higher forward velocities. Although we find eigenvalues close to 1, so that perturbations are slow growing in the long time limit, we find that the system is not self adjoint. This non-normality means that stable directions are close to unstable ones, and that there may be rapid short term growth of perturbations even while the long term growth of perturbations is slow. Specifically, we find a largest singular value of greater than 1.76 in the longitudinal direction and greater than 1.7 in the lateral direction. These values provide an upper bound for the growth of perturbations, but correspond to rapid short term

perturbation growth.

5.2 Methods

5.2.1 Geometry of the rigid body system

Script 1 The kinematic tree specification of the insect is shown below. The insect body has six degrees of freedom (BTX, BTY, BTZ, BRZ, BRY, BRX), while each wing has three degrees of freedom (WRZ1, WRX1, WRY1, WRZ2, WRX2, WRY2).

```
frames = [
  tx('BTX'), [
    ty('BTY'), [
      tz('BTZ'), [
        rz('BRZ'), [
          ry('BRY'), [
            rx('BRX', name='B', mass=(thorax_mass, Ixt, Iyt, Izt)), [
              tx(_c.xdH),[
                tz(_c.zdH, name='H', mass=(head_mass, Ixh, Iyh, Izh))],
              tx(_c.xdA),[
                tz(_c.zdA),[
                  ry(_c.angA,name='A',mass=(abdomen_mass, Ixa, Iya, Iza))]],
              # Wing has 0 pitch when horizontal
              ry(-body_pitch), [
                tx(wing_attach_x), [
                  ty(wing_attach_y), [
                    tz(wing_attach_z,name='W1o'), [
                      rz('WRZ1',kinematic=True), [
                        rx('WRX1',kinematic=True), [
                          ry('WRY1',kinematic=True), [
                            ty(wing_span, name='W1com', mass=(wing_mass, Ixw, Iyw, Izw))]]]]]]],
              #  The wing angles are stroke (WRZ), deviation (WRX) and pitch (WRY).
              #  This is not the xyz convention.  It is a yxz convention.  The wings
              #  start perpendicular to the body axes for their zero.
              ry(-body_pitch), [
                tx(wing_attach_x), [
                  ty(-wing_attach_y), [
                    tz(wing_attach_z,name='W2o'), [
                      rz('WRZ2',kinematic=True), [
                        rx('WRX2',kinematic=True), [
                          ry('WRY2',kinematic=True), [
                            ty(-wing_span, name='W2com', mass=(wing_mass, Ixw, Iyw, Izw))]]]]]]]
]]]]]]
```

In these simulations, the insect is represented as a rigid body constructed of a fused head, thorax, and abdomen, and two rigid wings attached to the body at fixed points of connection. The moments of inertia for the head, thorax, abdomen and wings are generated by modeling each with an ellipsoid. The ellipsoid dimensions are selected to match dimensions measured from motion capture footage. The head is measured to be a sphere of radius 0.18 mm, the

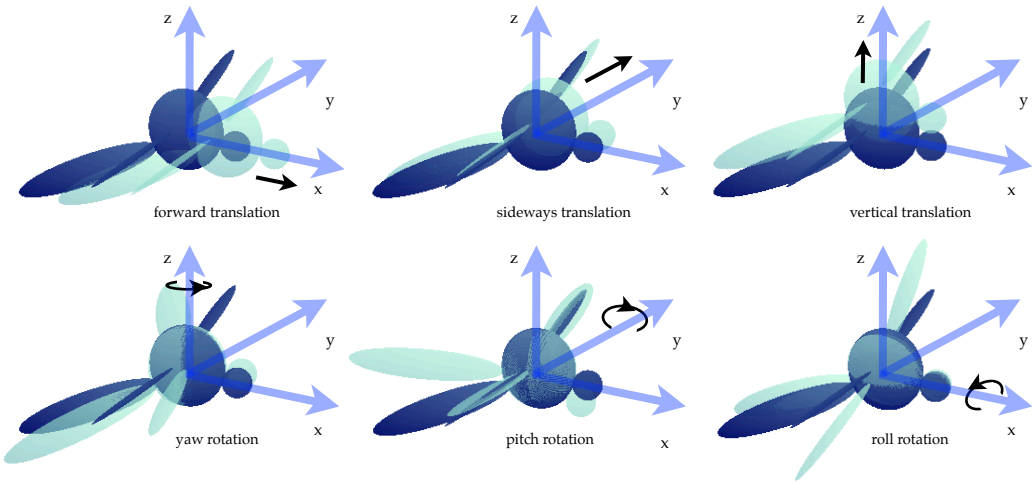

Figure 42: The body in shown in an initial position (dark blue) and in a shifted or rotated position (light cyan). The x axis aligns with the body centerline, the y axis points along the wing perpendicular to the x, and the z axis is in the vertical direction. The body can shift forward or backward, can translate sideways, or can shift vertically. These motions are shown in the top row. In addition, the insect can yaw, meaning it rotates about the z axis, it can pitch, meaning it rotates about the wing-aligned axis, and it can roll, meaning it rotates about the body centerline. These rotations are shown in the bottom row.

thorax to be a near spherical ellipsoid with radii 0.31 mm, 0.25 mm, and 0.41 mm, and the abdomen an elongated ellipsoid, with radii 0.94 mm, 0.94 mm, and 0.20 mm. For simplicity we simulate a 1.0 mg insect. Using an electrobalance, measured body masses ranged from 0.75 mg to 1.2 mg when we weighed a small subset of the unmated males that were used for flight observations. We assume the insect has a constant density within each body segment. The head is assigned a mass of 0.02 mg, while the thorax weighs 0.6 mg during simulations, and the abdomen contains the remainder of the insect's mass. These values are based upon measurement, but since fluid is lost with each cut in the process of separating the body segments, the values only approximate those of an actual insect.

The body has three translational and three rotational degrees of freedom, so it can move forward or backward, sideways, and upwards or downwards, as shown in figure 42. In addition, the body yaws about its vertical axis, pitches about its sideways axis, and rolls about its forward axis. This is also detailed in figure 42. Fully specifying the body position, and

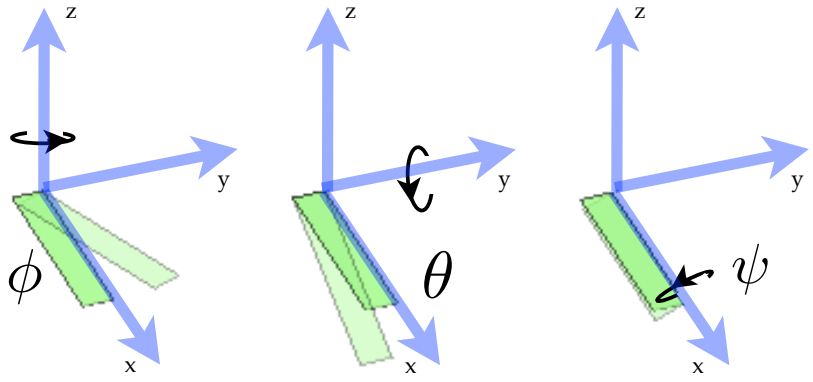

Figure 43: Rotation about the z axis is the wing stroke angle, ϕ, rotation about the y axis is the wing deviation angle, θ, and rotation about the x axis is the wing pitch angle, ψ.

orientation, along with corresponding body velocities leads to a twelve dimensional body state space. The presence of gravity in the system means that the equations of motion, although invariant to changes in the three position variables and to changes in yaw orientation, are sensitive to changes in body pitch and body roll angles. There are thus eight degrees of freedom that are dynamically important to describing the motion of the body.

Measured wings had a mass of approximately 0.001 mg, and this value is used for each wing during simulation. The wing is assumed to be an ellipsoid with half span 0.78 mm, half chord 0.23 mm, and half width 0.03 mm. The wings are attached to the body via joints with three degrees of freedom, allowing the wing to yaw, pitch, and roll relative to the body. These angles are referred to as the wing stroke angle, the wing deviation angle, and the wing pitch angle. As shown in figure 43, stroke angle refers to wing rotation about a vertical axis, deviation to rotation about a chord aligned axis and pitch to rotation about a spanwise axis. We vary the location of the wing attachment point relative to the body center of mass, which enables us to characterize the sensitivity of the system to changes in body mass distribution.

Throughout the simulations, wing motion is specified using a parametric description that is based upon measured insect motions drawn from motion capture data. These measurements are described in Chapter 4. The stroke angle, $\phi(t)$, the deviation angle, $\theta(t)$, and the

pitch angle, $\psi(t)$, are specified by

$$\phi(t) = A_1 \sin(2\pi t/P) + A_2 \sin 2(2\pi t/P) + A_3 \sin 3(2\pi t/P) + A_4$$

$$\theta(t) = B_1 \sin^2(2\pi t/P) + B_2$$

$$\psi(t) = C_1 \cos(2\pi t/P + C_2) + C_3 \cos 3(2\pi t/P) + C_4$$

where A_1 ranges from 0.40 to 0.55, $A_2 \approx 0.01$, $A_3 \approx -0.01$, and $A_4 \approx -0.17$. $B_1 \approx 0.08$, and $B_2 \approx 0.0$. Finally, $C_1 \approx 1.3$, $C_2 \approx 0.36$, $C_3 \approx -0.2$, and $C_4 \approx -0.004$. In addition, the wingbeat period, $P = 1.2$ ms, is specified so that the wing beats at 833 Hertz, which is a typical wingbeat frequency for *Aedes aegypti* males. During simulation, the wing motions are imposed symmetrically, so that, in the absence of perturbations, body motion is constrained to the longitudinal plane of the insect. The maximum wing velocity U_{max} is approximately $U_{max} = 2A_1\pi/P$, and ranges in value from 2.1 to 2.9 m/s. The wing chord is specified to be 0.46 mm, and the kinematic viscosity, $\nu = 15.7 \times 10^{-6}$ m^2/s at 300 K. Using these values, we compute Reynolds numbers ranging from 62 to 86 for the simulated insect.

5.2.2 Aerodynamics

Over the course of a single wingbeat, with the wings driven in the motion described above, the insect's body moves in response to the rigid body dynamics of the wing-body system, and in response to aerodynamic forces that are generated by the interaction of the wings and the air. At each point during the wingbeat, we use the wing velocity relative to the air to determine the drag forces that oppose wing motion and are applied in the normal direction relative to the wing plane, and the lift forces that act in the plane of the wing. To determine these forces, we use a simple quasisteady aerodynamic model:

$$F_{lift} = f_L |v_{mid}|^2 \sin 2\alpha,$$

$$F_{drag} = f_D |v_{mid}|^2 \sin^2 \alpha.$$

The structural form of this model is drawn from experimental and computational work at Reynolds numbers of 75 to 115 in [80]. $\rho = 1.18 \times 10^{-3}$ mg/mm^3 is the density of air at room temperature, $A = 0.58$ mm is the area of a single wing, v_{mid} is the wing velocity at the midpoint of the span, α is the angle of attack of the wing relative to still air, and f_L is chosen so that the insect generates sufficient lift to counter gravity when flight is simulated with the measured wingstroke. The amplitude A_1 is specified as a range because different amplitudes generate hover at different values of f_L. When $A_1 \approx 0.4$, $f_L = 3.3$. Most of this analysis was done with $f_L = 3.3$ and $A_1 \approx 0.4$. f_D is not as well constrained by measurements of insect motion and was set to 2.5.

Experimental work on aerodynamic model development has often focused on the hover case as in [20], [63], and [80]. In [82], they find good agreement between measured wing forces and a simple quasisteady model with added mass along with the inertial effects of wing motion. Simulation using TREP does include the inertial effects of wing motion. Including added mass in these inertial effects will require further tool development. In addition to matching measured forces, quasisteady models have been found to produce similar stability results to CFD for longitudinal motion ([42]). For lateral motion this is not the case. Quasisteady aerodynamic models have not been experimentally validated in the context of sideways translation of the wings, and there is evidence from computational fluid dynamics work by Zhang and Sun that the leading edge vortices that generate lift intensify on one wing and weaken on the other wing during sideways translation ([90]), which is not accounted for by standard quasisteady models. Consistent with this, Karásek and Preumont found that lateral stability results from quasisteady models do not agree with those from CFD ([42]). This inconsistency will need to be reconciled via experimental measurements of wing forces, and leaves the impact of aerodynamic forces on lateral stability an open question. Although sideways, or lateral, motion is central to the mosquito's flight repetoire (see Chapter 2), because the aerodynamic models remain unconstrained during sideways motion, we restrict

our stability analyses to the cases of hover and steady forward flight.

5.2.3 Computing periodic body motions

Using the full rigid body specifications, parameterized wing motions, and aerodynamic force model described above, we simulate the insect's motion over the course of a single wingbeat. We use the numerically robust rigid body simulation software TREP [41], which interprets the kinematic tree shown in 1 and translates it into equations of motion following rigid body techniques described in Murray, Li, and Sastry ([53]). These equations are often derived analytically ([84],[31]) and then discretized for computational integration. In TREP, the equations are found automatically using the specification of the kinematic tree, and discretization is imposed during the formation of the Lagrangian, so that the energy functional is approximate. This means that the generated equations of motion are intrinsically discrete. They can thus be integrated exactly using a computer. The aerodynamic forces are an external function of the insect's body state, and in computing solutions, we apply them at the discrete time steps we use in integrating the equations of motion. Creating the equations of motion in an automated way increases the flexibility of the system because adding or removing degrees of freedom from the wing motion, adjusting the wing position relative to the body, and changing the moment of inertia of any component of the system is straightforward.

We impose wing motions symmetrically. Of the eight body state variables that are dynamically important, four remain important in the presence of symmetric wing motion. These are pitch angle, pitch angular velocity, forward velocity, and vertical velocity. The roll angle, roll angular velocity, yaw velocity, and sideways velocity are initially set to zero and remain there due to symmetric force generation. We impose a parameterized wing motion. The body moves in response to this motion due to inertial effects and due to the aerodynamic forces generated by wing motion. For each parameterized wing motion, we identify initial conditions of the body state that create a periodic motion of the insect's

body, so that the insect returns to this same state at the end of the wingbeat. Aerodynamic forces are computed, using the quasisteady model, at each instant based on current wing velocity relative to still air.

To identify the initial conditions of the periodic orbit, we start with a guess of the appropriate initial conditions, $\mathbf{q}_0$. We compute the difference function, $\mathbf{F}(\mathbf{q}) = \mathbf{f}(\mathbf{q}) - \mathbf{q}$, where $\mathbf{f}(\mathbf{q})$ is the state of the body after a single wingbeat, given body initial conditions $\mathbf{q}$. $\mathbf{F}(\mathbf{q})$ is zero when the insect returns to the same body state at the end of the wingbeat. Identifying periodic orbits of the body motion requires finding body initial conditions that correspond to zeros of the $\mathbf{F}(\mathbf{q})$ function. To find these zeros we use Newton's method, which requires computing the Jacobian of $\mathbf{F}$, $J = \frac{\partial \mathbf{F}}{\partial \mathbf{q}}|_{\mathbf{q}_0}$. The Newton's method update step generates new initial conditions. Given current initial conditions $\mathbf{q}_n$ that are near the periodic orbit, we find new initial conditions $\mathbf{q}_{n+1} = \mathbf{q}_n - \left(\frac{\partial \mathbf{F}}{\partial \mathbf{q}}|_{\mathbf{q}_n}\right)^{-1} \mathbf{F}(\mathbf{q}_n)$. For all wing motions that we investigated, this process converged to initial conditions associated with a periodic orbit of the four body state variables, pitch, pitch velocity, forward velocity, and vertical velocity.

To compute the Jacobian, for each of the four components of the initial condition vector, q_i, we perturb the component to create new initial condition vectors $\mathbf{q} - \delta q_i \mathbf{e}_i$ and $\mathbf{q} + \delta q_i \mathbf{e}_i$, where $\mathbf{e}_i$ is the ith column vector of the 4×4 identity matrix, $\mathbb{I}_4$, and δ is small, but more than 10^2 times machine error. δ was usually set to 10^{-8} for computing the Jacobian to find periodic orbits. This creates a set of eight different initial conditions. For each of these initial conditions we integrate forward for a single wingbeat and then calculate $\mathbf{F}(\mathbf{q} \pm \delta q_i \mathbf{e}_i)$. The scaled difference $(\mathbf{F}(\mathbf{q} + \delta q_i \mathbf{e}_i) - \mathbf{F}(\mathbf{q} - \delta q_i \mathbf{e}_i))/2\delta$ is an approximation of the ith column of the Jacobian matrix.

If we are interested in identifying periodic orbits with specific mean translational velocities, such as a hover state, where the body motion is periodic in the four variables discussed above and also in forward position and vertical position, then we must generalize this method. Two more dynamically relevant degrees of freedom are necessary to generate a periodic or-

bit in six variables instead of four. Since forward and vertical position are not themselves dynamically important, we choose two of the wing parameters to act as these dynamically important variables. We select wing parameters from the stroke amplitude, A_1, the stroke offset angle, A_4, and the pitch offset angle, C_3, for this purpose. In addition, because the insect's motion can be sensitive to small variations in pitch, for some analyses we use these three wing variables along with the pitch velocity and the forward and vertical velocities as the six dynamically relevant variables for identifying a periodic orbit. In these cases, $\mathbf{q}_{body}$ is used to calculate $\mathbf{F}$ and $\mathbf{q}_{dynamic}$ is used to generate perturbed initial conditions.

5.2.4 Computing stability and identifying more stable states

For each periodic orbit we identify, the body motion is purely periodic in pitch, pitch velocity, forward velocity, and vertical velocity. In addition, the body may translate at a specified rate in the forward and vertical directions. Finally, the yaw velocity, roll, roll velocity, and sideways velocity are all fixed at zero. Given this body motion, we extend our state vector $\mathbf{q}$ to include all eight dynamically important variables, and $\mathbf{q}_{n+1} = \mathbf{q}_n + \mathbf{F}(\mathbf{q}_n)$ is the Poincare map associated with the body state. The identified periodic body motion is a fixed point in this map. To compute the stability of this fixed point we calculate the Jacobian, $J = \frac{\partial \mathbf{F}}{\partial \mathbf{q}}|_{\mathbf{q}_{fixed}}$, and find its eigenvalues and eigenvectors. We use $\delta = 10^{-5}$ for this computation. The Jacobian matrix we find is non-normal, so we compute its singular values, singular vectors, and pseudospectra. Our interest is in stability over insect-relevant timescales of ten to one hundred wingbeats, so the asymptotic stability of the system may be unimportant depending on the magnitudes of the singular values.

Once we have identified a periodic orbit and computed its corresponding eigenvalues, we search for nearby periodic orbits that are more stable. We use gradient descent to find the most stable nearby periodic motion. Leaving the target vertical velocity fixed, we perturb C_1, the pitch amplitude, C_2, the pitch phase difference, C_3, the amplitude of the $\cos 3t$ pitch term, A_2, the amplitude of the $\sin 2t$ stroke angle term, A_3, the amplitude of the

$\sin 3t$ stroke angle term, the body pitch, and the target forward velocity. We perturb the system by perturbing, one at a time, each of these parameters. The goal is to minimize the largest eigenvalue of the system. We compute the change in the largest eigenvalue as a result of the perturbation and compute the gradient of the largest eigenvalue function to find the perturbation direction of maximum increase in the eigenvalue. We adjust the seven parameters listed above in the negative gradient direction so as to drive the model insect towards a more stable periodic orbit as rapidly as possible.

We initialize these gradient descent searches at forward velocities ranging from -0.3 m/s to 0.6 m/s. In addition, we use an analogous technique to identify periodic orbits that minimize the largest singular value of the system, by replacing the largest eigenvalue with the largest singular value in the search described above.

5.3 Results

Using the gradient descent method described above, we find that the insect's periodic motions lie near the boundary of stability and instability. This result agrees with those from other analyses of insect flight ([42]). The boundary of stability and instability corresponds to high maneuverability. If the insect's flight were very stable then it might take substantial actuation to move away from a given state. If its flight were very unstable, then it would be unable to damp the growth of perturbations and control its flight. With flight that is weakly unstable, it is possible to take advantage of instability to generate changes in body motion. For example, if the insect were subject to a lateral instability that leads to increasing roll, that could potentially be used to increase the roll angle without the need for substantial direct generation of roll torque.

We think of the insect's periodic body motion over the course of the wingbeat as a limit cycle. We find the map between the insect's initial body state and its body state at the end of a single wingbeat. The maximum eigenvalue of the linearization of this map is

shown for each wing motion using red and black dots in figure 44. The maximum singular values are also shown. Eigenvalues convey information about the asymptotic growth of perturbations, whereas singular values provide a limit on the magnitude of short term growth of perturbations. In the plot on the left in figure 44, red dots correspond to real eigenvalues while black dots correspond to complex conjugate pairs. The singular values are all real. Using gradient descent we identify a wing motion associated with the smallest maximum eigenvalue at a particular forward velocity. The eigenvalue minima identified in this way are plotted using a solid magenta line in the region of asymptotic stability and a dashed magenta line in the region of asymptotic instability.

We find that forward motion is stabilizing, with the flapping insect becoming asymptotically stable for forward velocities above 0.264 m/s. At lower forward velocities, and at backward velocities, we do not find wing motions corresponding to stable body motions. We do not examine the impact of sideways velocity because aerodynamic models have limited applicability in that regime. This stability result aligns with those for a bee geometry by Xu and Sun ([85]), where they also found that forward motion was stabilizing. Across all wing motions we tested, all eigenvalues had a magnitude of less than 1.02. This is the unitless multiplicative factor by which an eigenvector will grow over the course of a single wingbeat. For comparison, Wu and Sun found maximum magnitudes of 1.05 for a dronefly geometry. Because we are examining the stability of a map, eigenvalues of less than 1 correspond to stability and values greater than 1 correspond to instability. Compared to the dronefly, the mosquito is potentially slightly closer to the stability/instability boundary. $\lambda = 1.02$ yields a doubling time of $k = 35$ wingbeats or more than 40 ms, where $\lambda^k = 2$ means that the eigenvector has doubled in length over k wingbeats. Thus the fastest growing asymptotic instabilities double on a timescale of about 35 wingbeats. In contrast, the maximum singular value associated with periodic body motions is approximately 1.765 for all wing motions examined. This corresponds to rapid growth and rotation of perturbations, since there is a perturbation that grows to 1.765 times its initial length after a single wingbeat. The lack

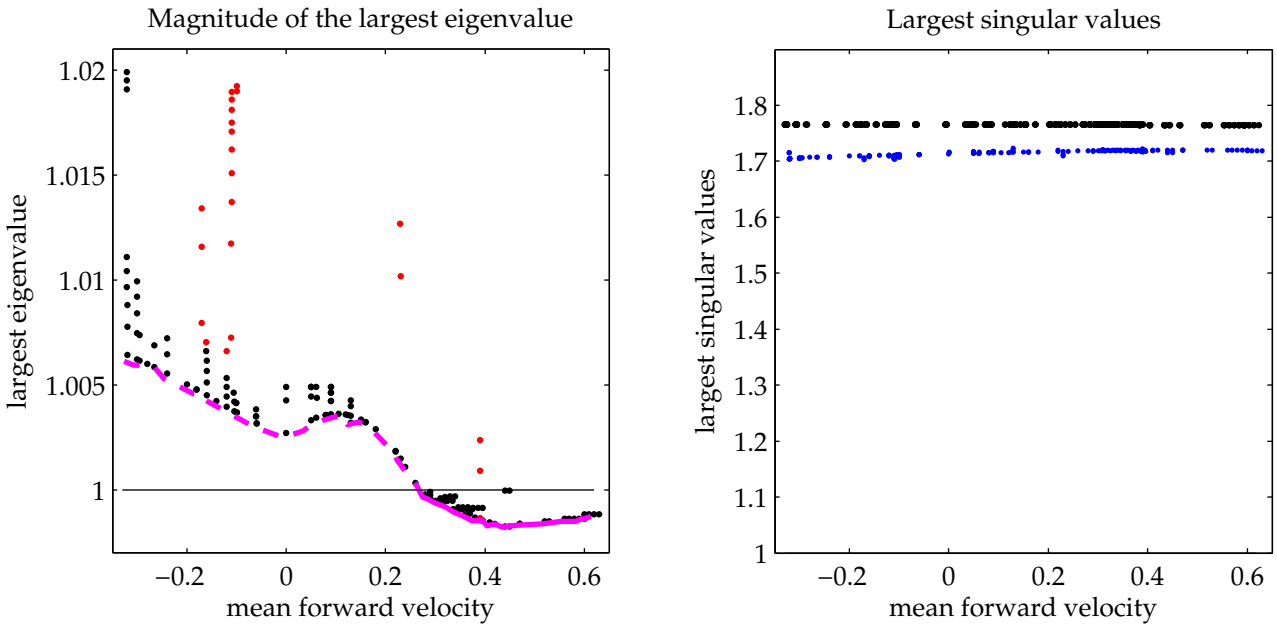

Figure 44: On the left, black and red dots correspond to particular data points while the magenta dashed and solid lines correspond to the minimum largest eigenvalue observed at a particular forward velocity. Red dots correspond to real eigenvalues and black dots to complex conjugate pairs. The system is weakly unstable for forward velocities below 0.264 m/s and is weakly stable for forward velocities above that threshold. On the right, black dots correspond to the largest singular value associated with a given wing motion, plotted against forward velocity. These always correspond to a longitudinal singular vector. Blue dots correspond to the second largest singular value, and a latitudinal singular vector. There is very little variation in the largest singular values, even as the system transitions from asymptotically unstable to asymptotically stable.

of variation in the singular value over a range of forward velocities and wing motions may indicate that the non-normality of the system is a result of the flapping geometry. To examine this, we turn down gravity and the aerodynamic forces in tandem so that inertial forces become much more important. The singular value decreases slightly but remains about 1.7 even as gravity and aerodynamic forces are less than 5 percent of their initial values. The lack of change with changing aerodynamic forces makes it likely that inertial considerations are responsible for the high singular values.

The imposition of symmetric wing motion fully decouples lateral motions such as yaw and roll from longitudinal ones such as pitch. The geometry of the insect precludes further

decoupling, however. Wing torques are applied along directions that do not correspond to the principal axes of the mosquito's body. This creates an intrinsic coupling between yaw, roll, and sideways motion. Roll velocity is also a component of lateral motion. In the longitudinal case, changing the body pitch angle adjusts both the forward velocity and the vertical velocity. In addition, different wing pitch sequences during the wingstroke drive a changes in the corresponding oppositional body pitch motion due to conservation of momentum, as well as in the forward and vertical velocities. Pitch velocity is the fourth component of longitudinal motion.

Four eigenvalues of the Jacobian matrix correspond to eigenvectors in longitudinal directions and four to eigenvectors in lateral directions. The magnitudes of the largest lateral and longitudinal eigenvectors are shown in figure 45. Red dots correspond to real eigenvalues and black to complex conjugate pairs. At almost all velocities, the insect is either unstable or stable with respect to both lateral and longitudinal perturbations. Transition to stability occurs at a slightly lower forward velocity for the lateral modes, but the difference is small. In the lateral direction, the most unstable mode is almost always an oscillatory mode. In the longitudinal direction, real eigenvalues do appear at high forward velocities and at negative forward velocities, but at intermediate velocities the most unstable mode is oscillatory. At all times there is a singular value of about 1.765 associated with a longitudinal singular vector. There is also always a singular value of greater than 1.700 associated with a lateral singular vector.

When we examine timescales longer than one wingbeat, we consider the matrix A^k where A is the linearized map for a single wingbeat and k is the number of wingbeats. For $k > 1$, the largest longitudinal singular value grows from 1.765. It increases linearly in the number of wingbeats for about fifty wingbeats, or 60 ms. It grows with a mean increase of 1.1 in the longitudinal singular value per wingbeat across all flights. The slope computed using fifty wingbeats has a standard devation of 0.1 across all wing motions. Even for stable systems, the singular value continues to increase for about eighty wingbeats before the long time

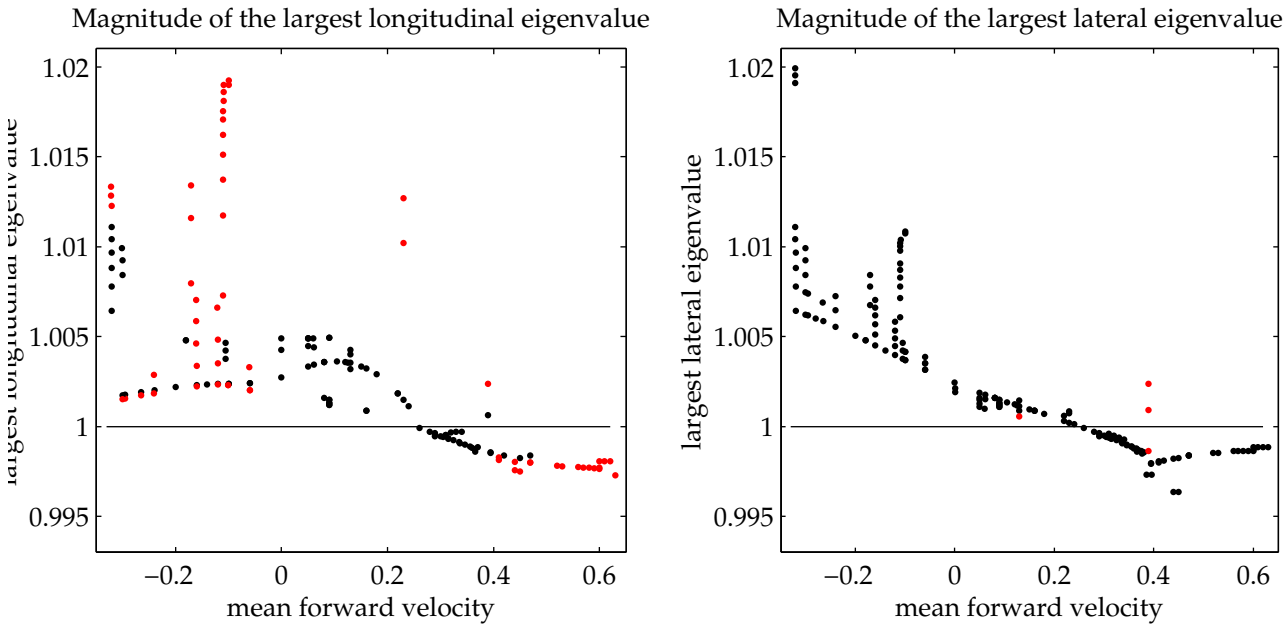

Figure 45: In the figure on the left, dots correspond to the magnitude of the largest eigenvalue associated with an eigenvector in a longitudinal direction. On the right they correspond to the magnitude of the largest eigenvalue associated with an eigenvector in a lateral direction. Lateral motion includes changes in roll, roll velocity, yaw velocity, and lateral velocity, while longitudinal motion involves changes in pitch, pitch velocity, forward velocity, or vertical velocity. Black dots correspond to eigenvalues that are part of a complex conjugate pair while red dots represent real eigenvalues. The minimization routine operated on the largest eigenvalue. For velocities above zero, this was often an eigenvalue associated with longitudinal motion, so the lateral values are not minimized in this case.

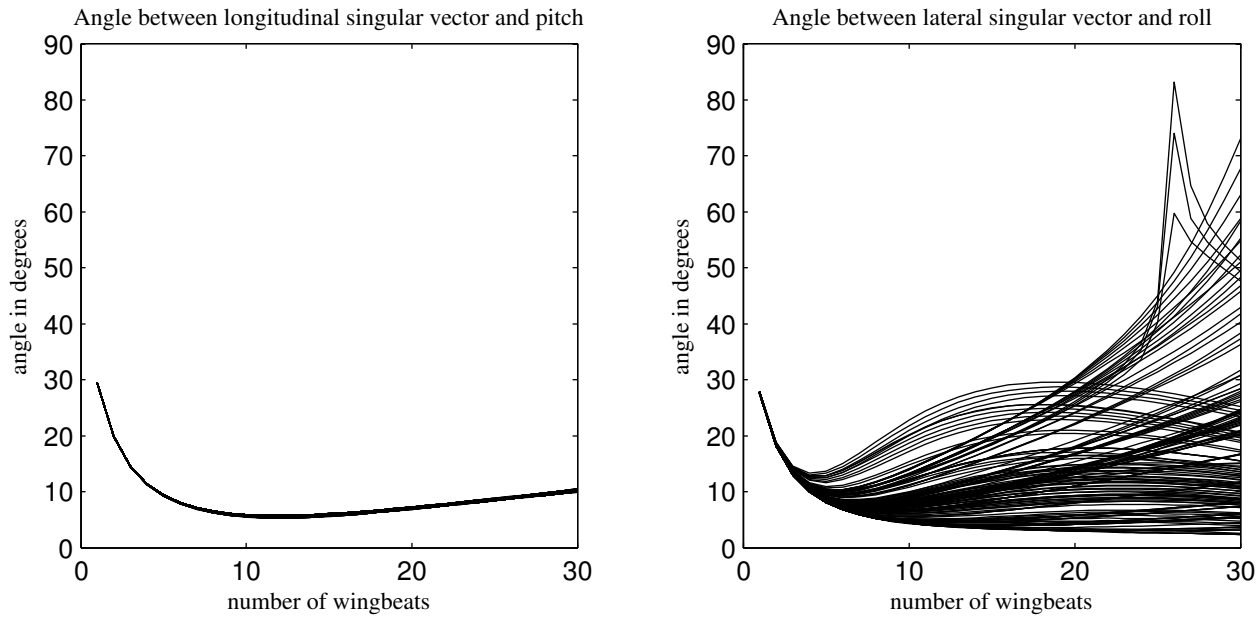

Figure 46: On the left, lines show the angle between the most unstable longitudinal singular vector and a pure pitch perturbation as a function of the number of wingbeats. On the right, lines show the angle between the most unstable lateral singular vector and a pure roll perturbation as a function of the number of wingbeats. These are computed by identifying the largest singular values, and their corresponding vectors, for J^k, where J is the Jacobian matrix associated with a particular wing motion, and k is the number of wingbeats. Given the singular vectors corresponding to the largest singular values, we find the angle between the vector and a pure pitch or roll perturbation. Each line in the graphs corresponds to a different wing motion. The fastest growing longitudinal perturbation becomes well aligned with a pure pitch mode within 8 wingbeats. In addition, it is consistent across all wing motions that we examine, resulting in the appearance of a single line in the graph. In contrast, there is substantial variation in the fastest growing lateral perturbation with wingbeat.

exponential decay begins to dominate.

The other longitudinal singular values are less than one, so all longitudinal perturbations will be stretched and rotated to align with the direction of the singular vector corresponding to the largest singular value. The angle between this vector and a pure pitch perturbation is shown as a function of the number of wingbeats on the left in figure 46. Each black line corresponds to the angular information for a different wing motion. The vector does not initially align with a pitch perturbation but is quickly rotated into better alignment. Between ten and fourteen wingbeats, these vectors are within six degrees of a pure pitch

mode for all wing motions examined. This uniformity in the evolution of perturbations across a range of wing motions may be advantageous for the insect. By the time a control is applied to a sensed perturbation, 5 to 40 wingbeats later, the perturbation has rotated towards alignment with the direction of the singular vector, and is thus to more aligned with a pure pitch perturbation. This could simplify the control system of the insect, because an arbitrary perturbation is passively transformed to fall within a small range of directions and the insect may only need to operate controls for that small range.

On the right of figure 46, the angle between the most unstable lateral singular vector and a pure roll mode is shown as a function of the number of wingbeats. There is much more variation in the lateral behavior between different wing motions of the insect. Initially, all of the singular vectors are rotated to better align with the roll direction. However their behavior quickly diverges and there is no consistent pattern. For the lateral singular value, the growth of the singular value is sublinear in all cases for the first forty wingbeats, so lateral perturbations do not grow as quickly as longitudinal perturbations. The wide variation in singular vectors with wing motion may make lateral control more complex than longitudinal control. At the same time, perturbations do not grow as fast laterally. Also, although the insect's roll angle is maintained within -15 degrees to 15 degrees at almost all times (see Chapter 3), changes in the yaw angle do not have much impact on the insect's flight so perturbations that impact the yaw angle may not need to be rapidly controlled.

When a matrix is non-normal there is the possibility that small perturbations in the matrix will lead to large changes in the eigenvalues. The pseudospectra of the Jacobian, for eight different forward velocities, are shown in figure 47. The contour lines of the pseudospectra show how much the eigenvalues change with small perturbations of the Jacobian matrix. The eigenvalues are plotted as small black dots, surrounded by contourlines that indicate level boundaries of sets $\{z \in \mathbb{C} : \|(A - zI)\mathbf{x}\| \leq \epsilon \text{ for some } \mathbf{x} \in \mathbb{C}^8 \text{ with } \|\mathbf{x}\| = 1\}$ ([73], [83]). In these plots, values of ϵ range from $10^{-4.75}$ to $10^{-2.5}$ in increments of 0.25 in the exponent. The unit circle is shown as a thin gray line. For each matrix, whether or

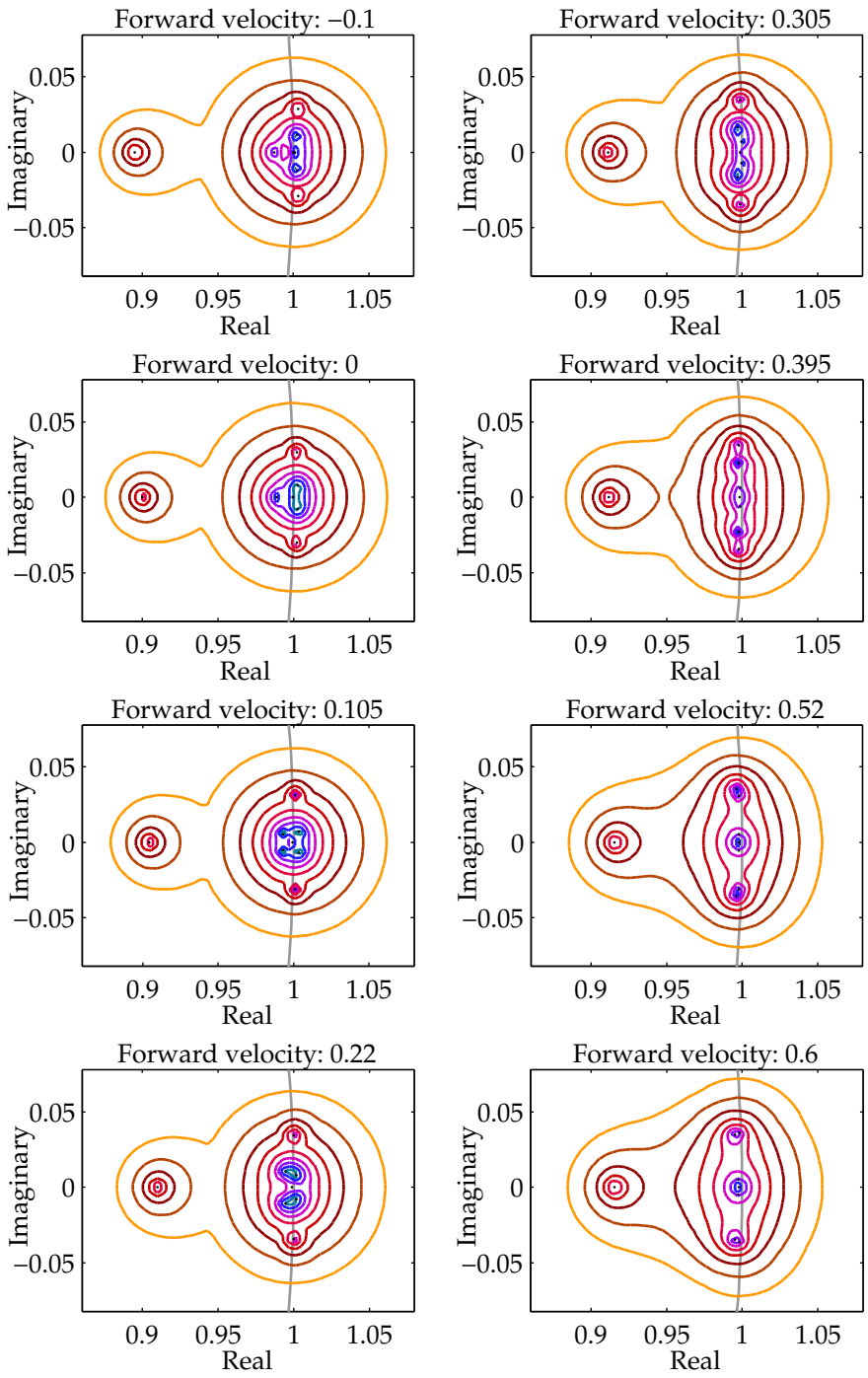

Figure 47: The pseudospectra are shown for eight different forward velocities, where the Jacobian matrices used are drawn from ones that lie on the pink line in figure 44. The eigenvalues are represented in the real-imaginary plane as black dots. Each matrix has eight corresponding eigenvalues. Contourlines are lines delineating the z where $\|(A - zI)\mathbf{x}\| \leq \epsilon$ for fixed ϵ. The inequality is satisfied when, for a given value of z, there is an arbitrary unit vector $\mathbf{x}$ for which the expression holds. The outermost contours correspond to $\epsilon = 10^{-2.5}$ while the innermost to $\epsilon = 10^{-4.75}$, with contours are plotted at increments of 0.25 in the exponent. For matrices that are non-normal, like these, the contours deviate from circles ([73]). The unit circle is a thin gray line that crosses each plot near one.

not it corresponds to an asymptotically stable system, the contour where $\epsilon = 10^{-3.75}$, which is a magenta line, crosses the unit circle. For all wing motions we examine there are thus nearby body evolution matrices with different asymptotic stability. Whether we find the insect's motion to be passively stable or weakly unstable, in all cases its motion is close to the boundary between stability and instability, so after a long time, perturbations will grow or decay slowly. At larger forward velocities, many of the eigenvalues are constrained to a narrow region near the unit circle. When we perturb the map describing the evolution of the body state under a given wing motion, we find that the imaginary parts of the eigenvalues may change substantially but the matrix remains along the stability boundary. Thus the degree of oscillation in the oscillatory instabilities varies, but the basic stability landscape does not.

5.4 Discussion

We find that the mosquito flight system is asymptotically stable, while remaining close to metastable, at high forward velocities, and is unstable, but close to metastable, at lower forward velocities. The insect is unstable both to longitudinal and to lateral perturbations at low velocities and is stable to both types of perturbations at higher velocities. This asymptotic stability result implies that perturbations will decay or will grow slowly when examined after a long time. The short term growth of instabilities is governed by the largest singular values of the matrix. The matrix describing the insect's linearized motion is non-normal, with two singular values much larger than 1. These large singular values correspond to two faster growing short-term instabilities, one in the longitudinal and one in the lateral direction. Over timescales of up to 100 ms, instead of observing the slow growth or decay of perturbations, as we would if the matrix were normal, there is instead the potential for substantial perturbation growth driven by these large singular values.

The analysis timescale we are interested in for the insect system is its control timescale.

From empirical observations, we know that mosquitoes are able to fly, and are highly maneuverable insects, so we expect them to be metastable with slowly growing or slowly decaying perturbations. The halteres and the visual system, which provide feedback for flight control, give feedback to flight muscles with 50 ms of perception ([62], [81]). Within this same period, non-normality contributes to transient perturbation growth. Without the presence of non-normality, mosquito flight appears to usually require only slow control. Perturbations grow on approximately the same timescale as timescale of sensory feedback and the most unstable mode is usually oscillatory. For body pitch and body yaw, flight can occur at a range of values. For body yaw, we observe oscillations which are sometimes present and occur over tens of milliseconds with amplitudes of a few degrees (see Chapter 2). These oscillations may be actively generated, or they may be a sign of instability that is not tightly controlled. Body roll may require more exacting control because it is important to determining flight direction (see Chapter 3). However, oscillations of a few degrees in the roll angle, where roll angles reach 15 or even 20 degrees during maneuvers, would not necessarily disrupt flight control.

With non-normality, as we find here, there are some perturbations that grow rapidly, rather than all perturbations growing at a rate controllable by the visual system. A perturbation imposed at time zero can rotate and grow between the time it is sensed and the time at which the insect will utilize a control to impose a correction. In the longitudinal case, because the singular vector corresponding to the largest singular value is similar across all wing motions we examine, this may alter the control problem the insect faces by reducing the space of controls that would need to be applied. Instead of having a variety of controls to address a range of sensed instabilities, the insect may actually encounter only a small family of perturbations by the time it imposes a new wing motion. If a gust perturbs its forward velocity, vertical velocity, or pitch velocity, these perturbations evolve towards a perturbation with a large pitch component. The lateral stability picture is more complicated because there are a range of singular vectors, each associated with the largest singular value

of different wing motions. Instead of perturbations evolving similarly over time regardless of current wing motion, the evolution of perturbations depends on the current wing motion. Nonetheless, if a control is applied within 20 wingbeats, or 25 ms, the fastest growing perturbations remain within about 30 degrees of a pure roll perturbation.

The presence of non-normality may be due to the structure of the rigid body system. A singular value of 1.61 is associated with flapping flight in droneflies ([84]), and the maximum singular value changes substantially when flappng is neglected. We find that turning down aerodynamic forces and gravity to less than 5 percent of their normal values creates little change in the singular values, another indicator that they are a result of inertial interactions between the wings and body. The motion of the wing drives changes in body pitch on the sub-wingbeat timescale, even in the absence of aerodynamic forces, and even though these changes are small for the small wingstroke of a mosquito, they may be the source of non-normality. Rotational body friction, which was not included in this computational model, might provide damping that could potentially alter the system. Understanding the source and consequences of non-normality in this system remains an important open question.

Chapter 6

Conclusions

Using motion capture data for hundreds of mosquito flights, we work towards characterizing mosquito flight. We find a number of differences between the flight of mosquitoes and that of other commonly studied Dipterans. For example, mosquitoes have a very short stroke amplitude compared to those recorded for other insects, and they fly with a sideways component to their flight more frequently than other Dipterans. Even hoverflies, which are well known to use sideslip, fly forward more frequently than mosquitoes do ([32], [12]). This makes it difficult to predict mosquito orientation from flight direction information alone. Like fruitflies ([70]), mosquitoes interrupt their flights with many changes in flight direction. Unlike fruitflies, mosquitoes actuate most of these directional changes via sideslipping turns, with yaw turns occurring less frequently. Mosquitoes also change their yaw direction without changing their flight direction, a type of turn seen in hoverflies ([12]) as well.

Sideways acceleration is an important component of mosquito flight. It drives sideslip based turns, and is thus central to mosquito directional changes. Sideways acceleration also often occurs during non-turning flight. When acceleration information is averaged over multiple wingbeats, the direction of time-averaged acceleration relative to the insect's body yaw direction is approximately evenly distributed. It has long been thought that sideways acceleration is roll driven ([77]) although other mechanisms of sideways thrust generation are

known in fruitflies ([59], [68]) and blowflies ([2]). For mosquitoes, we find good quantitative agreement between roll driven tilt of the insect's lift vector and measured sideways thrust. In particular, roll driven thrust is the dominant component of sideways thrust generation in almost all flights.

A similar tilt-based mechanism, where forward acceleration is generated by pitching of the lift vector, has been found to dominate forward acceleration generation in fruitflies ([50]) and has long been known to be important to thrust generation in these insects ([76], [14]). At the same time, other forward thrust generation mechanisms are known to exist in fruitflies ([58]) and in houseflies ([77]). For mosquitoes, in contrast, pitch driven thrust makes a dominant contribution to the total thrust in less than one quarter of flights. Instead, there are multiple wing motions that are associated with forward thrust generation.

For example, after the wing flips, the wing continues to rotate, reaching a low angle of attack before returning to a slightly higher angle for the bulk of the wingstroke. Often, after the wing flip, the wing will rotate until it is almost parallel to the stroke plane. At other times, it only rotates to just below 45 degrees. When a large rotation occurs at the beginning of the downstroke, and a smaller rotation at the beginning of the upstroke, there is an asymmetry in the post-wing flip rotation. This asymmetry corresponds to reduced drag during the downstroke relative to the upstroke and is thus associated with a net forward thrust. This asymmetry appears in both wings simultaneously, so is used for thrust generation, and may contribute a net body pitching moment, but likely does not directly drive changes in roll or yaw.

Another wing motion asymmetry that corresponds to longitudinal thrust is a timing change in the time of the wing flip relative to the time when the leading edge of the wing changes direction. Although the leading edge of the wing moves symmetrically, the wing often flips with delay as the wing moves towards the head, or flips in advance as the wing moves away from the head. Delayed or advanced wing flips cause associated peaks in the lift and drag forces ([63], [20], [80]). According to measurements by Sane and Dickinson, delay

at the end of the downstroke causes extra drag during the upstroke and advancement at the end of the upstroke also causes extra drag during the upstroke, so there is a mechanistic explanation for forward thrust generation associated with these timing variations.

Along with thrust generation mechanisms, we examine other aspects of mosquito wing motion. We find that *Aedes aegypti* males have a wingbeat frequency of 800 Hz, with typical variation within a flight of about 20 Hz. We observed one flight where the wingbeat frequency of the insect changed by over 100 Hz in under 100 ms of flight, and one flight where the wingbeat frequency of the insect reached 1100 Hz. We did not find a strong relationship between the wingbeat frequency and acceleration or velocity. Wingbeat frequency is sometimes adjusted as mosquitoes approach a mate ([9]), so little or no association between wingbeat frequency and acceleration may mean that the insect is able to adjust its wingbeat frequency without substantially altering its flight forces.

With a wingbeat frequency of 800 Hz, these mosquitoes are flapping much faster than other studied Dipterans ([24]). At the same time, they have an extraordinarily short stroke amplitude. The angle subtended by a wing over the course of a wingbeat has a mean of 42 degrees. In contrast, most Brachycerans subtend angles of more than 100 degrees, although hoverfly stroke amplitudes have been found to be as small as 66 degrees. In fruitflies and blowflies, there can be substantial asymmetries in stroke angle between the two wings ([2], [29]). In hoverflies ([78]), and in mosquitoes, these large variations are not observed.

Along with a short stroke amplitude, mosquitoes have at most a short phase of pure translation during the wingbeat, and in many wing strokes they exhibit continuous wing rotation with no translational phase. Altshuler et al found that changes in the speed of wing rotation cause substantial changes in flight forces ([1]). The speed of wing rotation before the wing flip varies in mosquitoes, with slower rotation occurring when translation is absent. Wing rotation just after the stroke flip, as the wing moves from vertical to closer to horizontal, is always rapid.

In addition to thrust generation, which results from asymmetries between the downstroke

and the upstroke, wing asymmetries can drive torque generation. Yaw and roll moments require asymmetries between the two wings, while pitch moments can result when the portion of the wingbeat that occurs forward of the center of mass generates torques that are not balanced by the portion of the wingbeat occurring behind the center of mass. The center of the wing stroke is set back about 6 degrees from perpendicular to the yaw direction. This backward offset is likely related to balancing pitch moment generation throughout the stroke, since the abdomen is behind the wing attachment point and this may shift the center of mass backwards from the thorax. The shifts in wing flip timing, as well as the asymmetry in wing rotation discussed above, likely play a role in pitch moment generation as well as in forward thrust generation. Using simulation, we find that the insect is weakly unstable to pitch perturbations when its forward velocity is below 0.26 m/s, and the singular value associated with longitudinal perturbations is 1.76. This corresponds to substantial instability growth, so the insect likely applies counter-torques on some timescale to maintain its pitch angle within an acceptable range.

Asymmetries between the two wings can generate roll or yaw torques. We observe many such asymmetries. Wing flip advancement or delay can occur in one wing and not the other. In addition, a translational phase to the stroke may appear in just a single wing. Both of these are associated with asymmetries in wing pitch angle between the two wings, and pitch angle asymmetries have been found to drive body rotation in fruitflies ([5]). Asymmetries in the wing flip also directly change the timing of lift and drag forces so may drive body rotation independent of their influence on the wing pitch angle. Experiments measuring wing forces at Reynolds numbers relevant to mosquitoes, with rotational and translational timing that apply to mosquito motion, remain to be done. Without experimental data validating quasisteady models in the mosquito regime, it is difficult to determine which mechanism of torque generation is dominant. In addition, quasisteady models are not validated in the presence of lateral translation, a phenomenon that is central to mosquito flight and is particularly important during turning maneuvers. During lateral translation, quasisteady

models and CFD lead to different stability results ([42]) so quasisteady models offer less insight in that situation.

Body pitch and body yaw do not have clear dynamic importance in mosquitoes. Mosquitoes fly with their body yaw oriented at a range of angles relative to their flight direction, and their body pitch is not a dominant mechanism for thrust generation, so likely has a wide range of acceptable values. In contrast, the roll angle is directly linked to sideways acceleration and thus to the generation of directional changes during flight. Although quasisteady models provide us with limited insight into lateral stability, using simulation we find that the insect is unstable to lateral perturbations at low and moderate forward velocities. If the insect is unstable to lateral perturbations, roll could be generated passively, and then controlled by the generation of torques, rather than directly generated. In addition, roll and yaw are correlated in mosquitoes. This may be because some controls, such as wing flip timing, likely actuate both yaw and roll by changing both lift and drag forces. Other mechanisms, such as a pitch asymmetry at midstroke, have a larger impact on wing drag forces than on lift forces. This is because, for a wing angle near 45 degrees, lift production is near the peak of a quadratic as the angle changes, while drag production changes linearly with the angle change so changes more rapidly. Thus some controls may couple yaw and roll while others are potentially decoupled. Since some changes in wing motion likely generate both roll and yaw torques, it is potentially the case that some yaw rotation occurs as a side effect of controlled changes in roll.

Detecting the difference between passive and active generation of roll or yaw as well as identifying potential aspects of the wing motion that serve as controls will require coupling simulation and wing kinematic measurements with aerodynamic models that have been specifically developed for application to lateral motion. Open questions in this area include identifying whether the yaw angle is actively set, or whether it is maintained within an acceptable range. In measurements of body yaw angle, we observe small yaw oscillations that occur over tens of milliseconds. They are on a timescale consistent with oscillatory instabil-

ity, so they may be a sign of slow control of instabilities, or they may be actively generated for some sensory or stability purpose. Their source and importance are currently unknown.

Another open question related to understanding roll is the contribution of wing drag to the roll dynamics. The moment of inertia of mosquitoes is low about the roll axis in comparison to the pitch and yaw axes. This could lead to a need for fine control of torque to maintain roll within the limits that we observe. Mosquito roll rarely exceeds 15 degrees, and changes in roll occurs no more rapidly than rotation about other axes. For yaw turns, recent work has found that the wings contribute substantial drag, with this drag dwarfing the inertial contribution of the body ([38]). In cockatoos, drag during roll appears to provide limits on the motion ([37]). If wing effects dominate in mosquitoes then the low body moment of inertia would be less important and roll and yaw dynamics would be similar despite the large difference in moment of inertia.

In addition to generating a number of questions about mosquito motion and control, the experimental techniques we use make it possible to capture flights of male mosquitoes that are stimulated by the motion of females. We are able to capture footage of males approaching females, connecting with females, flying in tandem with females, and mating with females. These techniques could be used to examine and characterize the process of a male finding a female during free flight.

To go beyond experiment, we use simulation to delve into mosquito flight stability. Our main finding is that non-normality is present in the linearized system that describes how the mosquito's body state evolves during each wingbeat. This non-normality corresponds to large singular values, which means that there are perturbations to the insect's body state that will grow rapidly. However, as these perturbations grow they also change direction so that a perturbation in forward velocity evolves into a perturbation in body pitch angle. This rotation of perturbations, which occurs on timescales of just a few wingbeats, could potentially simplify the control problem faced by mosquitoes to requiring a single controller for longitudinal stability across a wide range of wing motions and many different directions

of perturbation. The lateral control picture may be more complicated, but it is also an area where the quasisteady aerodynamic model we use is more limited. Further work is needed in understanding the lateral stability and control in mosquitoes because this is their main flight control. The development of validated aerodynamic models would be an important first step in this area.

Bibliography

[1] Douglas L. Altshuler, William B. Dickson, Jason T. Vance, Stephen P. Roberts, and Michael H. Dickinson. Short-amplitude high-frequency wing strokes determine the aerodynamics of honeybee flight. *Proceedings of the National Academy of Sciences of the United States of America*, 102(50):18213–18218, 2005.

[2] Claire N. Balint and Michael H. Dickinson. Neuromuscular control of aerodynamic forces and moments in the blowfly, *Calliphora vicina*. *Journal of Experimental Biology*, 207(22):3813–3838, 2004.

[3] J Beeuwkes, J Spitzen, CW Spoor, JL Van Leeuwen, and W Takken. 3-d flight behaviour of the malaria mosquito anopheles gambiae ss inside an odour plume. *Proc Neth Entomol Soc Meet*, 19:137–146, 2008.

[4] John A. Bender and Michael H. Dickinson. Visual stimulation of saccades in magnetically tethered drosophila. *The Journal of Experimental Biology*, 209(16):3170–3182, 2006.

[5] Attila J. Bergou, Leif Ristroph, John Guckenheimer, Itai Cohen, and Z. Jane Wang. Fruit flies modulate passive wing pitching to generate in-flight turns. *Phys. Rev. Lett.*, 104:148101, Apr 2010.

[6] Norbert Boeddeker and Jan M. Hemmi. Visual gaze control during peering flight manoeuvres in honeybees. *Proceedings of the Royal Society B: Biological Sciences*, 277(1685):1209–1217, 2010.

[7] William G. Brogdon. Measurement of flight tone differences between female *Aedes aegypti* and *A. albopictus* (diptera: Culicidae). *Journal of Medical Entomology*, 31(5):700–703, 1994.

[8] Sachit Butail, Nicholas C Manoukis, Moussa Diallo, José MC Ribeiro, and Derek A Paley. The dance of male anopheles gambiae in wild mating swarms. *Journal of Medical Entomology*, 50(3):552–559, 2013.

[9] Lauren J. Cator, Ben J. Arthur, Laura C. Harrington, and Ronald R. Hoy. Harmonic convergence in the love songs of the dengue vector mosquito. *Science*, 323(5917):1077–1079, 2009.

[10] B. Cheng, S. N. Fry, Q. Huang, and X. Deng. Aerodynamic damping during rapid flight maneuvers in the fruit fly drosophila. *The Journal of Experimental Biology*, 213(4):602–612, 2010.

[11] A.N. Clements. *The Biology of Mosquitoes: Sensory reception and behaviour*. The Biology of Mosquitoes. Chapman & Hall, 1999.

[12] TS Collett and MF Land. Visual control of flight behaviour in the hoverflysyritta pipiens l. *Journal of Comparative Physiology*, 99(1):1–66, 1975.

[13] Stacey A Combes and Robert Dudley. Turbulence-driven instabilities limit insect flight performance. *Proceedings of the National Academy of Sciences*, 106(22):9105–9108, 2009.

[14] C. T. David. The relationship between body angle and flight speed in free-flying drosophila. *Physiological Entomology*, 3(3):191–195, 1978.

[15] R De Jong and BGJ Knols. Selection of biting sites on man by two malaria mosquito species. *Experientia*, 51(1):80–84, 1995.

[16] Andrew K Dickerson, Peter G Shankles, Nihar M Madhavan, and David L Hu. Mosquitoes survive raindrop collisions by virtue of their low mass. *Proceedings of the National Academy of Sciences*, 109(25):9822–9827, 2012.

[17] M H Dickinson and K G Götz. The wake dynamics and flight forces of the fruit fly *Drosophila melanogaster*. *Journal of Experimental Biology*, 199(9):2085–104, 1996.

[18] M. H. Dickinson, F. O. Lehmann, and K. G. Götz. The active control of wing rotation by *Drosophila*. *Journal of Experimental Biology*, 182(1):173–189, 1993.

[19] Michael H. Dickinson. The initiation and control of rapid flight maneuvers in fruit flies. *Integrative and Comparative Biology*, 45(2):274–281, 2005.

[20] Michael H. Dickinson, Fritz-Olaf Lehmann, and Sanjay P. Sane. Wing rotation and the aerodynamic basis of insect flight. *Science*, 284(5422):1954–1960, 1999.

[21] William B. Dickson, Peter Polidoro, Melissa M. Tanner, and Michael H. Dickinson. A linear systems analysis of the yaw dynamics of a dynamically scaled insect model. *The Journal of Experimental Biology*, 213(17):3047–3061, 2010.

[22] JA Downes. The swarming and mating flight of diptera. *Annual review of entomology*, 14(1):271–298, 1969.

[23] R. Dudley and C. P. Ellington. Mechanics of forward flight in bumblebees: I. kinematics and morphology. *Journal of Experimental Biology*, 148(1):19–52, 1990.

[24] C. P. Ellington. The aerodynamics of hovering insect flight. iii. kinematics. *Philosophical Transactions of the Royal Society of London. Series B, Biological Sciences*, 305(1122):pp. 41–78, 1984.

[25] CP Ellington. The aerodynamics of hovering insect flight. iv. aeorodynamic mechanisms. *Philosophical Transactions of the Royal Society of London. B, Biological Sciences*, 305(1122):79–113, 1984.

[26] A. Roland Ennos. The kinematics and aerodynamics of the free flight of some diptera. *Journal of Experimental Biology*, 142(1):49–85, 1989.

[27] Imraan Faruque and J Sean Humbert. Dipteran insect flight dynamics. part 1 longitudinal motion about hover. *Journal of Theoretical Biology*, 264(2):538–552, 2010.

[28] Imraan Faruque and J Sean Humbert. Dipteran insect flight dynamics. part 2: Lateral–directional motion about hover. *Journal of Theoretical Biology*, 265(3):306–313, 2010.

[29] Steven N Fry, Rosalyn Sayaman, and Michael H Dickinson. The aerodynamics of free-flight maneuvers in *Drosophila*. *Science*, 300(5618):495–498, 2003.

[30] Steven N. Fry, Rosalyn Sayaman, and Michael H. Dickinson. The aerodynamics of hovering flight in *Drosophila*. *Journal of Experimental Biology*, 208(12):2303–2318, 2005.

[31] Na Gao, Hikaru Aono, and Hao Liu. Perturbation analysis of 6dof flight dynamics and passive dynamic stability of hovering fruit fly¡ i¿ drosophila melanogaster¡/i¿. *Journal of Theoretical Biology*, 270(1):98–111, 2011.

[32] Bart R. H. Geurten, Roland Kern, Elke Braun, and Martin Egelhaaf. A syntax of hoverfly flight prototypes. *The Journal of Experimental Biology*, 213(14):2461–2475, 2010.

[33] Karl Georg Götz. Flight control in *Drosophila* by visual perception of motion. *Kybernetik*, 4(6):199–208, 1968.

[34] Karl Georg Götz, Bärbel Hengstenberg, and Roland Biesinger. Optomotor control of wing beat and body posture in drosophila. *Biological Cybernetics*, 35(2):101–112, 1979.

[35] Duane J Gubler. The global emergence/resurgence of arboviral diseases as public health problems. *Archives of medical research*, 33(4):330–342, 2002.

[36] J.H. Hateren and C. Schilstra. Blowfly flight and optic flow. ii. head movements during flight. *Journal of Experimental Biology*, 202(11):1491–1500, 1999.

[37] T. L. Hedrick, J. R. Usherwood, and A. A. Biewener. Low speed maneuvering flight of the rose-breasted cockatoo (*Eolophus roseicapillus*). ii. inertial and aerodynamic reorientation. *Journal of Experimental Biology*, 210(11):1912–1924, 2007.

[38] Thomas Hesselberg and Fritz-Olaf Lehmann. Turning behaviour depends on frictional damping in the fruit fly *Drosophila*. *Journal of Experimental Biology*, 210(24):4319–4334, 2007.

[39] Thomas Hesselberg and Fritz-Olaf Lehmann. The role of experience in flight behaviour of *Drosophila*. *Journal of Experimental Biology*, 212(20):3377–3386, 2009.

[40] Daisuke Ishihara, T. Horie, and Mitsunori Denda. A two-dimensional computational study on the fluidstructure interaction cause of wing pitch changes in dipteran flapping flight. *Journal of Experimental Biology*, 212(1):1–10, 2009.

[41] Elliot R Johnson and Todd D Murphey. Scalable variational integrators for constrained mechanical systems in generalized coordinates. *Robotics, IEEE Transactions on*, 25(6):1249–1261, 2009.

[42] Matěj Karásek and André Preumont. Flapping flight stability in hover: A comparison of various aerodynamic models. *International Journal of Micro Air Vehicles*, 4(3):203–226, 2012.

[43] John S Kennedy. The visual responses of flying mosquitoes. *Proceedings of the Zoological Society of London*, 109(4):221–242, 1940.

[44] Roland Kern, Norbert Boeddeker, Laura Dittmar, and Martin Egelhaaf. Blowfly flight characteristics are shaped by environmental features and controlled by optic flow information. *The Journal of Experimental Biology*, 215(14):2501–2514, 2012.

[45] Daniel L Kline. Traps and trapping techniques for adult mosquito control. *Journal of the American Mosquito Control Association*, 22(3):490–496, 2006.

[46] XQ Kong and CW Wu. Mosquito proboscis: An elegant biomicroelectromechanical system. *Physical Review E*, 82(1):011910, 2010.

[47] M.F. Land and T.S. Collett. Chasing behaviour of houseflies (fannia canicularis). *Journal of comparative physiology*, 89(4):331–357, 1974.

[48] F.O. Lehmann and M.H. Dickinson. The production of elevated flight force compromises manoeuvrability in the fruit fly *Drosophila melanogaster*. *Journal of Experimental Biology*, 204(4):627–635, 2001.

[49] Yanpeng Liu and Mao Sun. Wing kinematics measurement and aerodynamics of hovering droneflies. *Journal of Experimental Biology*, 211(13):2014–2025, 2008.

[50] V. Medici and S. N. Fry. Embodied linearity of speed control in *Drosophila melanogaster*. *Journal of The Royal Society Interface*, 9(77):3260–3267, 2012.

[51] Aubrey Moore, James R. Miller, Bruce E. Tabashnik, and Stuart H. Gage. Automated identification of flying insects by analysis of wingbeat frequencies. *Journal of Economic Entomology*, 79(6):1703–1706, 1986.

[52] Markus Mronz and Fritz-Olaf Lehmann. The free-flight response of drosophila to motion of the visual environment. *Journal of Experimental Biology*, 211(13):2026–2045, 2008.

[53] Richard Murray, ZX Li, and S Shankar Sastry. A mathematical introduction to robotic manipulation. *Florida: CRC Press, Inc*, 1994.

[54] Werner Nachtigall and Werner Roth. Correlations between stationary measurable parameters of wing movement and aerodynamic force production in the blowfly (*Calliphora vicina R.-D.*). *Journal of comparative physiology*, 150(2):251–260, 1983.

[55] Gerbera Nalbach. The gear change mechanism of the blowfly (calliphora erythrocephala) in tethered flight. *Journal of Comparative Physiology A*, 165(3):321–331, 1989.

[56] Christopher T Orlowski and Anouck R Girard. Dynamics, stability, and control analyses of flapping wing micro-air vehicles. *Progress in Aerospace Sciences*, 51:18–30, 2012.

[57] J James O Ramsay, Giles Hooker, and Spencer Graves. *Functional data analysis with R and MATLAB*. Springer, 2009.

[58] Leif Ristroph, Attila J. Bergou, John Guckenheimer, Z. Jane Wang, and Itai Cohen. Paddling mode of forward flight in insects. *Phys. Rev. Lett.*, 106:178103, Apr 2011.

[59] Leif Ristroph, Gordon J Berman, Attila J Bergou, Z Jane Wang, and Itai Cohen. Automated hull reconstruction motion tracking (hrmt) applied to sideways maneuvers of free-flying insects. *Journal of Experimental Biology*, 212(9):1324–1335, 2009.

[60] Wayne A. Rowley and Charles L. Graham. The effect of age on the flight performance of female *Aedes aegypti* mosquitoes. *Journal of Insect Physiology*, 14(5):719 – 728, 1968.

[61] Wayne A. Rowley and Charles L. Graham. The effect of temperature and relative humidity on the flight performance of female *Aedes aegypti*. *Journal of Insect Physiology*, 14(9):1251 – 1257, 1968.

[62] DAVID C. SANDEMAN and H. MARKL. Head movements in flies (calliphora) produced by deflexion of the halteres. *The Journal of Experimental Biology*, 85(1):43–60, 1980.

[63] Sanjay P. Sane and Michael H. Dickinson. The aerodynamic effects of wing rotation and a revised quasi-steady model of flapping flight. *Journal of Experimental Biology*, 205(8):1087–1096, 2002.

[64] C. Schilstra and J.H. Hateren. Blowfly flight and optic flow. i. thorax kinematics and flight dynamics. *Journal of Experimental Biology*, 202(11):1481–1490, 1999.

[65] C Schilstra and JH Van Hateren. Stabilizing gaze in flying blowflies. *Nature*, 395(6703):654–654, 1998.

[66] David J Sheskin. *Handbook of parametric and nonparametric statistical procedures*. Chapman and Hall/CRC, 2003.

[67] Mandyam V Srinivasan. A visually-evoked roll response in the housefly. *Journal of comparative physiology*, 119(1):1–14, 1977.

[68] Hiroki Sugiura and Michael H Dickinson. The generation of forces and moments during visual-evoked steering maneuvers in flying drosophila. *PloS one*, 4(3):e4883, 2009.

[69] Willem Takken and Bart GJ Knols. Odor-mediated behavior of afrotropical malaria mosquitoes. *Annual review of entomology*, 44(1):131–157, 1999.

[70] Lance F. Tammero and Michael H. Dickinson. The influence of visual landscape on the free flight behavior of the fruit fly drosophila melanogaster. *Journal of Experimental Biology*, 205(3):327–343, 2002.

[71] Lance F Tammero and Michael H Dickinson. The influence of visual landscape on the free flight behavior of the fruit fly drosophila melanogaster. *Journal of Experimental Biology*, 205(3):327–343, 2002.

[72] Graham K Taylor and Adrian LR Thomas. Dynamic flight stability in the desert locust schistocerca gregaria. *Journal of Experimental Biology*, 206(16):2803–2829, 2003.

[73] Lloyd N Trefethen. Pseudospectra of linear operators. *SIAM review*, 39(3):383–406, 1997.

[74] MS Tu and MH Dickinson. The control of wing kinematics by two steering muscles of the blowfly (calliphora vicina). *Journal of Comparative Physiology A*, 178(6):813–830, 1996.

[75] Floris van Breugel and Michael H. Dickinson. The visual control of landing and obstacle avoidance in the fruit fly drosophila melanogaster. *The Journal of Experimental Biology*, 215(11):1783–1798, 2012.

[76] Steven Vogel. Flight in drosophila : I. flight performance of tethered flies. *Journal of Experimental Biology*, 44(3):567–578, 1966.

[77] H. Wagner. Flight performance and visual control of flight of the free-flying housefly (musca domestica l.) i. organization of the flight motor. *Philosophical Transactions of the Royal Society of London. B, Biological Sciences*, 312(1158):527–551, 1986.

[78] Simon M. Walker, Adrian L. R. Thomas, and Graham K. Taylor. Deformable wing kinematics in free-flying hoverflies. *Journal of The Royal Society Interface*, 7(42):131–142, 2010.

[79] Simon M Walker, Adrian L.R Thomas, and Graham K Taylor. Photogrammetric reconstruction of high-resolution surface topographies and deformable wing kinematics of tethered locusts and free-flying hoverflies. *Journal of The Royal Society Interface*, 6(33):351–366, 2009.

[80] Z. Jane Wang, James M. Birch, and Michael H. Dickinson. Unsteady forces and flows in low reynolds number hovering flight: two-dimensional computations vs robotic wing experiments. *Journal of Experimental Biology*, 207(3):449–460, 2004.

[81] Anne-Kathrin Warzecha and Martin Egelhaaf. Response latency of a motion-sensitive neuron in the fly visual system: dependence on stimulus parameters and physiological conditions. *Vision Research*, 40(21):2973 – 2983, 2000.

[82] JP Whitney and RJ Wood. Aeromechanics of passive rotation in flapping flight. *Journal of Fluid Mechanics*, 660(1):197–220, 2010.

[83] Thomas G Wright and Lloyd N Trefethen. Large-scale computation of pseudospectra using arpack and eigs. *SIAM Journal on Scientific Computing*, 23(2):591–605, 2001.

[84] Jiang Hao Wu and Mao Sun. Floquet stability analysis of the longitudinal dynamics of

two hovering model insects. *Journal of The Royal Society Interface*, 9(74):2033–2046, 2012.

[85] Na Xu and Mao Sun. Lateral dynamic flight stability of a model bumblebee in hovering and forward flight. *Journal of theoretical biology*, 319:102–115, 2013.

[86] William J. Yurkiewicz and T. Smyth Jr. Effect of temperature on flight speed of the sheep blowfly. *Journal of Insect Physiology*, 12(2):189 – 194, 1966.

[87] P. O. Zanen and R. T. Card. Directional control by male gypsy moths of upwind flight along a pheromone plume in three wind speeds. *Journal of Comparative Physiology A*, 184(1):21–35, 1999.

[88] J. M. Zanker. The wing beat of *Drosophila Melanogaster*. i. kinematics. *Philosophical Transactions of the Royal Society of London. B, Biological Sciences*, 327(1238):1–18, 1990.

[89] Wolfram Zarnack and Michael Wortmann. On the so-called constant-lift reaction of migratory locusts. *Journal of experimental biology*, 147(1):111–124, 1989.

[90] Yanlai Zhang and Mao Sun. Dynamic flight stability of a hovering model insect: lateral motion. *Acta Mechanica Sinica*, 26(2):175–190, 2010.